Summer 2008

Experimental validation of an integrated FRP and visco-elastic hardening, damping, and wave-modulating system for blast resistance enhancement of RC columns

Brian Henry Wood

Department:

EXPERIMENTAL VALIDATION OF AN INTEGRATED FRP AND VISCO-ELASTIC HARDENING, DAMPING, AND WAVE-MODULATING SYSTEM FOR BLAST RESISTANCE ENHANCEMENT OF RC COLUMNS

by

BRIAN HENRY WOOD

A THESIS

Presented to the Faculty of the Graduate School of the

MISSOURI UNIVERSITY OF SCIENCE AND TECHNOLOGY

In Partial Fulfillment of the Requirements for the Degree

MASTER OF SCIENCE IN CIVIL ENGINEERING

2008

Approved by

Genda Chen, Advisor
John J. Myers
Jason Baird

ABSTRACT

In today's society, terrorist attacks and accidental explosions pose a major threat to critical infrastructure. Vulnerable to blast loading, structures must be rehabilitated to ensure structural stability and protect human life. The goal of this study is to develop and validate a sandwich composite technology for column retrofitting. The new technology consists of an inner fiber reinforced polymer (FRP) sheet, an outer FRP sheet, and a visco-elastic (VE) layer sandwiched between the two FRP sheets. The inner FRP sheet is wrapped around an existing column for confinement, while the outer FRP sheet is for anchoring of the VE layer into the column supports. The compact, inexpensive, and easy to construct system has been shown effective under seismic loads. In this study, the blast performance of the engineering system is investigated with two main objectives: to field validate the effectiveness of the system for hardening, damping, and wave-modulating (HDM) of a reinforced concrete (RC) column under blast loads, and to validate the performance of coaxial cable crack sensors for dynamic measurements under blast loads. The sensors have undergone extensive testing under static and cyclic loadings, but their performance under high strain-rate loading is still unknown. Dynamic measurements with coaxial cable sensors were recently made possible due to the introduction of a high-speed oscilloscope. To accomplish the objectives, a ¼-scale, three-column specimen was designed, cast, and tested under blast loads. One column was considered as a benchmark without any retrofitting, the second column was wrapped with one FRP sheet for confinement, and the third column was retrofitted with the new composite technology. Test results indicated that the third column experienced the smallest permanent deflection. The cable sensors can effectively measure the dynamic responses of columns.

ACKNOWLEDGEMENTS

Many people at the Missouri University of Science and Tech. deserve a great deal of gratitude for their guidance and assistance throughout my research. First, I would like to thank Dr. Genda Chen, my advisor, for his guidance throughout my graduate studies. Dr. Chen gave me the opportunity to work on cutting edge research, and I learned a great deal of knowledge from him. I would like to thank Dr. Jason Baird for all of his guidance and explosives expertise and for keeping all of us safe during the blast testing. I would also like to thank Dr. John Myers for serving on my committee as well as Caltrans and the MS&T Center for Transportation Infrastructure and Safety for funding my research.

The experimental phase of my research would not have been possible without the help of several students and University staff members. I want to thank Mei Wang for developing the FE model, Igor Izyumin and Hongxia Ning in Electrical Engineering for their assistance during the testing and data processing, Jason Cox and Travis Hernandez for their assistance with the specimen construction and for their concrete and composites expertise, and Jeff Bradshaw for overseeing all of the instrumentation during my testing.

I would like to extend my thanks to Dr. Richard Helgeson at the University of Tennessee at Martin who initiated my interest in structural dynamics and guided me through my undergraduate research. I owe a special thanks to my parents and the rest of my family who have always encouraged and supported me with the utmost enthusiasm in everything that I have ever done. Last but certainly not least, I would like to thank my wonderful wife, Jennifer, who has always supported me and endured this time away from our family and friends while we pursue our graduate degrees.

TABLE OF CONTENTS

LIST OF ILLUSTRATIONS

LIST OF TABLES

1. INTRODUCTION

1.1. GENERAL

Columns in buildings and bridges serve a critically important role in the overall load path of a structural system. They allow the loads from the girders and floor or deck system to be transferred to the foundation and ultimately to the ground. In structures with little or no redundancy, damage or removal of columns could result in immediate collapse of the entire structure. In the event of an earthquake or explosion, damage to girders or floor systems will not necessarily cause collapse, but damage or failure of columns will cause either collapse or redistribution of loads which could ultimately lead to collapse.

When considering building retrofit for blast loading, there are three primary areas that should be addressed. These include glazing protection (windows), strengthening of walls to prevent debris from being ejected into the building, and strengthening of columns to prevent progressive collapse. Much research has been conducted and is still being carried out in these first two areas, but little research has been conducted regarding strengthening of columns for blast loads. One of the main reasons for this lack of research is the fact that experimental blast testing on column specimens is very expensive, and as with all blast testing, you only have one shot at collecting good data from the test.

The Alfred P. Murrah Building in Oklahoma City was severely damaged by a truck bomb in 1995, and the collapse of the building caused extensive loss of life. It has been shown by analyses that the actual blast only damaged a small portion of the building, and the majority of the collapse was caused by progressive collapse (Kiger and

Woodson, 2008). This means that the structure was unable to properly redistribute gravity loads following the removal of some of its supporting members. It has also been shown that a similar amount of damage would have been caused by merely removing a single column from the first floor (Kiger and Woodson, 2008). Had the structure been designed to be able to redistribute loads or had first floor columns been capable of resisting the blast load, only a small portion of the building would have been damaged, but more importantly, very few people would have lost their lives. This example effectively illustrates the importance of columns in preventing progressive collapse.

In the LRFD (Load and Resistance Factor Design) method of design, columns and other compression members have higher factors of safety because of their importance in the overall performance of a structural system. The factors in the current design specifications, however, do not account for blast loads, as this would be uneconomical in most situations. Blast loads are taken into account for structural hardening of critical constructed facilities. The structural reliability of critical infrastructure such as hospitals, government agencies (fire stations, police stations, etc.), and central transportation structures should most certainly be considered when examining terrorist attack and accidental explosion scenarios. Large-scale attacks such as those that occurred on September 11, 2001, however, cannot economically be planned for, and we hope that nothing of this magnitude will ever transpire again.

In reinforced concrete structures, it can be difficult to detect cracks after a dynamic loading event such as an earthquake or explosion has occurred. After the event is over, gravity loads can often close the cracks, rendering them undetectable. A coaxial cable crack sensor developed at Missouri S&T under the direction of Dr. Genda Chen

(Chen et al., 2004; 2005) can detect cracks during static and cyclic loading. Liang Xue (2006) then developed a high-speed time-domain reflectometer (TDR) system that could be used with the crack sensors to detect cracks dynamically, or while a loading event is taking place. This allows the observation of cracks as they open and close. The system has been tested previously under moderately high strain-rate loading (earthquake loading), but had not been tested under extremely high strain-rate loading such as blast loading. If implemented, this system could prove to be a valuable tool for structural health monitoring of RC structures and for the assessment of post-disaster damage.

1.2. RESEARCH OBJECTIVES

The research presented in this thesis had two primary objectives.

- The first objective was to investigate the performance of the FRP-VE hardening, damping, and wave-modulating system under real blast loads and to compare the experimental results with simulation results.
- The second objective was to validate the performance of the coaxial cable crack sensors when measured dynamically during a blast.

2. LITERATURE REVIEW

2.1. GENERAL

There have been many efforts to study different methods of retrofitting structures to resist blast loads. As mentioned previously, there are three areas of concern in strengthening for blast – glazing, masonry walls, and columns. Since this research focuses on the latter, this review places emphasis on strengthening of columns for blast loads. Malvar et al. (2004) noted that FRP wrapping, as well as steel jacketing of RC columns is now a proven method of retrofitting structures to resist both earthquakes and blast loads from close-in explosions. A brief overview of the materials that are used in the proposed strengthening system is also given, as well as a review of the literature relating to the coaxial cable crack sensor studied in this research. For more information on the strengthening of masonry walls, slabs, and beams for blast resistance, readers are referred to Buchan and Chen (2007).

2.2. SEISMIC VERSUS BLAST RETROFIT

Over the past two or three decades, several methods have been developed for strengthening of RC structures to resist seismic loads by either upgrading structural members or using fiber reinforced polymers or steel sheets. Many types of dampers and base isolation systems have also been developed. Most of these methods have been shown to be very effective in mitigating earthquake loads and have therefore been implemented in retrofitting buildings in regions of high seismicity.

Although both blast and seismic loads are dynamic, they are very different in nature and should be treated separately. The primary distinction between the two lies in

the fact that blast loads are short duration and impulsive in nature, while earthquake loads are longer duration and cyclic in nature. The natural period and corresponding natural frequency are important parameters in both cases, but for different reasons. During an earthquake, structures are most sensitive to input frequencies close to their own natural frequencies. In simple terms, this means that if the earthquake is shaking the ground at the same frequency (or close to the same frequency) as one of the building's natural frequencies, then the building's response will be maximized. In contrast, blast loads have a very short duration, usually on the order of a few milliseconds if considering conventional explosions and up to a few hundred milliseconds if considering nuclear explosions. If the duration of the blast is very short relative to the natural period of the structure, the load has finished acting before the structure has had time to respond (Mays and Smith, 1995). This type of loading is impulsive, and the displacement is a function of impulse (momentum), stiffness, and mass. However, if the duration of the blast is long relative to the natural period of the structure, the structure has attained its maximum deflection before the load has finished acting. This type of load is called quasi-static loading, and the displacement is a function of the peak blast load and the stiffness (Mays and Smith, 1995). It is also important to note that with earthquake loads several modes may contribute to the response, while under blast loads one mode dominates (Kiger and Woodson, 2008). This means that if the structure is a multi-degree-of-freedom structure, only the first mode will contribute to the response under blast loads but several modes may contribute under earthquake loads.

Some researchers have suggested that strengthening for earthquake loads will subsequently increase blast and progressive collapse resistance. In some cases, this claim

may hold true but should be investigated on an individual basis. Hayes et al. (2005) investigated the impact that strengthening the Murrah Building in Oklahoma City for seismic loads would have on enhancing blast and progressive collapse resistance. They assumed that the building was located in a region of very high seismicity, and designed three different strengthening systems to upgrade the building to meet the current design standards set forth in FEMA 310 (1998) and ACI 318 (2002). Two of the systems focused on strengthening the ordinary moment frame system by adding new structural systems to the street face of the building (a large-pier spandrel system; new ductile special moment frame system), while the third utilized internal shear walls. They also re-detailed the original design to account for seismic loads as a fourth alternative. All four systems were equally effective in strengthening the building for seismic loading. However, only the first two strengthening systems and the re-detailed original design were effective in reducing blast and progressive collapse damage. The internal shear wall system was not as effective in reducing damage. Their analysis demonstrates that external strengthening systems can be effective in reducing blast and progressive collapse damage, while strengthening elements internal to the building envelope may not have as much impact. When strengthening for both seismic and blast loads, the engineer should investigate each load case separately instead of designing a seismic strengthening system and assuming that it is sufficient for blast loads.

2.3. BEHAVIOR AND RETROFIT OF RC COLUMNS FOR BLAST

The method commonly used in the design of structural elements to resist blast loads is the Equivalent Single-Degree-of-Freedom (SDOF) method. Malhotra, Carson,

and Stevens (2007) give a very good overview of this method. In this method, individual structural elements are reduced to an equivalent SDOF system by separating them from the complete structure and applying the proper boundary conditions. Damping is typically ignored, as it has a negligible effect for short duration, impulsive loads. The design loads are based on how much ductility (inelastic deformation) the designer allows. This inelastic deformation is 'how' the structure absorbs the kinetic energy delivered by the blast impulse. Consequently, larger ductility factors result in lower design blast loads but a higher degree of permanent deformation, while smaller ductility factors result in higher design blast loads but a lower degree of permanent deformation. A ductility factor of one denotes the start of yielding, or no permanent deformation.

There has been little research conducted in blast retrofit and behavior of RC columns. Ngo et al. studied the behavior of high-strength concrete columns subjected to blast loading, and found that high-strength concrete columns perform better than normal-strength concrete columns (with the same axial load capacity) when subjected to extreme impulsive loading. Muszynski et al. (1995 & 2003) conducted explosive tests on RC columns strengthened with Glass FRP (GFRP) and Carbon FRP (CFRP). The tests were conducted with the columns being part of a concrete cubicle. The unretrofitted columns failed in tension and spalling was evident, but the test on the retrofitted columns was inconclusive due to some problems with the test setup.

Crawford et al. (2001a) conducted an explosive trial on a four-story office building with 350 mm [13.78 in] square columns. The building was typical of an East Coast RC four-story office building located in Seismic Zone 1. This type of building – inherently weak in lateral capacity – is supported by columns having minimal ductility as

compared to a typical West Coast RC building. Because of their insufficient hoop reinforcement, the columns were expected to fail catastrophically in shear. One of the columns was a control column and the other was wrapped with six horizontal wraps and three vertical strips of CFRP. The control column failed in shear at the top and bottom, while the central section remained relatively intact and vertical. The residual deflection at the mid-height of the control column was 250 mm [9.84 in]. The retrofitted column remained elastic under the same load, and there was no apparent permanent deformation. Following these field tests, full-scale static and further explosive tests were conducted on identical columns. Three columns were tested in the laboratory – one unretrofitted, one with two layers of CFRP, and one with six layers of CFRP. The two layers of CFRP were implemented to provide just enough shear resistance to allow the column to develop its full flexural capacity. The peak resistance of the two-layer CFRP column was about twice that of the unretrofitted column, and failure was due to insufficient strength of the wrap to resist the hoop forces generated by the expansion of the concrete at a mid-height deflection of 114 mm [4.49 in]. The six-layer column design provided an excess of shear capacity, but also provided additional confinement which allowed an increase in ductility. This column was driven to 150 mm [5.91 in] of lateral deflection with no visible signs of damage. Upon unloading, the column had a residual deflection of 95 mm [3.74 in], and its residual capacity was verified by applying a 1779 kN [400 kip] axial load. Further field tests concluded that the laboratory setup was capable of producing similar results, and that the retrofit system was successful in mitigating damage caused by blast loads.

Crawford et al. (1997) conducted numerical analyses of 1.1 m [43.3 in] circular RC columns from a multi-story building retrofitted with CFRP. The Lagrangian Finite

Element code DYNA3D was used in the analyses. The concrete was modeled using eight-node brick elements, reinforcement was modeled with truss elements, and shell elements were used for the floors and joists. All results showed that the composite retrofit could have a beneficial effect on the performance of the columns, thereby preventing progressive collapse.

A single-degree-of-freedom (SDOF) method was also used by Crawford et al. (2001a and 2001b) and Morrill et al. (2004) to predict the response of FRP retrofitted columns against blast loads. They found that the predictions using this simple method were close to the observed displacements from explosive tests. Buchan and Chen (2007) noted that the method involves many simplifications to obtain a SDOF system for a structure with many degrees of freedom, and care must be taken in making these simplifications.

Woodson and Baylot (2000) conducted experiments on four quarter-scale buildings designed as typical RC structures in regions of low seismic risk, such as the northeastern United States. The first experiment was an open-frame structure and served as the baseline. The second experiment was designed to represent an RC structure with in-fill masonry walls, and the third structure was the same as the second structure but with window openings in the in-fill walls (33% of surface area). The fourth experiment was similar to a parking garage configuration. All test structures were designed as flat-plate floor systems on square columns with edge beams and with drop panels at the interior columns. Among other significant findings, it was demonstrated that the presence of in-fill walls has a significant effect on the impulse of the load applied to a column because of clearing effects. Additionally, the edge beams carried the dead

weight, particularly the added weight at the top of the column when the columns incurred severe damage.

Al-Salloum (2007) conducted tests on 42 small scale concrete cylinders confined with GFRP or CFRP. The purpose was to test the effect of high temperatures on FRP-confined concrete. The specimens were exposed to room temperature and heating regimes of 100°C [212°F] and 200°C [392°F] for a period of one, two, or three hours. The test results demonstrated that at a temperature of around the glass transition temperature of the resin, CFRP and GFRP wrapped specimens experienced a small loss in strength resulting from melting of epoxy. The damage was more pronounced when the temperature reached 200°C [392°F]. These tests exposed the specimens to high temperature for extended periods of time. No literature exists that investigates the behavior of FRP when subjected to short durations of extremely high temperatures, such as that seen in a blast. The glass transition temperature of MBrace Saturant is 71°C [163°F] (WBA Corp., 2002).

At the University of California, San Diego, a system was designed and built to perform laboratory blast simulations (Gram et al., 2006). The system uses impact loading to produce a 2 ms pulse with a typical peak pressure loading of 35 MPa [5076 psi] and an impulse of 14 kPa-s [2030 psi-ms] over the surface of the column. Recording the specimen failure with high-speed video is made possible by the absence of the fireball that would usually be present in an actual explosion. The paper notes that comparison of post-test laboratory and field data from similar tests conducted on similar test specimens have revealed excellent correlation of impulse, deformation, and failure mode. However, many experts in the field of blast research assert that the system does not truly simulate

blast loading conditions. The system is also limited to a minimum loading duration of a few milliseconds, making it incapable of simulating close-in blasts, which can have positive durations of less than one millisecond.

2.4. FRP AND VE MATERIALS

2.4.1. FRP Composite Materials. FRP materials have come to the forefront of structural engineering in recent years. They have become popular materials for strengthening applications because of their high strength, ease of installation, and excellent corrosion resistance. FRP fabrics consist of parallel strands of continuous fibers that are woven together to form a long roll of a specific width. Fabrics can either be of the unidirectional form, as described above, or bidirectional in which fibers are oriented perpendicular to each other (Bank, 2006). Bidirectional fabrics can be used in cases in which bidirectional strengthening is desired, such as walls or two-way slabs. In order to allow load transfer from the base material (substrate) to the FRP and to distribute the load throughout the fibers evenly, the FRP sheets are encased in a polymer matrix. The polymer matrix, usually low in strength, also serves to protect the fibers from damage and keep the fibers aligned. In strengthening situations that are bond-critical, an adhesive primer is first applied directly to the substrate before applying the FRP and polymer material.

FRP fabrics are made of three types of materials – carbon, glass, and aramid (Kevlar). Table 2.1 gives a comparison of the primary material properties. All three types have been used in blast resistant retrofits, but carbon and glass were used the most extensively. Crawford et al. (1997) stated that although carbon and glass are typically

used for column retrofits, aramid would be more appropriate due to its impact resistance. However, in a later paper, Crawford et al. (2001b) stated that carbon is preferred to glass and aramid for wrapping because of its high stiffness, which allows for higher lateral confining forces and better ductility enhancement. Buchan and Chen (2007) noted that greater confinement can also be achieved by using a larger amount of a less stiff material. Aramid would perhaps be better suited for wall and slab retrofits because of its impact resistance.

Table 2.1. Comparison of FRP Materials (Bank, 2006)

	Density (kg/m^3) [lb/in^3]	**Tensile Modulus (GPa) [ksi]**	**Tensile Strength (MPa) [ksi]**
Carbon	1688 – 2104 [0.061 – 0.076]	250.3 – 799.8 [36,300 – 116,000]	2400 – 4800 [348 – 696]
Glass	2464 – 2574 [0.089 – 0.093]	72.39 – 88.25 [10,500 – 12,800]	2344 – 4600 [340 – 667]
Aramid	~1412 [~ 0.051]	68.95 – 124.1 [10,000 – 18,000]	3447 – 4137 [500 – 600]

2.4.2. Visco-Elastic (VE) Material Properties. VE materials have been used for vibration control since the mid-1950's, and the application of VE dampers to civil engineering structures began about 20 years later when 10,000 VE dampers were installed in each of the twin towers of the former World Trade Center to help resist wind loads (Huang, 2005). A more thorough review of the behavior and use of VE materials in civil engineering structures can be found in the dissertation by Huang (2005).

Sorbothane, the visco-elastic material that was used in this research, is a thermoset, polyether-based, polyurethane material (Sorbothane, 2001). VE materials

exhibit properties of both viscous materials, which dissipate energy, and elastic materials, which store energy. One of the advantages of VE materials is that they are effective in applications of vibration damping as well as shock absorption. Figure 2.1 shows the hysteretic response of Sorbothane and natural rubber. The area under the curve represents the energy that is dissipated. Figure 2.2 shows the response of Sorbothane and other materials to an impulse. The impulse shown on the graph looks much like a blast load, and the Sorbothane results in approximately an 82 % reduction in the G-force.

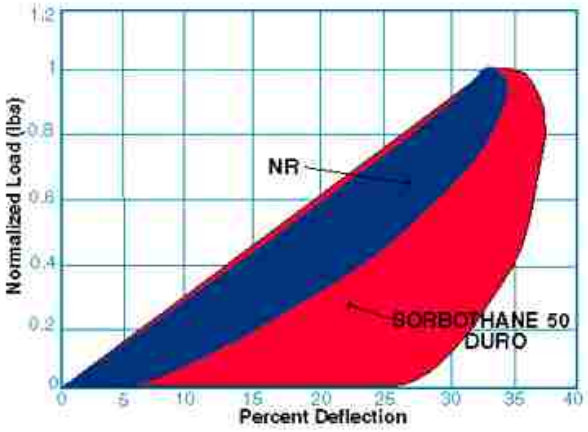

Figure 2.1. Hysteretic Response of Sorbothane and Natural Rubber (Sorbothane, 2001)

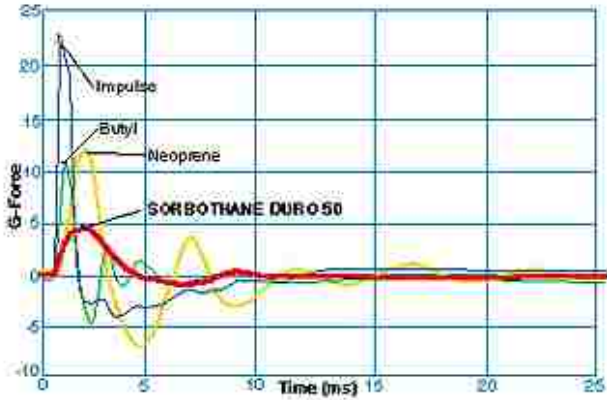

Figure 2.2. Response of Sorbothane and Other Materials to an Impulse (Sorbothane, 2001)

Luo et.al (2007) developed an analytical solution for a layered elastic stress wave attenuator system to mitigate impulsive loads. They showed that when an incident stress pulse passes through a two-layer structure, a reduced stress amplitude and elongated pulse duration could be obtained with proper selection of materials and layer dimensions. Visco-elastic material properties were used in the analysis, but no experimental results were presented.

2.5. EMBEDDED COAXIAL CABLE CRACK SENSORS

2.5.1. Background and Design. The crack sensors that were developed at Missouri S&T have undergone extensive testing to understand their behavior under static loading as well as the influence of environmental factors on their performance in the field. The principle on which the sensor design is based is called electrical time-domain reflectometry (ETDR). ETDR is a remote sensing technology that implements the use of information collected from the reflected wave along the length of a signal carrier after an electrical signal in the form of fast-rising pulses has propagated through the signal carrier (McDaniel, 2004). Figure 2.3 shows a cut-away view of the crack sensors.

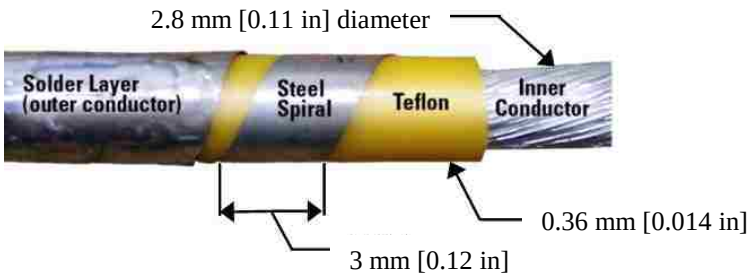

Figure 2.3. Cut-Away View of Crack Sensor (McDaniel, 2004)

To fabricate the sensors, a 10 gage wire is wrapped with a stainless steel spiral along the entire length of the cable. A very thin layer of solder is then applied on top of the spirals to create a continuous outer conductor and to prevent premature separation of the spirals. In place of hand-soldering, a thermal spray system that uses plasma gas and a very fine copper powder can be used to create the continuity in the outer conductor. The coating can either be applied using a hand-operated spray gun or by using robotic equipment. Although the robotic equipment creates the most uniform coating, either method (hand or robotic) has been proven to create a more consistent coating than the hand-soldering method in addition to being less time-consuming.

The sensor is then embedded in concrete either by pre-forming or cutting a 13 mm [0.5 in] by 13 mm [0.5 in] groove along the face of the member on which you wish to detect cracks. An adhesive primer is then brushed in the groove, the sensor is placed in the groove, and the groove is filled with grout. When the concrete member is loaded and cracks begin to form, the cracks pull apart the steel spirals on the sensor. This action causes a local disruption in the flow of current which affects the characteristic impedance of the sensor at that location. Figure 2.4 illustrates the effect of a separation in the outer conductor on the flow of current. By measuring the signal voltage using a digital oscilloscope, one can obtain the reflected voltage as a function of time along the length of the cable.

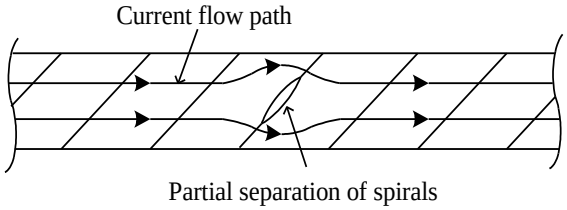

Figure 2.4. Path of Current along Disturbed Outer Conductor (McDaniel, 2004)

The propagation time scale can be converted to distance along the cable by dividing by two and multiplying by the signal propagation velocity, which is based on the electrical properties of the cable. The reflected voltage can be converted to a dimensionless measure called reflection coefficient (Γ) by dividing it by the voltage of the original pulse signal. Once these conversions are made, the signal is then in the form of reflection coefficient as a function of distance along the cable. From this data, the locations of various cracks along the member are easily established. Figure 2.5 demonstrates how the sensors work in an actual structure. The cracks, of course, do not have to be as large as the ones shown in the picture for the sensor to work properly, but this figure illustrates the separation of the spirals around the sensor.

Figure 2.5. Separation of Steel Spirals in Two Cracks

2.5.2. Use for Dynamic Measurement. The sensors were originally developed to detect cracks under static loads. Xue (2006) then developed a TDR system that was capable of monitoring the signal along the cable in real time under dynamic loading. The system is based on a fast-rising pulse generator and a high-speed digital oscilloscope that performs fast measurement and data storage, thereby allowing real-time measurement and analysis.

This new system allowed a much broader application of the crack sensor technology. It allows the engineer to monitor, in real-time, the opening and closing of cracks while a dynamic event is occurring. This has important implications for post-disaster assessments. Following a dynamic event, gravity loads will often close cracks that may have formed on a column during the event. During the development of this system, lab experiments were conducted to validate the performance of the sensors under earthquake loading, but no extremely high strain-rate loading, such as blast loading, was conducted.

3. BACKGROUND OF THE HDM SYSTEM AND SPECIMEN DESIGN

3.1. CONCEPT

The concept of the hardening, damping, and wave-modulating (HDM) system is fairly simple, and is very similar to the concept of VE dampers. The system consists of one or more sheets of FRP wrapped around the column, a VE layer wrapped around the FRP sheets, and one FRP sheet on the outside of the VE layer that is anchored into the footing of the column, as shown in Figure 3.1. The FRP rod and epoxy anchorage system was not used in this study since the columns were fixed at both ends making the anchorage not necessary for the system to be effective. In cantilevered columns, however, the anchorage must be present in order for the system to reach its full capability.

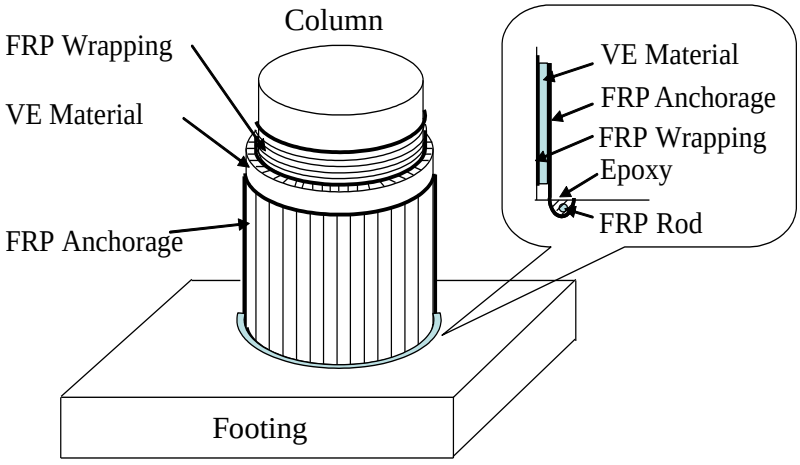

Figure 3.1. Composition of the HDM System (Huang, 2005)

As shown in the figure, the first layer of FRP is oriented with its fibers going around the column, and the outer layer is oriented with its fibers parallel to the length of

the column. The first layer(s) of FRP provides confinement to the column, significantly increasing its ductility under large deformations. Since the outer layer of FRP is anchored into the footing, when the column is bent to the right, the VE layer on the left side undergoes shear deformation between the inner and outer FRP sheets and dissipates energy. This action is reversed when the column bends in the other direction, making the system very effective at dissipating energy for cyclic loading. Huang (2005) stated that the main design parameters of the system include the number and height of the inner FRP sheets, thickness and height of the VE layers, the ratio of Young's moduli between the VE material and concrete, bond strength, and embedment length of the outer FRP sheet for anchorage. He conducted a parametric study to find the parameters that would result in the best performance. He found that for seismic loading, thinner VE and higher VE hardness (Durometer) result in greater energy dissipation. He also noted that FRP materials with higher stiffness values result in greater shear stresses in the VE materials (greater energy dissipation). It is expected that the optimal parameters for blast loading will be different than those for seismic loading. For example, it is likely that thicker and softer VE material will result in more energy dissipation under blast loads.

3.2. APPLICATION TO BLAST LOADS

The HDM system was originally developed for cyclic loading, such as earthquake loads, but it can also be effectively applied to mitigate blast loads, which are impulsive and very short in duration. It is understood that damping, unless a very large percentage of critical damping (the damping coefficient that inhibits oscillation completely; corresponds to a damping ratio equal to one) is provided, does not have a

significant effect on the peak response of a structure that is subjected to an impulsive load. However, damping is extremely important for reducing the response of a structure subjected to cyclic loading.

Because of the nature of VE materials, merely applying a layer of the material on a surface that is subjected to blast loading can absorb a portion of the energy. Figure 2.2 in the previous section shows the response of Sorbothane to an impulse. It can be seen in the figure that the VE material results in a very significant reduction in the response. However, this is only true if the duration of the load is long enough for the VE material to deform. If the duration is too short, the material will behave as a rigid material and will have no energy absorption effect. A blast load subjects a structure to an instantaneous velocity, and after the blast load is over the structure is in free vibration. It is during this free vibration that the shear deformation in the VE material dissipates energy. Hence, the system is effective against both impulsive and cyclic loading.

A contact charge will generally punch a hole on an RC column (cratering) and cause spalling on the back side of the column as a result of the blast-induced tension stress wave. On the other hand, a far-field charge will mainly induce blast incident and possibly reflected pressures on the column. It will also generate dynamic pressure (dynamic wind) effects on the column. If the stand-off distance is close to the column, both punching (impulse) and blast-induced vibration effects will be important. If the angle of incidence of the blast wave on the surface of the structure is between 0° and approximately 40°, the surface will also see the reflected pressure (Mays and Smith, 1995). Reflected pressure is seen when the reflected wave travels through gas that has already been compressed by the initial passage of the blast wave (prior to reflection). To

enhance the column performance against close-in explosions, the system integrates hardening, damping, and wave modulation to mitigate the effects of the blast. The wave modulation can be explained by examining the impedance difference between the different materials used in the system (FRP, VE, and concrete). When the stress wave travels through materials of different densities, it is attenuated by the concept of impedance mismatching. This attenuation would theoretically be optimized by maximizing the acoustic impedance mismatch of the adjoining materials. This effect is similar to using two concrete panels (donor and acceptor) separated by a sand filled cavity to resist close-in blast loads. The attenuation of the blast by the sand is accomplished by (1) the increased mass it affords to the concrete portions of the wall, (2) the increased distance the blast wave must travel due to the increased wall thickness produced by the sand (dispersion of the blast wave), (3) the blast energy absorbed by the displacement and compression of the sand particles (TM 5-1300, 1990), and (4) the wave energy dissipated by the impedance mismatch between the sand particles and the air that fills the voids between the particles.

3.3. SPECIMEN DESIGN

In order to create three identical columns (before strengthening), a three-column specimen was designed, as shown in Figure 3.2. Each column was designed as a 1/4-scale specimen of a prototype bridge or exterior building column in Missouri. TM5-1300 (1990) states that exterior building columns are generally designed as beam elements, and although the axial load on these columns may be significant, usually the effect of transverse loads is greater. Also, these columns will usually be in the tension-controlled

region of the axial load–moment interaction curve where the addition of axial load increases the moment capacity of the member. For this reason, the column was designed as a flexure-controlled column. It should be noted that columns with a much larger axial load (above the balance point on the interaction diagram) will more likely fail in shear and experience a much less ductile failure than a column with a small axial load.

Figure 3.2. 3-D Rendering of Three-Column Specimen

The columns were 2.44 m [8 ft] long and 254 mm [10 in] in diameter. Each was reinforced with 6 #3 deformed bars and #3 hoops every 152 mm [6 in]. All reinforcement was Grade 60, and the reinforcement and detailing was designed based on the provisions of ACI 318-02. The 6 #3 bars were selected to provide the minimum reinforcement ratio of 0.01 specified by ACI 318-02 for compression members. The tie spacing was also selected based on the minimum tie spacing required by ACI as $16d_b$, where d_b is the diameter of the longitudinal reinforcement. The specimen had a 305 mm

[1 ft] thick footing and a 305 mm [1 ft] thick slab on top. Figure 3.3 through Figure 3.5 show the dimensions as well as the reinforcement details for both the columns and the footing and slab.

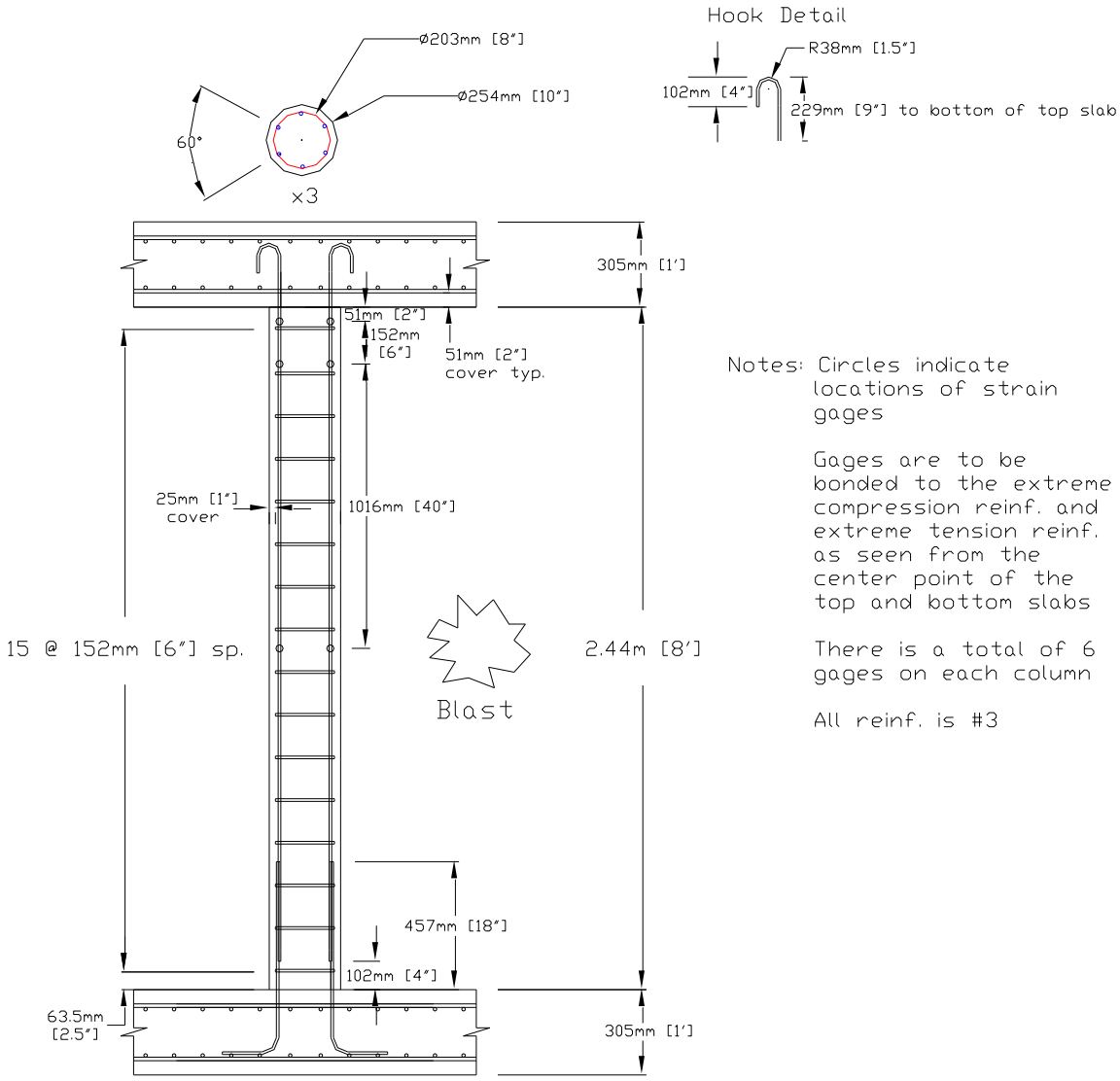

Figure 3.3. Column Reinforcement Details

The purpose of the three-column layout is such that the charge may be suspended from the top of the specimen or mounted on a pedestal so as to induce an identical blast

load on each of the three columns. The top slab was also balanced over the three columns so that very little end moment would be present on the columns before they were loaded by the blast pressure. Column 1 was the control column and had no strengthening. Column 2 was strengthened with one layer of CFRP for confinement, and Column 3 was strengthened with the HDM system.

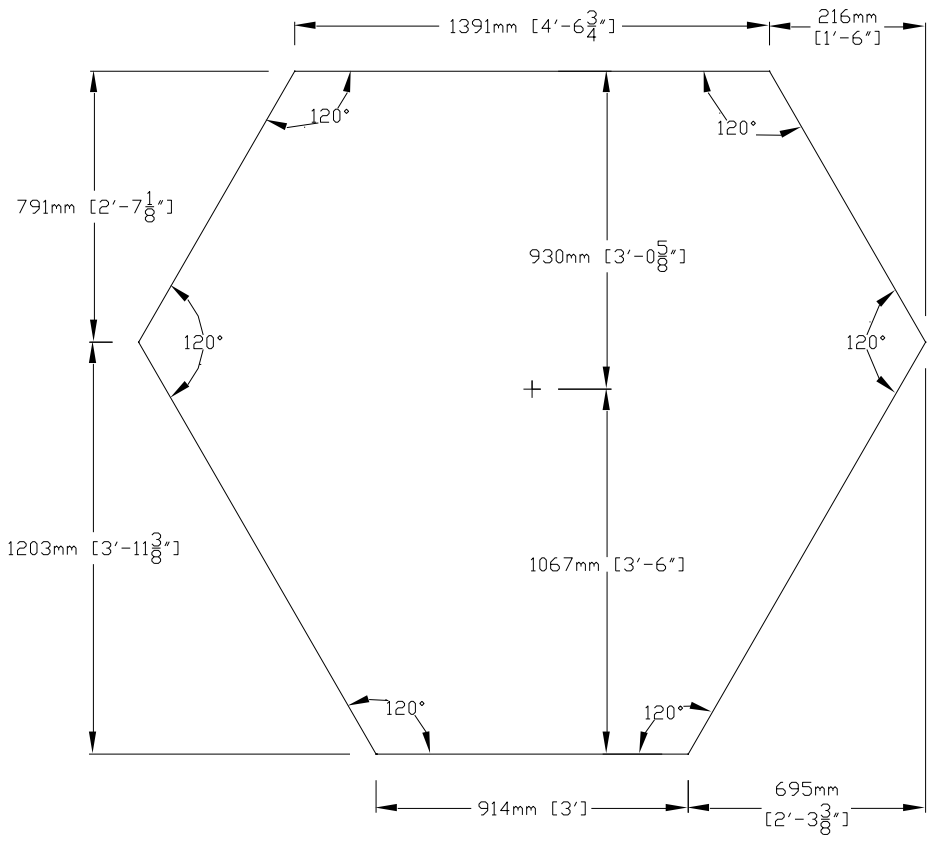

Figure 3.4. Dimensions of Footing and Slab

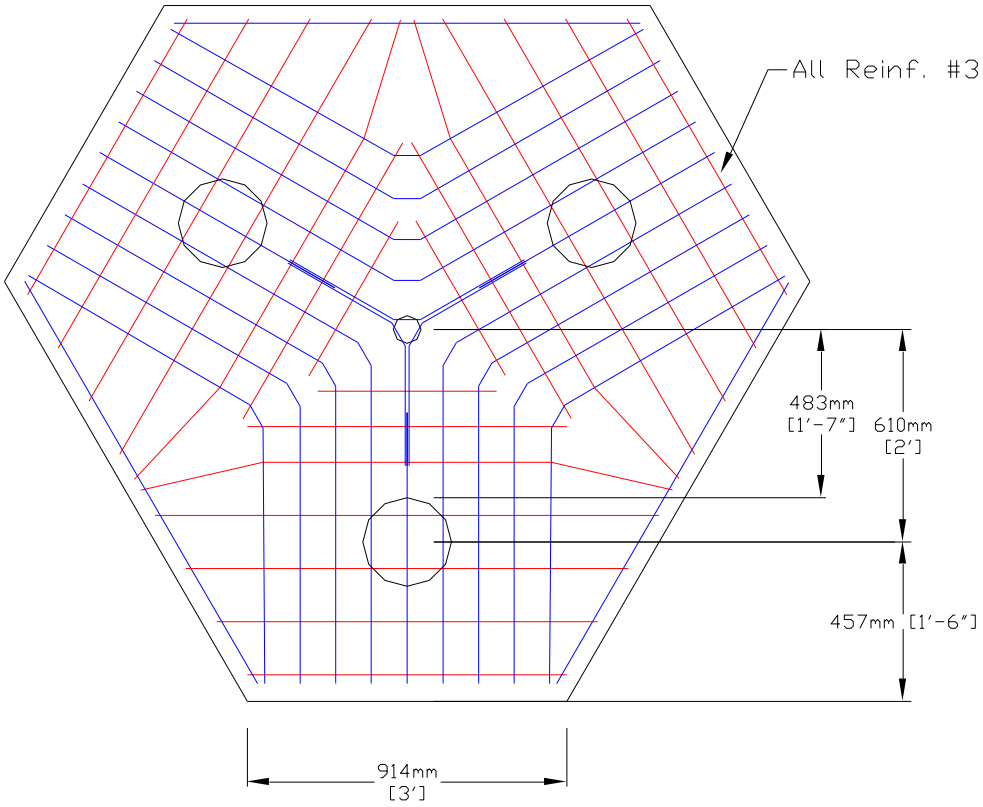

Figure 3.5. Reinforcement Details for Footing and Slab

3.4. CAPACITY ANALYSIS

The computer program USC_RC, developed by Dr. Asad Esmaeily at the University of Southern California, was used to determine the capacity of Column 1. The model takes into account the confinement provided by the ties by utilizing the Mander Confinement Model (Esmaeily, 2001). Even though the spacing of the ties is large, they still provide some ductility enhancement but not much increase in strength as shown in Figure 3.6. The model also takes into account strain-rate effects indirectly by inputting dynamic increase factors (DIF's). The DIF's used for this analysis came from the Army Technical Manual TM 5-1300 (1990), and are based on flexure for the close-in design range (no or very limited stand-off distance to the structural element). The factors used

are likely to be lower than the actual DIF's for the impulsive type loading seen in these experiments, but it is difficult to determine a definite strain rate from the experimental data that was obtained. The yield strength of the Grade 60 rebar was input as 455 MPa [66 ksi] instead of 414 MPa [60 ksi]. This is common practice in blast design, as extensive test results indicate that the average yield strength of Grade 60 steel is 455 MPa [66 ksi]. A stress-strain relationship that takes these DIF's into account was also developed for the steel rebar, as shown in Figure 3.7 The input parameters are shown in Table 3.1. USC_RC Dynamic Increase Factors (TM5-1300, 1990).

Moment-Axial Force Interaction as well as Moment-Curvature for a constant axial force of 8.18 kN [1.84 kips] (weight of slab) diagrams were developed by USC_RC for the column and are shown in Figures Figure 3.8. Column Interaction Diagram and Figure 3.9. Moment Curvature Diagram. The location of Column 1 on the interaction diagram is shown in Figure 3.8. It can be seen in the figure that the column is at the very bottom of the tension-controlled region of the interaction diagram, thus its failure should be flexural and very ductile. The analysis was set to terminate when either the confined concrete exceeded the ultimate strain or the steel strain exceeded the rupture strain. In this case, the confined concrete exceeded its ultimate strain long before the steel ruptured. The Moment-Curvature analysis yielded a maximum moment capacity of 25.4 kN [18.7 k-ft] and a ductility ratio of 29 (at a maximum curvature of 3.74×10^{-4} mm^{-1} [9.49×10^{-3} in^{-1}]). A Force-Displacement diagram for a point load at the mid-height of the column was also developed, and is shown in Figure 3.10. Force-Deflection Diagram for a Point Load at Mid-height. This yielded a lateral load capacity of 41.4 kN [9.3 kips] and a lateral displacement capacity of 61 mm [2.4 in] (at mid-height).

:

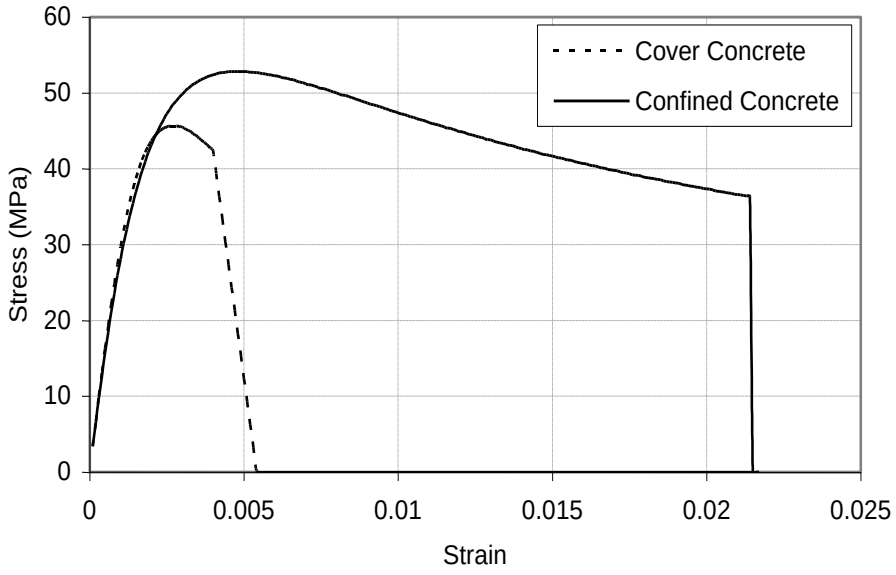

Figure 3.6. Stress-Strain Relationship for Concrete

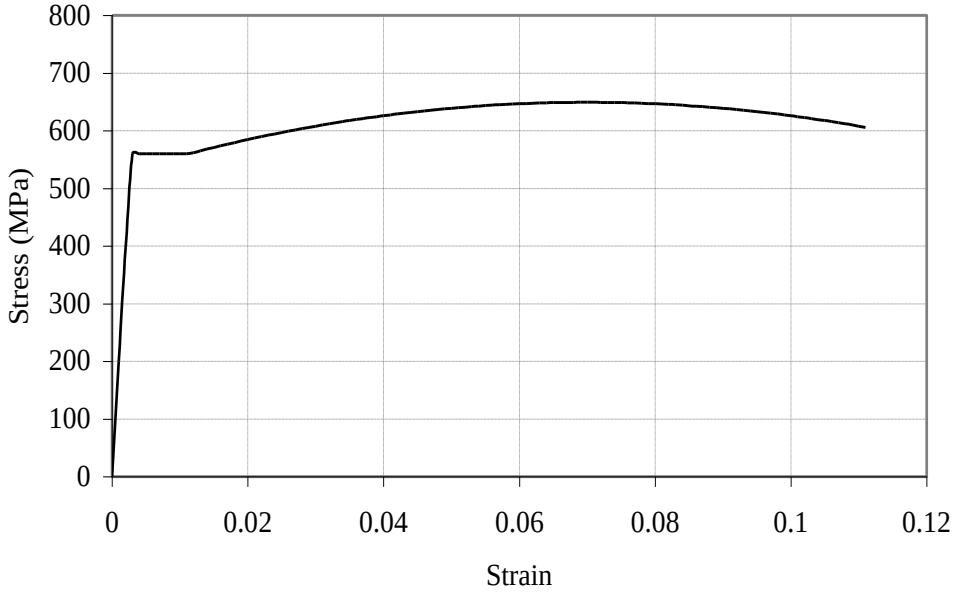

Figure 3.7. Stress-Strain Relationship of Rebar

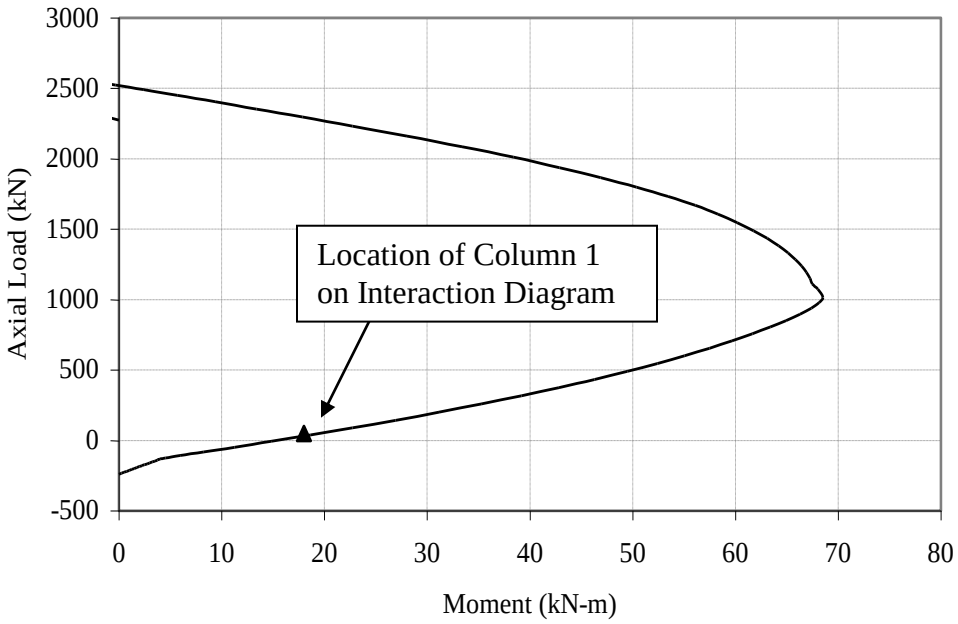

Figure 3.8. Column Interaction Diagram

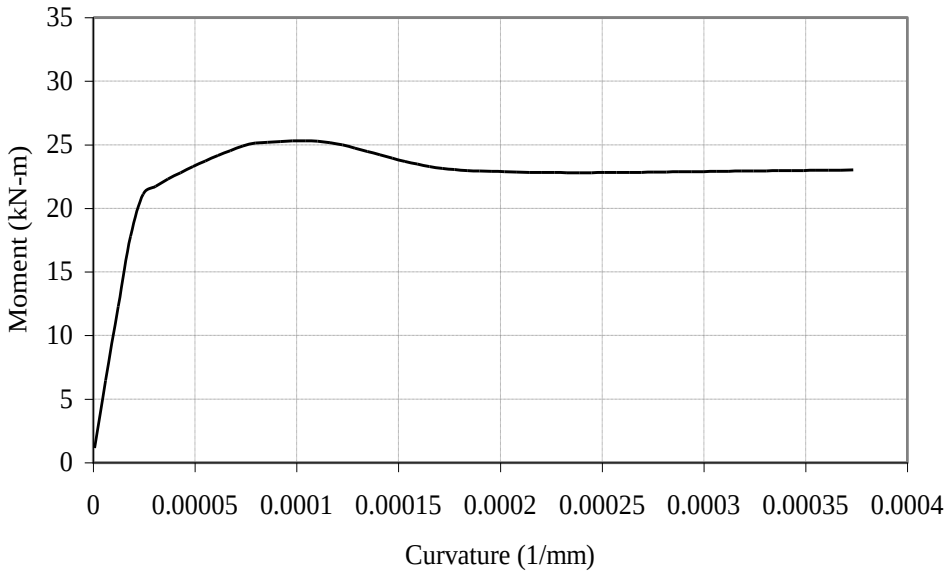

Figure 3.9. Moment Curvature Diagram

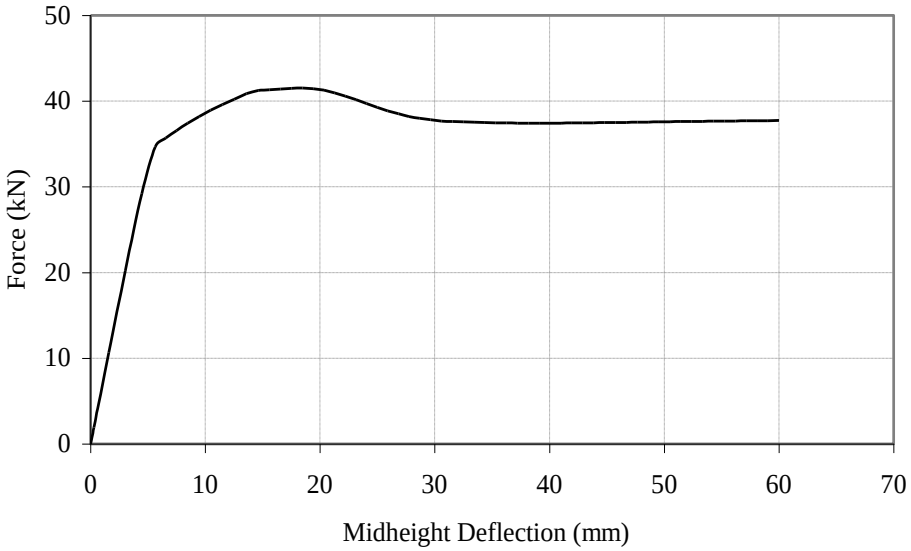

Figure 3.10. Force-Deflection Diagram for a Point Load at Mid-height

Table 3.1. USC_RC Dynamic Increase Factors (TM5-1300, 1990) and Input Parameters

Concrete Compressive Strength DIF	1.25
Steel Yield Strength DIF	1.23
Steel Ultimate Strength DIF	1.05
Unconfined Concrete Strength (Measured)	36.5 MPa [5.3 ksi]
Steel Modulus of Elasticity	200 GPa [29000 ksi]
Steel Yield Strength (from literature)	455 MPa [66 ksi]
Ultimate Strength of Steel (from literature)	621 MPa [90 ksi]

3.5. DYNAMIC ANALYSIS

In order to determine the natural frequencies and vibration modes of the RC column, the system was assumed to have its mass uniformly distributed along the length

of the column and its stiffness constant along the length. The mode shape of an Euler beam (Chopra, 2007) can be expressed as

$$\phi(x) = A_1 \cos(ax) + A_2 \sin(ax) + A_3 \cosh(ax) + A_4 \sinh(ax) \tag{3.1}$$

$$a^4 = \frac{4\pi^2 f^2 m}{EI} \tag{3.2}$$

where a is an eigenvalue parameter ($mm^{-1}[in^{-1}]$), A_1, A_2, A_3, A_4 are the integration coefficients to be determined, f is the natural frequency (Hz), m is the mass per unit length $(1.240x10^{-5}\ kg\text{-}s^2/mm^2[0.01764\ lb\text{-}s^2/in^2])$, E is the modulus of elasticity (28.61 GPa [4,150,000 psi]), and I is the moment of inertia (mm^4 [in^4]). For a column fixed at both ends, as shown in Figure 3.11, deflection and rotation are zero at the ends, or $\phi = \phi' = 0$ at $x = 0$ and at $x = L$.

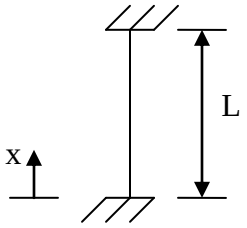

Figure 3.11. Column with Fixed-Fixed Boundary Conditions

Substituting these boundary conditions into Equation 3.1 and its first derivative, the following system of equations (matrix form) can be obtained after two simplifications

$$\begin{bmatrix} 1 & 0 & 1 & 0 \\ 0 & 1 & 0 & 1 \\ \cos(aL) & \sin(aL) & \cosh(aL) & \sinh(aL) \\ -\sin(aL) & \cos(aL) & \sinh(aL) & \cosh(aL) \end{bmatrix} \begin{Bmatrix} A_1 \\ A_2 \\ A_3 \\ A_4 \end{Bmatrix} = \begin{Bmatrix} 0 \\ 0 \\ 0 \\ 0 \end{Bmatrix} \tag{3.3}$$

Since the mass is distributed, there is an infinite set of frequencies and associated modes that satisfy Equation 3.3. For simplicity, only the first three modes will be considered, since these modes have the most effect on the dynamic behavior of the system. By solving numerically, the first three solutions become

$$aL = 4.730,\ 7.853,\ 11.00 \tag{3.4}$$

By substituting each of these values into Equation 3.2 and solving for *f*, the first three natural frequencies can be determined as functions of the moment of inertia, *I*

$$f_1 = 0.009184\sqrt{I}\ \text{Hz} \tag{3.5}$$

$$f_2 = 0.02532\sqrt{I}\ \text{Hz} \tag{3.6}$$

$$f_3 = 0.04963\sqrt{I}\ \text{Hz} \tag{3.7}$$

For an RC concrete section, the moment of inertia will have a value somewhere between that of an uncracked section and a fully cracked section. Even though the cross section is constant along the length of the column, the moment of inertia could actually vary along the length because of varying crack patterns. Methods for calculating the cracked moment of inertia can be found in MacGregor and Wight (2005). For the columns used in these experiments, the moments of inertia of the gross transformed section (uncracked) and fully cracked transformed section were calculated to be 2164 x 10^5 mm^4 [520 in^4] and 349.6 x 10^5 mm^4 [84 in^4], respectively. Figure 3.12 shows how each of the three frequencies varies as *I* changes from that of a fully cracked section to an uncracked section.

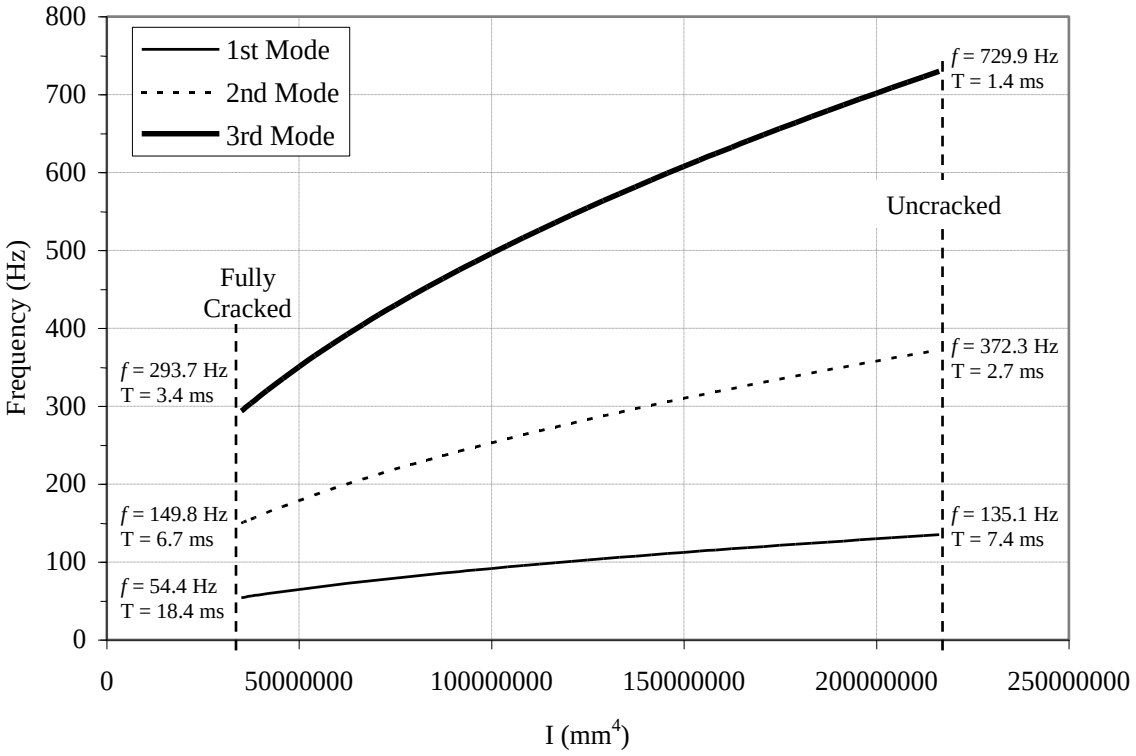

Figure 3.12. Variation of Modal Frequencies with Moment of Inertia

For the first three modes of vibration, the vibration periods range from 1.4 ms to 7.4 ms (for the uncracked section). For a very close-in blast, the duration of the blast load will most likely be a fraction of a millisecond. This means that the load will have been removed from the columns before they have time to respond, meaning that the load is mainly impulsive. In addition, the charge was installed at the mid-height of the column in this study. As such, the first mode of vibration is dominant in the column response. The dynamic analysis was used to study the effects of the two strengthening systems on the dynamic properties of the columns (natural frequency, etc.). Since the FRP and FRP-VE strengthening systems provide cracking resistance to the columns, their stiffness's are

increased, and thus their natural frequencies should see an increase as well. This analysis is discussed in Section 6.

3.6. MATERIALS

The materials used in the design consisted of Wabo MBrace CF 160 unidirectional high strength carbon fiber fabric, Sorbothane VE material, 36.54 MPa [5.3 ksi] concrete (measured strength) for the columns, and Grade 60 rebar for the reinforcement. The material properties of the CFRP (from manufacturer) that was used are shown in Table 3.2, and a close-up view of the material is shown in Figure 3.13. The unidirectional black carbon fibers can be seen in the figure along with the transversely weaved white glass fibers used to hold the carbon fibers in place.

Table 3.2. Material Properties of CFRP (WBA Corp., 2003)

Property	Value
Fabric Width	610 mm [24 in]
Nominal Thickness	0.33 mm/ply [0.013 in/ply]
Tensile Strength	3792 MPa [550 ksi]
Tensile Modulus	227.5 GPa [33,000 ksi]
Ultimate Rupture Strain	0.0167

Sorbothane is the brand name of the VE material that was used in the previous development of this system as well as in this experimental work. Table 3.3 shows the material properties from the manufacturer of the particular type of Sorbothane that was

used. The material comes in sheets that measure 610 mm [24 in] by 610 mm [24 in], and it had a Durometer (hardness) specification of 50.

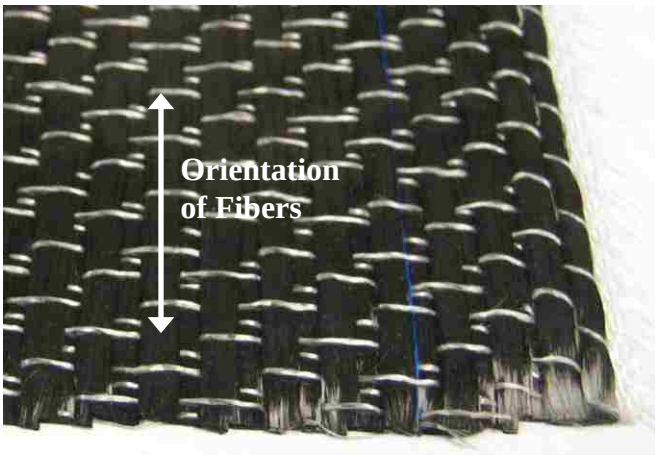

Figure 3.13. Close-up View of CFRP Fabric

Table 3.3. Material Properties of Sorbothane (Sorbothane, 2001)

Property	Value
Thickness	3.2 mm [1/8 in]
Ultimate Tensile Strength	845.3 kPa [122.6 psi]
Ultimate Elongation	568 %
Optimum Performance Temperature Range	-29° to 71° C [-20° to 160° F]
Dynamic Young's Modulus at 30 Hz	1448 kPa [210 psi]
Dynamic Young's Modulus at 50 Hz	1862 kPa [270 psi]

4. FINITE ELEMENT MODEL

4.1. FE PROGRAM UTILIZED

The finite element model (FEM) of each column was previously developed in ABAQUS Version 6.5 (as mentioned in the Acknowledgements section). As a general purpose finite element code, ABAQUS has a concrete plasticity model that allows for the damage analysis of concrete structures under cyclic and/or dynamic loading. At low confinement, concrete behaves in a brittle manner; its main damage mechanisms are associated with cracking in tension and crushing in compression. The model is capable of simulating the loss of stiffness and quantifying the level of damage by evaluating the plastic deformation that the material undergoes at ultimate strength.

Steel reinforcing bars in concrete structures are modeled as one-dimensional elements (truss elements) that can be defined individually or in a group along some surface. The truss elements are superimposed on a mesh of standard element types for concrete. The behavior of steel bars is represented by a metal plasticity model.

In ABAQUS, concrete is modeled independently of the rebar. Their interfacial behavior, such as bond slip and dowel action, can be approximately modeled by simulating the load transfer across cracks in the concrete through the rebar with a "tension stiffening" feature added to the concrete model.

ABAQUS/Explicit implements the direct time integration approach of all degrees of freedom for the evaluation of dynamic responses. It can simulate high load rate effects and the behavior of materials with degradation and failure. For blast loads, the load

condition can be specified by inputting the time-history overpressure caused by the explosion.

4.2. CONCRETE DAMAGE MODEL

The damage model that ABAQUS uses for concrete is based on plasticity and continuum mechanics. The evolution of the yield (or failure) surface is controlled by two hardening variables, $\tilde{\varepsilon}_t^{pl}$ and $\tilde{\varepsilon}_c^{pl}$, related to the damage mechanisms under tension and compression loading, respectively. The two variables are referred to as equivalent tensile and compressive plastic strains. As shown by the bold dotted lines in Figure 4.1 (a) and (b), when the concrete specimen is unloaded from any point on the strain softening branch of the stress-strain curves, the unloading response is observed to be weakened: the elastic stiffness of the material appears to be damaged (or degraded).

The degraded response of concrete is characterized by two independent uniaxial damage variables, d_t and d_c, for tension and compression, respectively. They increase with the equivalent plastic strains, ranging from zero to one, with zero for the undamaged material and one for the fully damaged material. If E_0 is the initial (undamaged) elastic stiffness of the material, the stress-strain relations under uniaxial tension and compression loading can be respectively expressed into

$$\sigma_t = (1-d_t)E_0(\varepsilon_t - \tilde{\varepsilon}_t^{pl}) \tag{4.1}$$

$$\sigma_c = (1-d_c)E_0(\varepsilon_c - \tilde{\varepsilon}_c^{pl}) \tag{4.2}$$

The effective uniaxial stresses determine the size of the yield (or failure) surface. They are defined by

$$\bar{\sigma}_t = \frac{\sigma_t}{(1-d_t)} = E_0(\varepsilon_t - \tilde{\varepsilon}_t^{pl}) \tag{4.3}$$

$$\bar{\sigma}_c = \frac{\sigma_c}{(1-d_c)} = E_0(\varepsilon_c - \tilde{\varepsilon}_c^{pl}) \tag{4.4}$$

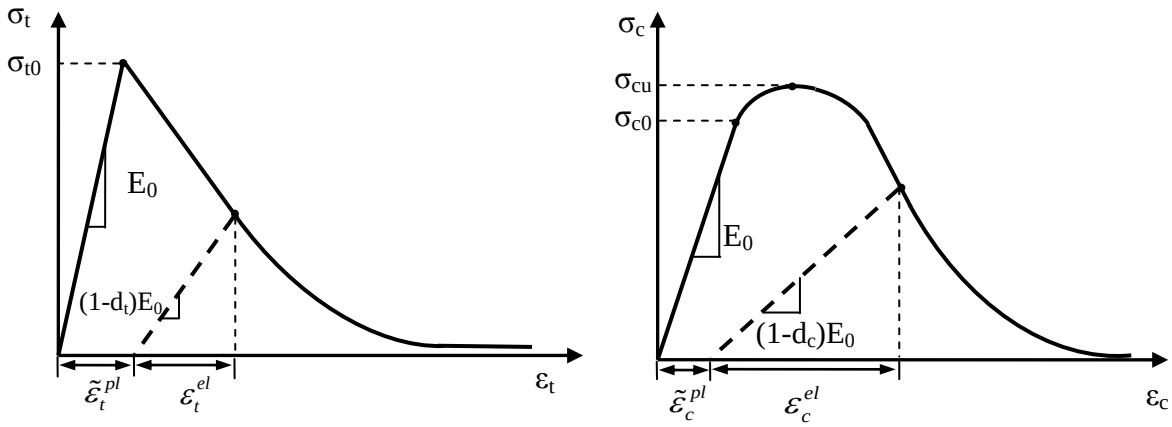

(a) Tension (b) Compression

Figure 4.1. Concrete Response to Uniaxial Loading (ABAQUS, 2005)

4.3. DYNAMIC CONSTITUTIVE DAMAGE MODEL

ABAQUS does not have damage models for impulsive-type loading, but it does have models available for general dynamic loading. However, the loads may still be applied as impulsive loads in the model. The details of the dynamic constitutive damage models for both concrete and steel rebar are described in the following sections.

4.3.1. Dynamic Compressive Strength of Concrete. For a given strain rate, the dynamic compressive strength was estimated as follows (Mendis et al., 2000):

$$K_d(\dot{\varepsilon}) = f_{cd} / f_{cm} = \begin{Bmatrix} (\dot{\varepsilon}_c / \dot{\varepsilon}_{c0})^{1.026\alpha_s} & \text{for } |\dot{\varepsilon}_c| \le 30 \quad s^{-1} \\ \gamma_s (\dot{\varepsilon}_c / \dot{\varepsilon}_{c0})^{1/3} & \text{for } |\dot{\varepsilon}_c| > 30 \quad s^{-1} \end{Bmatrix} \tag{4.5}$$

in which $\alpha_s = \left(5 + 9 f_{cm} / f_{cm0}\right)^{-1}$ and $\gamma_s = 10^{6.156\alpha_s - 2}$, f_{cd} is the dynamic compressive strength, f_{cm} is the mean value of static compressive strength, f_{cm0} = 10 MPa [1450 psi], $\dot{\varepsilon}_c$ is the strain rate (s^{-1}), and $\dot{\varepsilon}_{c0}$ = -30 x 10^{-6} s^{-1}.

4.3.2. Dynamic Concrete Stress-Strain Relation in Compression. The dynamic concrete stress-strain relationship in compression is adapted from Mendis et al. (2000) for high-strength concrete. The stress-strain curve includes a parabolic ascending portion and a straight line descending branch as shown in Figure 4.2. The ascending and descending portions can be respectively evaluated by

$$\sigma = K_d f_{cm} \left[\frac{2\varepsilon}{\varepsilon_{cd}} - \left(\frac{\varepsilon}{\varepsilon_{cd}} \right)^2 \right] \text{ for } \varepsilon \le \varepsilon_{cd} \tag{4.6}$$

$$\sigma = K_d f_{cm} \left[1 - Z_d (\varepsilon - \varepsilon_{cd}) \right] \ge f_{res} \text{ for } \varepsilon > \varepsilon_{cd} \tag{4.7}$$

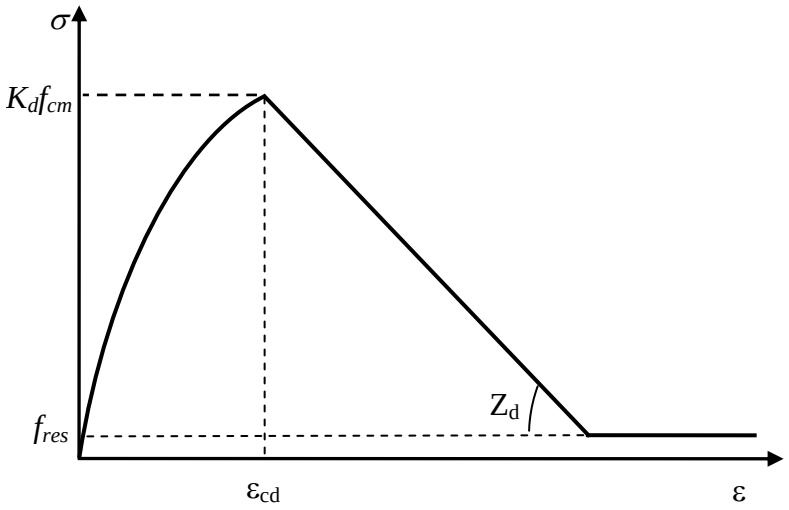

Figure 4.2. Simplified Dynamic Stress-Strain Relationship of Concrete (Mendis et al., 2000)

The residual stress, $f_{res,}$ is defined by

$$f_{res} = K_d f_{cm}(0.28 - 0.0032 f_{cm}) \geq 0 \tag{4.8}$$

where $Z_d = \dfrac{0.5K_d Z\left(\dot{\varepsilon}_c / \dot{\varepsilon}_{c0}\right)^{-\alpha}}{(3+0.29 f_{cm})/(145 f_{cm} - 1000) - \varepsilon_{cd}} \geq 0$, $\varepsilon_{cd} = (0.24K_d^3 + 0.76)\varepsilon_c$,

$Z = 0.018 f_{cm} + 0.55$, $\varepsilon_c = 4.26 f_{cm} / (\sqrt[4]{f_{cm}} E_c)$, and $E_c = 4733\sqrt{f_{cm}}$ (MPa) (ACI 318, 2002), and α will be calibrated with the dynamic test data.

4.3.3. Dynamic Tensile Strength of Concrete. For a given strain rate in the range of 10^{-6} to 160 s^{-1}, the modified Comité Euro-International du Béton (CEB) formulation of tensile strength (Malvar and Ross, 1998) was considered in this study. It can be expressed as

$$f_{td} / f_{tm} = \begin{cases} (\dot{\varepsilon}_t / \dot{\varepsilon}_{t0})^{\delta_s} & \text{for } |\dot{\varepsilon}_t| \leq 1 \quad s^{-1} \\ \beta_s (\dot{\varepsilon}_t / \dot{\varepsilon}_{t0})^{1/3} & \text{for } |\dot{\varepsilon}_t| > 1 \quad s^{-} \end{cases} \tag{4.9}$$

where $\delta_s = \left(1 + 8 f_{cm} / f_{cm0}\right)^{-1}$ and $\beta_s = 10^{6\delta_s - 2}$, f_{td} is the dynamic tensile strength, f_{cm} is the mean value of compressive strength, f_{cm0} = 10 MPa [1450 psi], $\dot{\varepsilon}_t$ is the tensile strain rate in the range of 10^{-6} to 160 s^{-1}, and $\dot{\varepsilon}_{t0} = 10^{-6}$ s^{-1}.

4.3.4. Dynamic Concrete Stress-Strain Relations in Tension. For concrete subjected to tensile dynamic loading, two models from CEB-FIP 90 were adapted for uncracked and cracked sections, respectively. For uncracked concrete, a linear stress-strain relationship is assumed as

$$\sigma_t = E_c \varepsilon_t \tag{4.10}$$

where σ_t is the tensile stress, ε_t is the tensile strain, and E_c is the tangent modulus of elasticity. For cracked sections of concrete, a bilinear stress-crack width relationship (see Figure 4.3) was used; it is guaranteed to give stable numerical results (CEB-FIP and ABAQUS)

$$\sigma_t = f_{td}\left(1-0.85\frac{w}{w_1}\right) \quad \text{for} \quad 0.15 f_{td} \le \sigma_t \le f_{td} \tag{4.11}$$

$$\sigma_t = \frac{0.15 f_{td}(w_c - w)}{w_c - w_1} \quad \text{for} \quad 0 \le \sigma_t < 0.15 f_{td} \tag{4.12}$$

where $w_1 = 2G_{Fd} / f_{td} - 0.15 w_c$, $w_c = \alpha_F G_{Fd} / f_{td}$, w is the crack width (mm), w_1 is the crack width (mm) at $\sigma_t = 0.15 f_{td}$, w_c is the crack width (mm) at $\sigma_t = 0$, f_{td} is the dynamic tensile strength (MPa), α_F is the coefficient as given in Table 4.1, and G_{Fd} is the dynamic fracture energy (N-mm/mm^2).

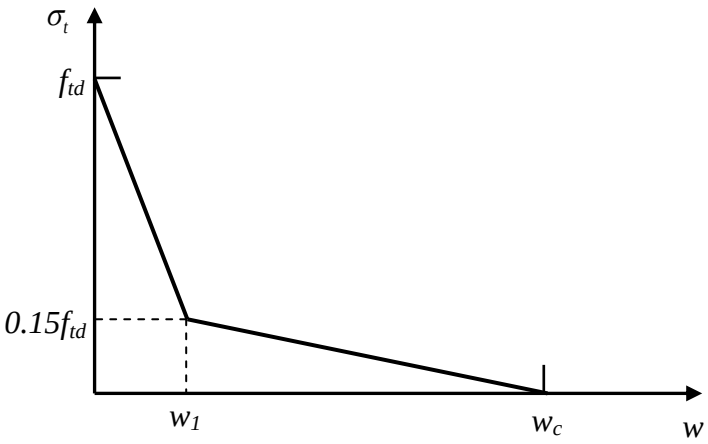

Figure 4.3. Stress-Crack Opening Diagram

One can also define the dynamic fracture energy of concrete, G_{Fd}, as the energy required to propagate a tensile crack of a unit area. Because of the absence of experimental data for G_{Fd}, the static equation recommended by CEB-FIP was adopted and extended to the dynamic case as

$$G_{Fd} = G_{F0}(f_{cd} / f_{cd0}) \tag{4.13}$$

where f_{cd0} = 10 MPa [1450 psi], G_{F0} is the base value of fracture energy that depends on the maximum aggregate size, $d_{\max}$, given in Table 4.1.

Table 4.1. Coefficient α_F and Fracture Energy G_{F0} vs. Max Aggregate Size $d_{\max}$

$d_{\max}$ (mm [in])	8 [0.31]	16 [0.63]	32 [1.26]
α_F	8	7	5
G_{F0} (N-mm/mm^2 [lb-in/in^2])	0.025 [0.143]	0.03 [0.171]	0.058 [0.331]

4.3.5. Dynamic Stress-Strain Relation of Steel Rebar. An idealized stress-strain relation was used in this study. This idealized characteristic is adapted from CEB-FIP as shown in Figure 4.4, in which E_s indicates the modulus of elasticity and f_y denotes the yield stress.

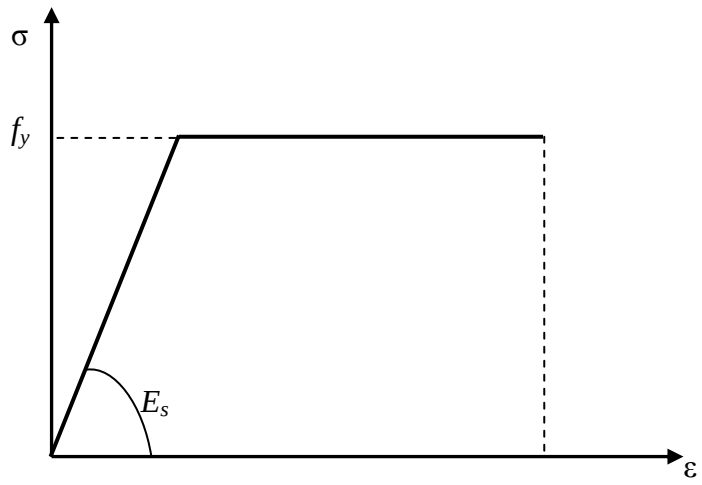

Figure 4.4. Idealized Stress-Strain Relationship for Steel Rebar

4.4. ASSUMED BLAST LOADING

A blast is a very rapid release of stored energy. A major part of the energy is transmitted via blast waves through the surrounding air at a supersonic velocity. The very first mechanical effect of an explosive blast is a forceful blow from the instantaneous pressure jump in its shock front, which is immediately followed by the crushing effect of blast overpressure (pressure above atmospheric) (Kinney and Graham, 1985). The explosive blast wave has an instantaneous rise, a rapid decay, and a relatively short duration. A typical pressure-time history for a blast wave is shown in Figure 4.5. As shown in the figure, the overpressure reaches atmospheric pressure and then falls below it in a short time. An empirical quasi-exponential form can be used to describe a free-air blast wave of the positive phase of a spherical chemical charge (Kinney and Graham, 1985)

$$P(\mathrm{t}) = P_0(1 - t/t_d)e^{-\alpha t/t_d} \tag{4.14}$$

where P(t) is the instantaneous overpressure at time t, $P_0 = (P_m - P_a)$ is the maximum or peak incident overpressure observed when t is zero, P_a is the atmospheric pressure, P_m is the peak pressure when t is zero, *e* is the base of natural logarithms, α is the decay factor, and t_d is the positive pressure duration.

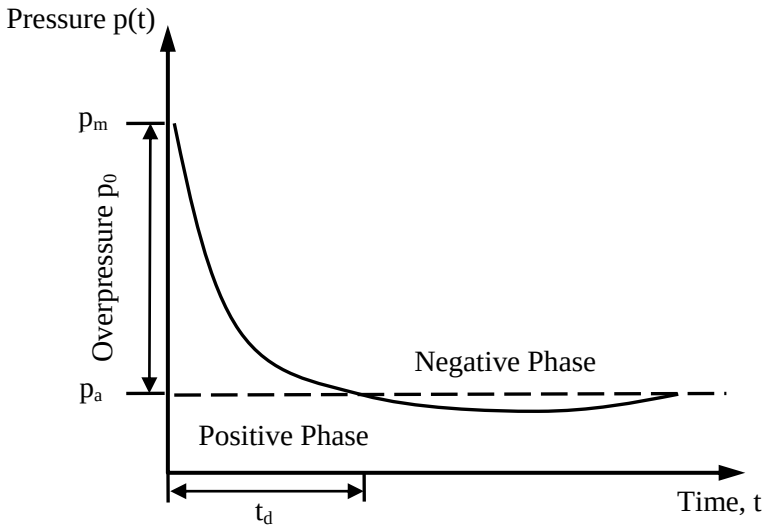

Figure 4.5. A Typical Pressure-Time Curve for a Blast Wave (Kinney and Graham, 1985)

The peak incident overpressure, P_0 (MPa), is calculated by (Kinney and Graham, 1985)

$$P_0 = \frac{808P_a\left[1+\left(\frac{Z}{4.5}\right)^2\right]}{\sqrt{1+\left(\frac{Z}{0.048}\right)^2}\sqrt{1+\left(\frac{Z}{0.32}\right)^2}\sqrt{1+\left(\frac{Z}{1.35}\right)^2}} \tag{4.15}$$

in which the atmospheric pressure, P_a, is taken as 0.10132 MPa [14.7 psi] and Z is the scaled distance (m [ft])

$$Z = \frac{d}{\sqrt[3]{W}} \tag{4.16}$$

where W is the charge weight (kg), and d is the standoff distance (m).

The positive pressure duration in milliseconds is expressed as follows (Kinney and Graham, 1985)

$$t_d = \frac{980\sqrt[3]{W}\left[1+\left(\frac{Z}{0.54}\right)^{10}\right]}{\left[1+\left(\frac{Z}{0.02}\right)^{3}\right]\left[1+\left(\frac{Z}{0.74}\right)^{6}\right]\sqrt{1+\left(\frac{Z}{6.9}\right)^{2}}} \tag{4.17}$$

α is fitted using tabulated data from the book by Kinney and Graham (1985)

$$\alpha = 0.3306Z^4 - 3.184Z^3 + 11.76Z^2 - 20.31Z + 15.12, \quad \text{for Z} < 3.0 \tag{4.18}$$

The column surface close to mid-height will also see reflected pressures, as discussed in Section 3. The magnitude of this reflected pressure is found by multiplying the incident pressure by a reflection coefficient. The reflection coefficient can have values ranging from two all the way up to 20 (Kinney and Graham, 1985). This reflection coefficient is defined as follows (Kinney and Graham, 1985)

$$R_c = \frac{8P_0 + 14P_a}{P_0 + 7P_a} \tag{4.19}$$

Therefore, the peak reflected pressure, P_r, imposed on the surface of a structure can be expressed as follows

$$P_r = R_c P_0 \tag{4.20}$$

The peak reflected pressure is only seen at the point on the column directly in front of the charge. The column surface surrounding this point will also see reflected pressure, but it will have a lower magnitude.

4.5. FINITE ELEMENT RESULTS

4.5.1. General. Due to symmetry, only a quarter portion of each column was modeled. The blast pressure was applied as uniform pressure on the surface of each column using the pressure-time profile defined in Equation 4.14. The negative phase of the blast pressure was ignored, as this portion of the blast will have little effect structurally on the behavior of the columns.

The finite element mesh was generated automatically by ABAQUS. The number of 3-D solid elements used to model the concrete was 480, while the number of shell elements used to model the CFRP and VE material was 240. The rebar elements were modeled as one-dimensional truss elements. The base of the column was assumed to be fixed. Figure 4.6 shows the model of one-quarter of Column 1 and its reinforcement cage.

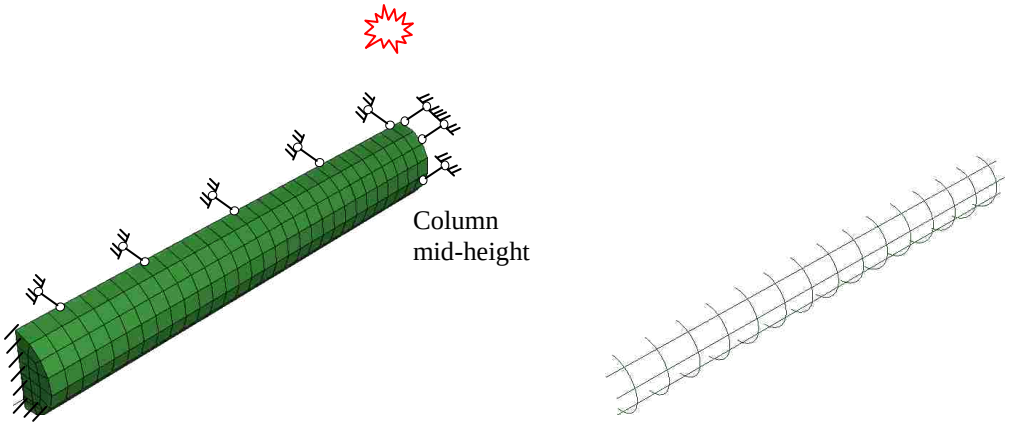

(a) Concrete (b) Rebar

Figure 4.6. Model of One-quarter of Column

4.5.2. Permanent Displacement. For each of the three columns, several load cases were analyzed. Blast loads were calculated and applied to the columns with charge weights ranging from 1.81 to 13.61 kg [4 to 30 lbs], in increments of approximately 2 kg [4.4 lbs]. These results are shown in Figure 4.7 and a comparison to experimental results is given in Section 6. From these results, charge sizes were determined as 1.81 kg [4 lbs], 4.54 kg [10 lbs], and 13.6 kg [30 lbs] as shown in the figure. For simplicity, these charge sizes are hereafter referred to as the 4, 10, and 30 lbs blasts. The 4 lbs charge was expected to cause minimal damage. The 10 lbs charge was expected to cause significant damage to Column 1, and the 30 lbs charge was expected to fail all three Columns.

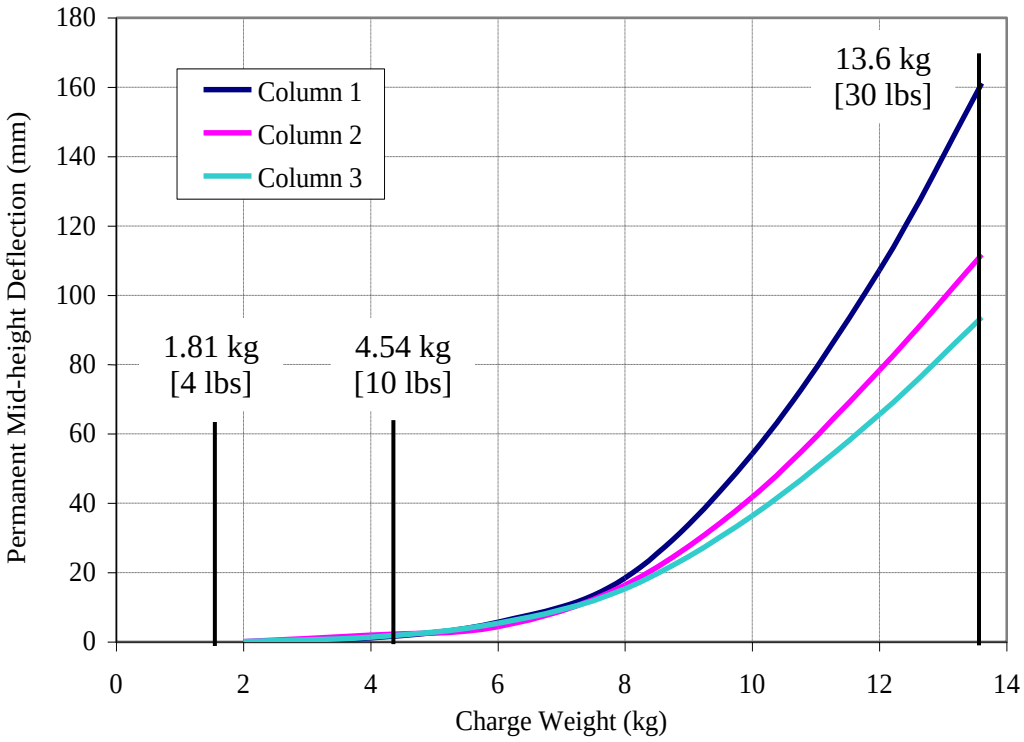

Figure 4.7. Permanent Mid-height Deflection for Varying Charge Weights

5. CONSTRUCTION AND EXPERIMENTAL SETUP

5.1. GENERAL

Due to the size of both the test specimen and the explosive charge, the test was conducted at one of the blast ranges at Fort Leonard Wood Army Base. The specimen was constructed and cured in the High Bay Structures Laboratory at Missouri S&T and then moved to the test site at Fort Leonard Wood by means of a special trailer so as not to damage the specimen during transport. Once the specimen was situated at the test site, coaxial cable crack sensors were installed in each column, the FRP and VE retrofits were applied, and all the instrumentation were set up.

5.2. SPECIMEN CONSTRUCTION

5.2.1. Footing. First, the steel cages that would be placed in the footing and top slab were constructed as shown in Figure 5.1. Each had two layers of reinforcement, and all reinforcement was designed to be symmetrical.

Figure 5.1. One Layer of Reinforcement for Footing and Slab

Once each layer of reinforcement was tied together, they were placed in the forms, and the reinforcement for the column-footing construction joints were tied in place as shown in Figure 5.2. As shown in the figure, standard 90° hooks detailed using ACI 318-05 were utilized at these joints.

Figure 5.2. Formwork and Reinforcement for Footing

5.2.2. Columns and Top Slab. The reinforcement for the columns was tied separately and then attached to the dowel bars that were extended out from the footing. On each column reinforcement cage, six strain gages were attached at the points of maximum positive and negative moment. Since the reinforcement was spliced at the bottom joint, strain gages for negative moment were placed at the top of the column. Two gages were used for positive moment (one for tension and one for compression), and four were used for negative moment in the same fashion. Only two of the gages at the

top of the column would be used, but four were applied for redundancy in case any of the gages were damaged during the pouring of the concrete.

Once the column reinforcement was in place, the top slab was completed much in the same fashion as the footing, and a pipe was placed in the center of the slab so that the charges could be suspended from the top. Since the slab was only 305 mm [12 in] thick, the longitudinal column reinforcement had to be bent into 90° hooks to ensure proper development length. Figures 5.3 and 5.4 show the in-place column reinforcement before placing the forms, and the shoring and formwork for the slab, respectively.

Figure 5.3. Column Reinforcement

Figure 5.4. Shoring and Formwork for Slab

During both concrete pours, six 102 mm [4”] cylinders were prepared in order to verify the concrete compressive strength. One was tested at 7 days, one at 21 days, and four at 28 days. The 28-day compressive strengths of the footing and column/slab concrete, respectively, were 33.1 MPa [4.8 ksi] and 36.5 MPa [5.3 ksi]. The reason for the difference in compressive strengths (besides being different batches of concrete) was that additional water was added to the footing concrete before pouring to make it more workable, while adversely weakening the concrete.

5.2.3. Crack Sensor Installation. Each column had one coaxial cable crack sensor embedded on its back side (tension face). Normally, the sensor’s connector would extend out of the base of the column. In this case, to protect the connector from the blast,

the cable was bent at the base of the column and embedded in the top of the footing as well. To do this, a 13 mm [½"] by 13 mm [½"] groove was cut along the back of the column and in the footing that extended all the way to the edge of the footing. The sensor was then placed in the groove and grouted in using Carter Waters CW100 Precision Grout that was mixed to a dry-pack consistency. Following the first blast, a large portion of the grout was blown out of the column groove. It was determined that since the grout was mixed to a dry-pack consistency, it did not have a high enough water content to create a good bond to the base concrete. To solve this problem, all subsequent grout repairs were done by first brushing Sikatop Plus Component A bonding agent into the groove before packing the grout. This significantly improved the bond between the grout and the concrete. Finally, to protect the sensors' connectors from the blast pressure and debris, steel plates were fabricated and attached to the footing as shown in Figure 5.5.

Figure 5.5. Steel Plate to Protect Sensor Connectors

5.2.4. FRP and VE Application. Column 1 was designated as the control (or benchmark) column and had no strengthening, but it was painted white in order to see the cracking more clearly. Column 2 was strengthened with one layer of CFRP for confinement, and Column 3 was strengthened with the HDM system.

On Column 2, the CFRP was wrapped around the column and encapsulated in Wabo MBrace Saturant Epoxy Encapsulation Resin. The saturant comes in two parts which are mixed just before using. One layer is applied to the concrete before applying the fabric using a nap roller, and then another layer is applied on top of the fabric so that the FRP is completely encapsulated by the saturant. To ensure proper confinement, the fabric was overlapped on the back side of the column by 6 inches.

On Column 3, the first layer of CFRP was applied in the same manner as Column 2. Once the saturant began to harden, the VE material was applied on top and another layer of saturant was brushed onto the VE material. The final layer of CFRP was then applied on top of the VE material in the same matter as the first, except that the fibers were oriented along the length of the column. Figure 5.6 shows the column specimen after strengthening and sensor installation.

5.3. INSTRUMENTATION AND DATA ACQUISITION

5.3.1. Accelerometers and Pressure Transducers. In addition to the crack sensors and the strain gages, each column was instrumented with one accelerometer. The accelerometers were attached by gluing a mounting clip to the back side of each column at mid-height.

Figure 5.6. Final Column Specimen before Testing

On Columns 1 and 2, the clip was glued directly to the concrete and FRP wrap, respectively. On Column 3, a small hole was cut in the outer FRP and VE material so that the clip could be glued to the first layer of FRP. This was done to obtain the

acceleration of the column itself and to avoid a false acceleration from the much less stiff VE material. Figure 5.7 shows one of the accelerometers ready for measurement.

Figure 5.7. Accelerometer

Three pressure transducers were also used to verify the blast pressures calculated by various computer programs. They were placed 5.49 m [18 ft] from the center of the charge and were pointed directly towards it. This distance was selected based on the measurement range of the transducers and the maximum pressure that they would see during the largest blast. Each transducer was mounted in a pipe, embedded in the ground, and covered with a sandbag to ensure no movement occurred. Figure 5.8 shows one of the pressure transducers. Finally, a video camera was placed at a safe distance on top of a berm to record each blast.

Figure 5.8. Pressure Transducer

5.3.2. Data Acquisition. Several different systems were utilized for data acquisition. To acquire the strain and pressure data, a Synergy data recorder at very high sampling rates was used for the blast testing. For the accelerometers, a 'Black Box' data recorder was used. A sampling rate of 20 kHz was used for both the Synergy and 'Black Box' data recorders. For the crack sensors, a Digital TDR Oscilloscope was used along with a pulse generator which is used for dynamic measurements. The Oscilloscope only has one channel, so dynamic measurements were only taken from Column 1, but static measurements were taken on each column both before and after each blast. A laptop was also used to configure and record data from the Synergy and 'Black Box' data recorders. Finally, to protect all of the data acquisition systems from the blast, everything was placed in an aluminum box. The box was situated in a ditch next to the column specimen and covered with 6" x 6" timbers which were covered with plywood and sandbags. All of the cabling for the transducers was piped through PVC pipes which were secured with sandbags. Figures 5.9 and 5.10 show the layout of the instrumentation and the aluminum box containing all of the data acquisition systems, respectively, and Figure 5.11 is a picture of the test site.

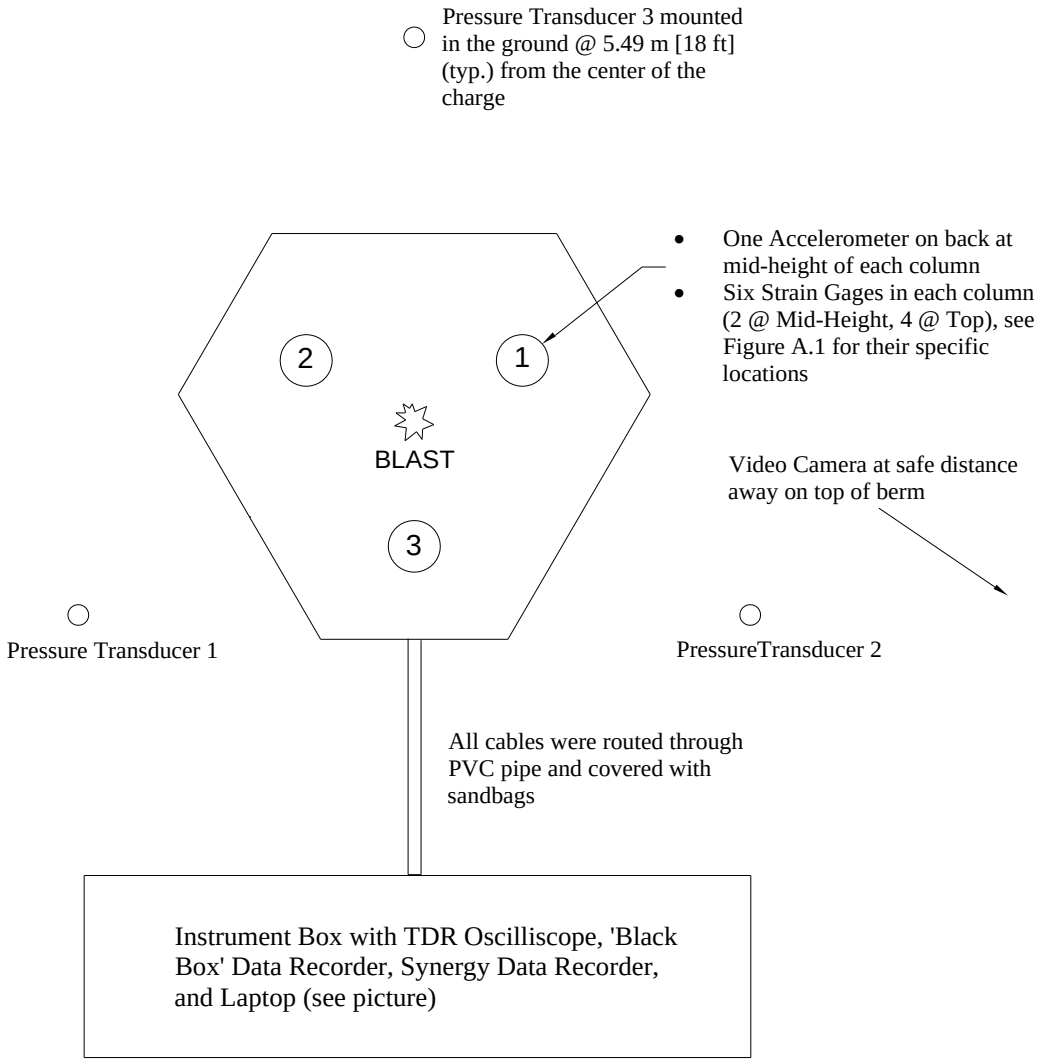

Figure 5.9. Instrumentation Layout

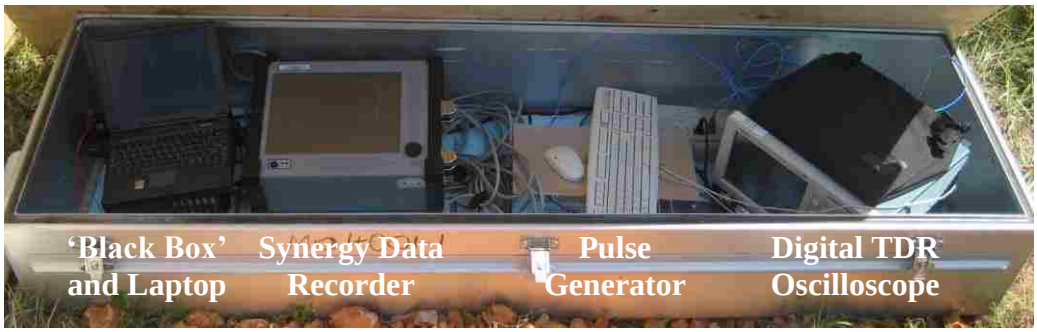

Figure 5.10. Aluminum Box with DAQ Systems

Figure 5.11. Test Site

5.4. CHARGES

Four different charges were used for the testing. Charge weight is always specified in TNT (Trinitrotoluene) equivalence. The TNT equivalence factor is defined as the ratio of the mass specific energy of the explosive compound to the mass specific energy of TNT (4520 kJ/kg). An alternative approach makes use of two conversion factors, depending on whether the peak overpressure or impulse is to be matched (Mays and Smith, 1995).

The first two charges were made up of pentolite cast boosters, each having a TNT equivalence of 1.1, for a total charge weight of 2 kg [4.4 lbs] of TNT (hereafter referred

to as the 4 lbs blasts). The third charge was made up of nine pentolite cast boosters (1.1 lbs each) and a 0.25 lbs pentolite cast booster, for a total charge weight of 4.6 kg [10.2 lbs] of TNT (hereafter referred to as the 10 lb blast). The fourth charge was made up of ammonium nitrate fuel oil (ANFO), with a TNT equivalence of 0.83, along with 2 pentolite cast boosters for a total charge weight of 13.6 kg [30 lbs] of TNT.

The first charge was placed on a piece of plywood which was sitting on a cardboard Sonotube, as shown in Figure 5.12.

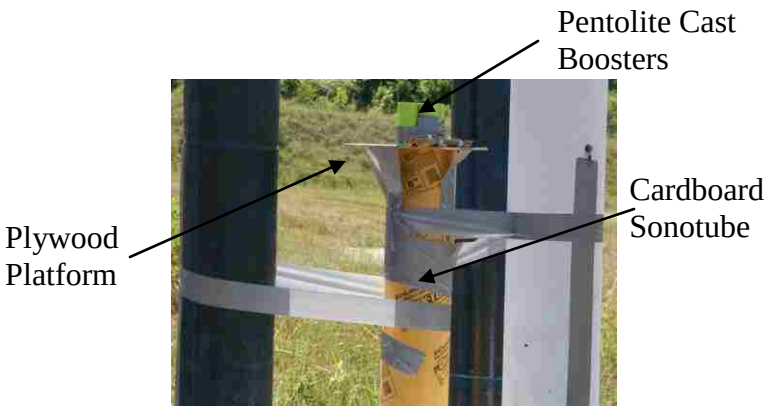

Figure 5.12. First 4 lbs Charge

After the first blast, all the columns were inspected. It was determined that the plywood had caused some of the damage to Column 3. While debris damage would be a normal occurrence during a blast, it was not considered in this study due to difficulty in prediction. Therefore, the second 4 lbs charge and the 10 lbs charge were suspended from the top slab. The ANFO used for the 30 lbs charge was put in a bag and placed on top of a cardboard Sonotube (with no plywood).

6. EXPERIMENTAL RESULTS

6.1. GENERAL

After the completion of each blast, a thorough inspection of each column was performed. Crack patterns were observed, and the damage to each column and its respective strengthening system was assessed. It should be noted that on the two columns that were strengthened, cracks cannot be observed visually. For these columns, the coaxial cable crack sensors were used to locate cracks after each blast. The data from these measurements are discussed in the latter part of this section. Following the completion of the 30 lbs blast, some of the FRP and VE materials were removed from the columns in order to expose the concrete beneath and observe cracking that may have occurred under the FRP. This is discussed in Section 6.4. Data from the strain gages, pressure transducers, and accelerometers are also presented in the latter part of this section.

6.2. SPALLING OF CONCRETE FROM BLAST LOADING

There are two types of spalling that can occur in concrete during a blast load — direct spalling and scabbing (TM 5-1300, 1990).

6.2.1. Direct Spalling. Direct spalling of an element is the result of a tension failure in the concrete normal to its free surface and is caused by the shock pressures of an impinging blast wave being transmitted through the element (TM 5-1300, 1990). The Army Technical Manual TM 5-1300 (1990) describes direct spalling as follows:

"When a shock front strikes the surface of a concrete element, compression stresses are transmitted from the air to the element. This stress disturbance propagates through the element in the form of a compression wave, and upon reaching the rear surface, is reflected as a tension wave identical in shape and magnitude to the compression wave. During the return passage, if the tension stresses in the reflected wave exceed the stresses in the compression wave plus the tensile capacity of the concrete, the material will fracture with that part of the element between the rear surface and the plane of failure being displaced from the remainder of the element. A portion of the stress wave is trapped in the failed section and contributes to its velocity. The part of the stress wave which remains within the main section continues to propagate with additional reflections and concrete fractures until its magnitude is reduced to that level below which spalling does not occur.

Direct spalling generally results in the formation of small concrete fragments. The size of the fragments is attributed to the nonuniformity of the shock wave (close-in effects) and the further distortions of the wave during its propagation through the element (nonhomogeneous material, inelastic effects, etc.). The thickness of concrete between the rear surface of the element and the centroid of the rear face reinforcement (cover concrete) is the usual depth of concrete dynamically disengaged from the element. Although the concrete between the layers of reinforcement may be cracked to some extent, it is confined by the flexural and shear reinforcement, thus preventing its disengagement."

Concrete elements subjected to a close-in blast are generally accelerating before or soon after spalling takes place. This accelerated motion of the element in turn accelerates spalled fragments. The velocities of these fragments can be as high as several hundred feet per second. It is these fragments that can be a hazard to human occupants, and they are often a main cause of casualties from an explosion. Given some material properties and some of the blast wave parameters, it is possible to predict when spalling will occur. It will occur for (TM5-1300, 1990)

$$\frac{Vi_r}{T_c P_r} \le 1.0 \quad \text{when} \quad \frac{P_r}{\sigma_u} \ge 1.0 \tag{6.1}$$

$$\frac{Vi_r}{T_c P_r} > 1.0 \quad \text{when} \quad \frac{P_r T_c P_r}{\sigma_u Vi_r} \ge 1.0 \tag{6.2}$$

where $\sigma_u = 0.1 \text{ f '}_c$, $V = \sqrt{E_c / \rho}$, P_r is the peak normal reflected pressure (kPa [psi]), σ_u is the tensile strength of the concrete (kPa [psi]), V is the velocity of the compression wave through concrete (mm/ms [in/ms]), i_r is the normal reflected impulse (kPa-ms [psi-ms]), T_c is the thickness of the concrete element (mm [in]), f'_c is the static compressive strength of the concrete (kPa [psi]), E_c is the modulus elasticity of the concrete (kPa [psi]), and ρ is the mass density of the concrete (kg/mm^4 [lb-ms^2/in^4]). Figure 6.1 shows Equations 6.1 and 6.2 graphically. It should be noted that Equations 6.1 and 6.2 were developed for walls, which behave differently than columns during a blast due to clearing effects. Also plotted on the graph are the spall predictions for the 4, 10, and 30 lbs blasts. The equations predict a much greater spall area than was seen in the experiments. This is likely due to the geometry of the circular columns, and that fact that the equations were developed for walls and not columns.

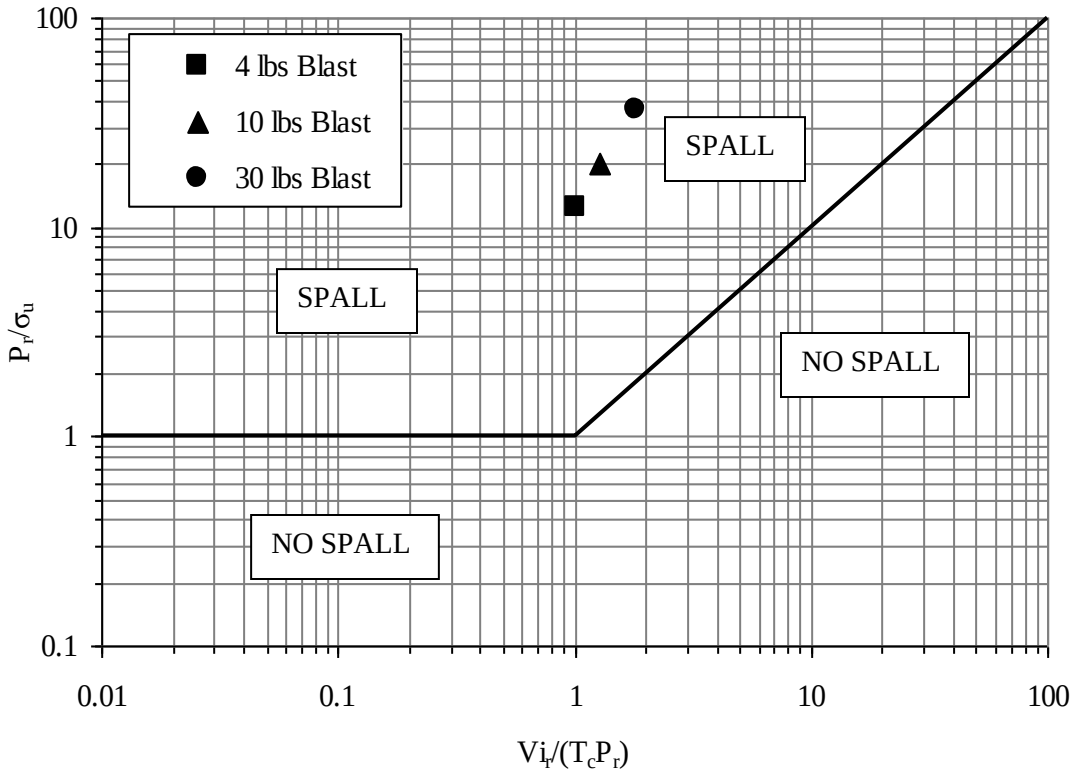

Figure 6.1. Spall Threshold for Blast Waves Loading Walls (TM5-1300, 1990)

6.2.2. Scabbing. Scabbing of concrete elements is the result of a tension failure in the concrete normal to its free surface and is associated with large deflections. In the later stages of the ductile response mode of an RC element, extremely large deflections are developed producing large strains in the flexural reinforcement and, consequently severe cracking and/or crushing of the concrete perpendicular to the free surfaces (TM 5-1300, 1990). Since the tension and compression strains are highest at the surface and since the shear reinforcement in the later stages of deflection confines the core concrete, damage to the cover concrete is more severe than damage to the core. The applied loads having long since passed, the element is in a stage of deceleration at these large deflections (TM 5-1300, 1990). Therefore, the velocities of scabbed fragments, which

are equal to the velocity of the element at $\theta = 5°$ (start of scabbing), are lower than the velocities of direct spalled fragments. However, the velocities of scabbed fragments may also be on the order of several hundred feet per second.

6.3. COLUMN BEHAVIOR

6.3.1. First 4 lbs Blast. For the first blast, the charge was placed on top of a square piece of plywood which was positioned on top of a cardboard concrete form (Sonotube). Unfortunately, this method ended up causing some damage to the columns that was not purely a result of the blast pressure, which will be discussed later.

Column 1, the unretrofitted benchmark column, sustained damage mainly on its back side (the side not directly facing the blast). All of the concrete was still intact, but a portion of the grout that was used to cover up the crack sensors had spalled off as shown in Figure 6.2. It was later determined that the spalling of the grout materials is due mainly to the poor bond between the concrete and grout since relatively dry grout was used to keep it from flowing out of the groove. Cracking was mainly concentrated on the back side of the column halfway up from the base. There was also some cracking on the front side of the column (the side facing the blast) near the base and the top of the column. The crack patterns that were observed agreed with basic structural mechanics theory for a column with support conditions defined as fixed-fixed. During the blast, the back side of the column at mid-height will be subjected to tension, while the back side of the column at the supports will be subjected to compression. The cracks at the top and bottom were mainly horizontal flexural cracks. Also on the front side of the columns,

there were tension cracks about every 152 mm [6 in] corresponding to the locations of the circular ties.

Figure 6.2. Damage to Sensor Grout on Column 1 after 1st 4 lbs Blast

At the mid-height of the column, however, the cracks were not all horizontal flexural cracks. Some were vertical and diagonal cracks. Figure 6.3 (a) and (b) show views of the cracking on the front and back side, respectively, of Column 1.

Before continuing with subsequent blasts, the sensor grout needed to be repaired. For the initial application of the grout, no primer was brushed into the groove. When the grout was repaired after the first blast, Sikatop Plus Component A was brushed into the groove before packing the grout. This proved to provide a much better bond between the concrete and the grout, and was therefore used for all other grout repairs.

(a) Front Side (b) Back Side

Figure 6.3. Column 1 Cracks after 1st 4 lbs Blast

Column 2, which was retrofitted with one layer of CFRP for confinement, sustained very little damage. Some of the MBrace saturant had been blown off on the front side of the column at the location of the blast, but most of the fibers were still intact. Figure 6.4 shows a side view of the damage area on Column 2.

Figure 6.4. Damage Area of Column 2 after 1st 4 lbs Blast

Column 3, which was retrofitted with the HDM system, sustained little damage as well. As mentioned previously, a Sonotube and a piece of plywood were used to elevate the charge to the mid-height of the columns. After inspecting the damage to Column 3, it was determined that most of the damage was caused by shards of plywood. This is evident by the fact that there were sharp pieces of wood embedded in the FRP and VE material after the blast. As with Column 2, almost all of the damage to Column 3 was concentrated at the mid-height. Figure 6.5 shows the damage on the front side of Column 3.

Figure 6.5. Damage to Front of Column 3 after 1st 4 lbs Blast

6.3.2. Second 4 lbs Blast. Due to the damage from the plywood incurred during the first 4 lbs blast, the second charge was suspended from the top of the specimen using a rope. It should be noted that in a realistic explosion, there will most likely be flying debris that can cause significant damage upon impact. However, this investigation is limited to studying the effects of a pure explosion, rather than damage from debris impact.

Much like the first blast, all of the concrete on Column 1 was still intact, but some of the sensor grout had spalled off. As was expected, most of the cracks that resulted from the second blast were extensions of the cracks from the first blast. It was also noticed that there was very little additional cracking on the top and bottom portions of the column. Most of the cracking from the second blast was concentrated at the mid-height,

as is shown in Figure 6.6 (a) through (c) below. This could be a result of redistribution of moments caused by damage from the initial 4 lbs blast. Significant cracks at both ends of the column from the first blast allowed the release of end moments from the second blast. The cracking sustained from the second blast is shown in red, while the blue lines indicate the locations of cracks sustained from the first blast.

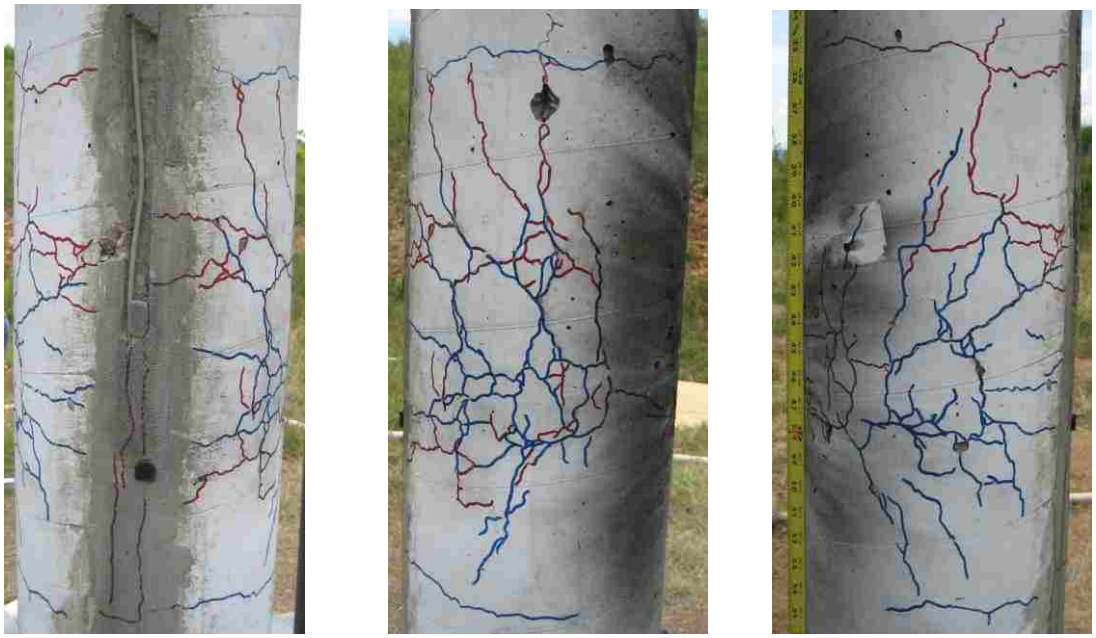

(a) Back Side (b) Side View (c) Opposite Side View

Figure 6.6. Crack Pattern on Column 1 after 2nd 4 lbs Blast

Column 2 sustained very little additional damage from the second blast. Much like the first blast, some of the saturant was blown off. There were a few additional FRP fibers that were ruptured, but as a whole the FRP wrapping was still intact and performed well. As with the first blast, the damage was limited to the front side of the column closest to the blast. There was no damage on the back side of the column. There was,

however, a crack that developed at the top of the column directly where the column joins the top slab. Figure 6.7 (a) and (b) show the damage to Column 2.

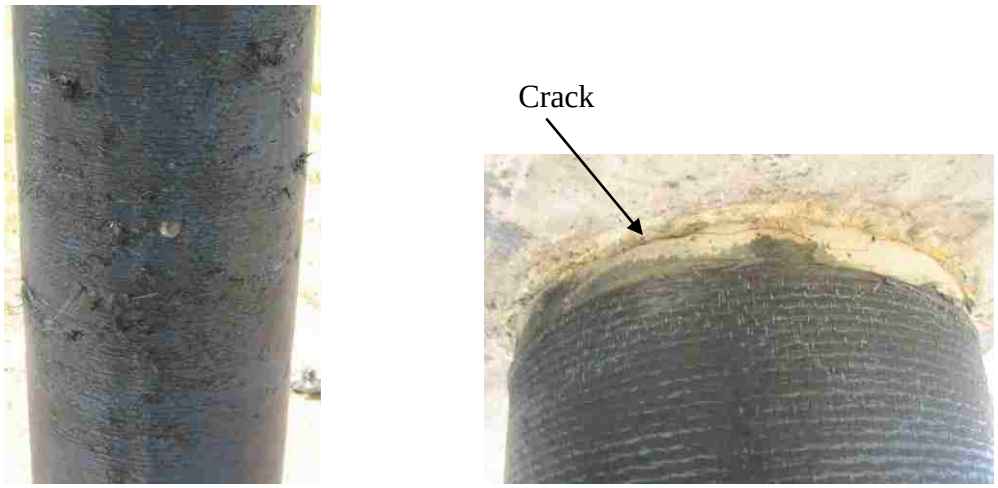

(a) Degradation at Mid-Height (b) Crack at Top

Figure 6.7. Damage to Column 2 after 2nd 4 lbs Blast

Column 3 sustained very little additional damage from the second blast. This perhaps validates the statement that the damage caused by the initial blast was mostly a result of the plywood debris impacting the FRP. There was a strip of FRP that started to peel down the side of the column, but this was minor damage that would not affect the integrity of the retrofit. The failure of this strip was not a result of the fibers rupturing. It merely separated in the direction parallel to the fibers. Figure 6.8 shows the damage to the front side of Column 3 and also the strip of FRP on the side of the column that started to peel off.

Figure 6.8. Damage to Column 3 after 2nd 4 lbs Blast

6.3.3. 10 lbs Blast. For the 10 lbs blast, the charge was suspended from the top of the specimen in the same manner as the second 4 lbs blast so as to prevent damage from debris impact.

Column 1 sustained significant damage from the 10 lbs blast. A large portion of the cover concrete had spalled off on the back side near the mid-height, and a small amount had been blown off of the front side (side facing the blast). However, the concrete core was still intact, there was no hinging in the column, and the permanent deformation was negligible. This observation indicated the column was still structurally stable and repairable to its full capacity. Figure 6.9 (a) and (c) show two different views of the damage to Column 1, and Figure 6.9 (b) shows that there was no permanent deformation in the column after the blast.

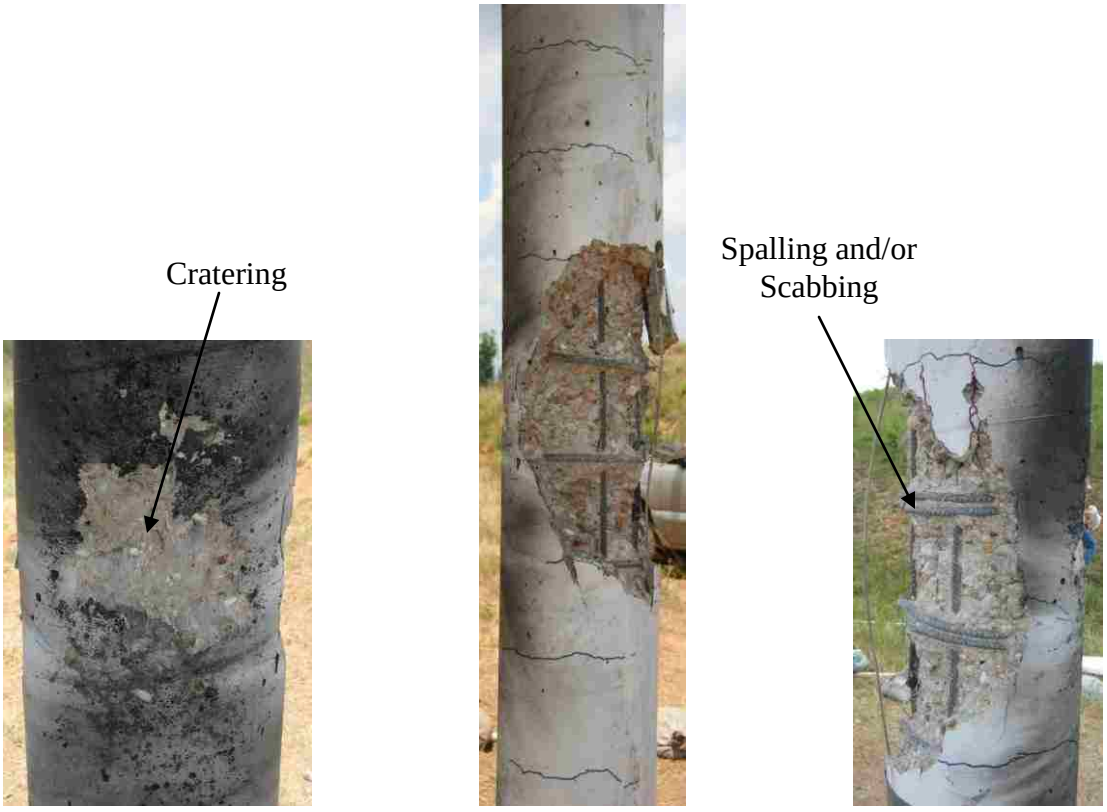

(a) Front Side (b) Side View (global) (c) Side View (local)

Figure 6.9. Damage to Column 1 after 10 lbs Blast

Column 2 sustained some additional damage from the 10 lbs blast, but it was not as severe as the damage to Column 1. Some of the saturant had been blown off and a few of the FRP fibers were ruptured on the front side of the column, but as a whole the system was still in fairly good shape. The back side of the column sustained no damage at all, and the crack at the top construction joint seemed to have slightly enlarged. There was no permanent deformation in the column, and as far as one could tell from visually inspecting the damage, the column was still structurally sound. Figure 6.10 (a) through (c) show some of the damage to Column 2. The damage shown in Figure 6.10 (a) could partially be a result of the fireball generated during the blast. The resilience of the

polymer resin encasing the CFRP could have been degraded from the heat, and this might have caused some of the fibers to rupture.

(a) Front Side (b) Back Side (c) Crack at Top

Figure 6.10. Damage to Column 2 after 10 lbs Blast

Column 3 sustained a similar amount of damage as Column 2. A few of the FRP fibers were ruptured on the front side, but there was no damage on the back side of the column. Most of the damage to the FRP was limited to the separating of fibers at multiple locations. There was also no permanent deformation in the column, and it could be deemed structurally sound. Figure 6.11 shows the damage to the front side of Column 3.

Figure 6.11. Damage to Front Side of Column 3 after 10 lbs Blast

6.3.4. 30 lbs Blast. For the 30 lbs blast, the explosive material (ANFO) was placed inside of a bag and positioned on top of a cardboard Sonotube – very similar to the first 4 lbs blast but without the piece of wood.

Column 1 sustained very significant damage from the 30 lbs blast. Most of the cover concrete around the mid-height had been blown off, and there was a hinge at the mid-height. There were also very large cracks near the top and bottom of the column at the same locations as the cracks that had formed during previous blasts. Some of the cover concrete had spalled off on the back side at both the top and bottom. Although the column had sustained damage during the previous blasts, the crack patterns that were observed after the 30 lbs blast indicated that the column fixity (fixed-fixed) had remained the same regardless of the damage. The column was structurally unsafe. Figure 6.12 (a) through (c) show different views of the damage.

(a) Mid-Height (b) Top Portion (c) At Base

Figure 6.12. Damage to Column 1 after 30 lbs Blast

Column 2 sustained significant damage during the 30 lbs blast but not as severe as the damage to Column 1. On the front side, the FRP at the mid-height was damaged significantly, and the FRP at the top and bottom had minor damage. The FRP on the back side of the column was fairly intact and sustained little damage. There was a hinge at the mid-height, and a small amount of concrete had been blown off on the front side where the FRP was damaged. Since the column had failed at the mid-height, it could be concluded that it was unsafe structurally. Figure 6.13 (a) and (b) show different views of the damage to Column 2.

(a) Front Side (b) Back Side

Figure 6.13. Damage to Column 2 after 30 lbs Blast

Column 3 sustained similar damage to Column 2. On the front side of the column close to the charge, as shown in Figure 6.14 (a), a significant portion of the VE layer had been either punctured or melted due to high temperature effects, but all of the concrete and inner FRP sheet on the column were still intact. On the back side of the column, as shown in Figure 6.14 (b), some of the outer FRP layer and VE layer had become delaminated from the inner FRP layer. These delaminations were likely caused by the reflected tensile wave generated when the blast wave reached the rear surface of the column. The column had hinged at the mid-height, but did not have as much permanent deflection as the other two columns, as will be discussed in the next section. Since the column had failed at the mid-height, it could be concluded that it was unsafe structurally. Figure 6.14 (a) and (b) show different views of the damage.

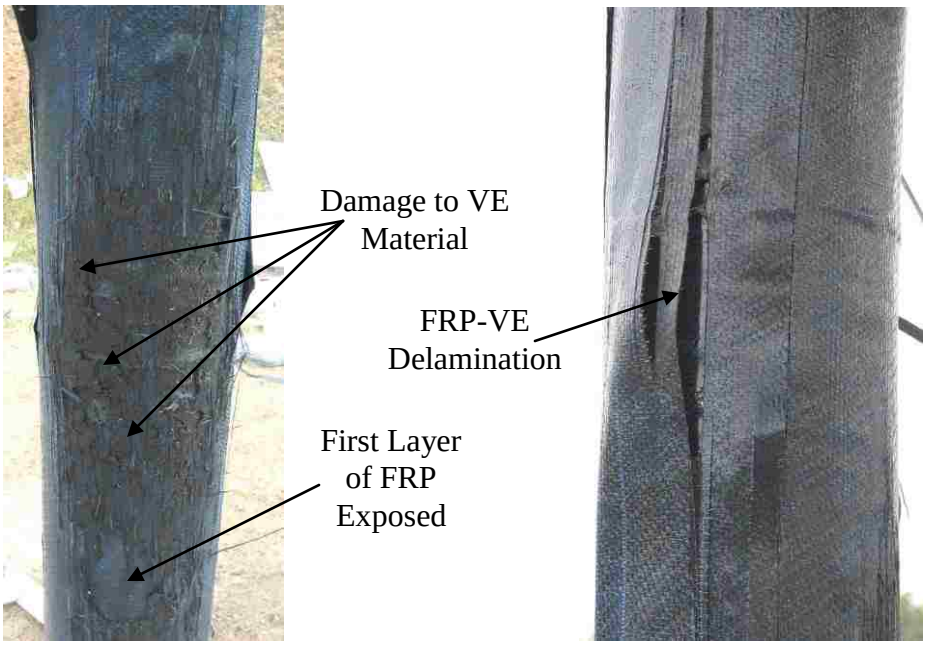

(a) VE Damage on Front Side (b) FRP and VE Delamination on Back Side

Figure 6.14. Damage to Column 3 after 30 lbs Blast

6.4. FRP-VE REMOVAL AND OTHER OBSERVATIONS

Following the completion of the 30 lbs blast, some of the FRP and VE materials were removed from Columns 2 and 3. This allowed a thorough inspection of the condition of the concrete underneath the strengthening materials and exposed any cracks that may have formed which would otherwise have only been detected by the crack sensors.

Removal of the FRP from Column 2 led to some interesting findings. Most cracks were located at the failure hinge. At the base of the column, one large crack was present on the tension side as seen in Figure 6.15 (a), but no other cracking was visible. The FRP was not removed at the top of the member, but it can be assumed that similar cracking occurred at that location since the loading was symmetric and the boundary

conditions at the joint were the same as those at the base (except for the splice in the flexural reinforcement at the base). There were several cracks at the mid-height of the column as seen in Figure 6.15 (b), but they were all flexural cracks, and there were no diagonal or horizontal cracks like those seen on the benchmark column in Figure 6.6. Except for local damage on the front face of the column at the mid-height, all of the concrete was intact, and there was no sign of loose materials. This indicates that the FRP protected the concrete from spalling and from further cracking such as that seen on Column 1 in Figure 6.6.

(a) Crack at Base

(b) Hinge at Mid-Height

Figure 6.15. Post-Test Inspection on Column 2

Removal of the FRP and VE materials from Column 3 led to similar findings. Most of the outer FRP and VE materials along the column were removed, but only the

inner layer of FRP that was around the failure hinge was removable because of its bond to the concrete. There was a small amount of spalling on the front of the column, but not enough to expose the reinforcement. The crack pattern on the back side of the failure hinge was similar to that of Column 2, but the cracks were narrower as shown in Figure 6.16.

Figure 6.16. Back Side of Column 3

As noted previously, the 30 lbs blast resulted in flexural failure of all three columns by creating a hinge at the mid-height of each member. It was noticed, however, that Column 3 did not have as much permanent deflection as Columns 1 and 2. Since it is very difficult to measure this deflection in the field, pictures were taken of each column and the deflection was estimated. Figure 6.17 shows a comparison of the three columns and their respective deflections following the 30 lbs. blast.

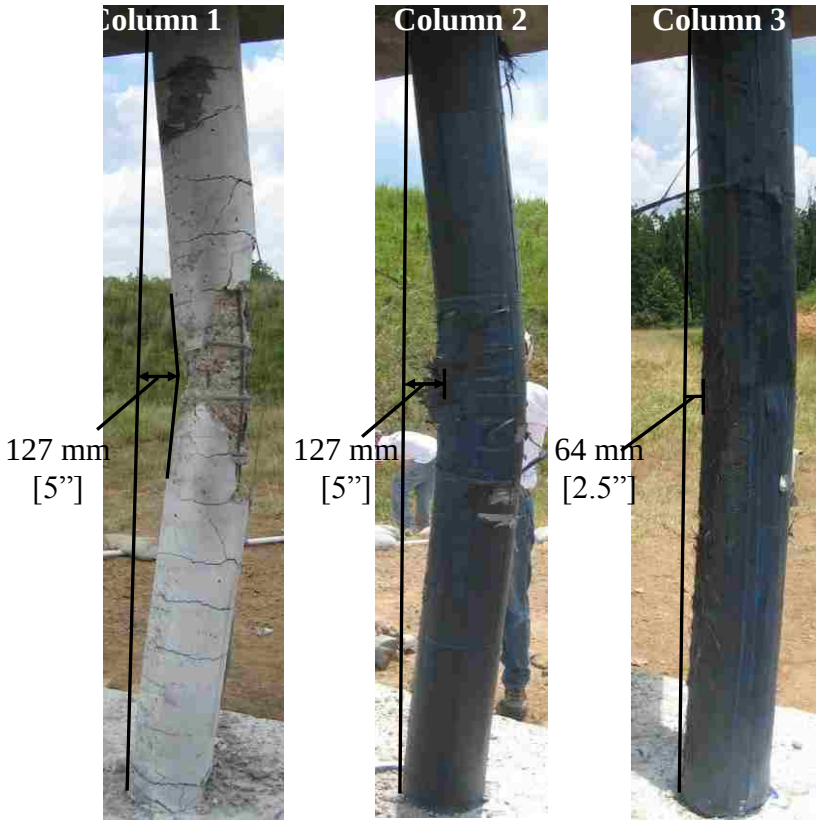

Figure 6.17. Comparison of Permanent Deflections

It can be seen from Figure 6.17 that after the blast, Column 3 had 50% less permanent deflection than the other two columns. This means that a significant amount of the energy generated by the blast was dissipated. Columns 2 and 3 both had a layer of FRP designed to confine the concrete. This confining action increases the ductility of the section, thereby dissipating energy when significant inelastic deformations are present. However, since Columns 2 and 3 had the same confinement FRP layer, and Columns 1 and 2 had approximately the same amount of permanent deflection, this additional energy dissipation could only be explained by the addition of the VE material. This alone provides evidence that this FRP-VE strengthening system adds a significant amount of

damping or wave-modulating effects, and reduces strength degradation by protecting the FRP confinement on the RC column.

6.5. COMPARISON WITH FE MODEL

The simulated deformations which were presented in Figure 4.7 coincide fairly well with the experimental results. As shown in the curves, there was virtually no permanent deflection resulting from the 4 and 10 lbs charges, as was the case in the experiments. After the 30 lbs blast test, Columns 1 and 2 had permanent deflections of 127 mm [5 in], and Column 3 had a permanent deflection of 64 mm [2.5 in]. The FE model overestimates this deflection for Columns 1 and 3, but slightly underestimates it for Column 2. These differences could result from a number of factors. In the model, the blast load was applied as a uniform pressure. In reality, a very close-in blast creates extremely non-uniform pressures, and these pressures can be very high at the points close to the charge. By applying the pressure as uniform over the entire surface of the column, the total load is overestimated. Another important point that should be noted is that the FE model does not take progressive damage into account. Each FE run was carried out assuming no initial damage to the column. In reality, each blast caused cracking which resulted in some stiffness degradation. The 10 lbs blast also caused significant spalling. This stiffness degradation and removal of material were not taken into account in ABAQUS. Also, any blast creates a fireball that can have extremely high temperatures, but this cannot be modeled in ABAQUS. For a close-in blast, these high temperatures can have adverse effects on the structural elements, and especially on any type of FRP

strengthening system, as FRP does not perform well at high temperatures. All of these items would have contributed to inaccuracies in the model which could not be avoided.

6.6. PRESSURE, STRAIN, AND ACCELEROMETER MEASUREMENTS

6.6.1. General. Due to problems with the transducers and data acquisition systems, only strain and pressure data from the first blast were obtained. Unfortunately, the data that was recorded from the accelerometers was questionable and is not included in this thesis. However, crack sensor data was acquired for all the blasts and is reported later in this section.

To prevent losses in the connecting cables for the crack sensors, the crack sensor instrumentation had to be placed near the test specimen. To avoid having instrumentation in two separate places, all the instrumentation was placed inside the aluminum box and well protected with Styrofoam, plywood, and sandbags. Although the box was well protected, there were still some problems with the setup. First, there were several pieces of instrumentation equipment inside the box. It was very hot outside during the testing, and enclosing the instrumentation restricted air flow causing the equipment to get too hot. It is well known that electrical equipment runs better when it is kept cool, and this could have been one of the problems. Second, even though the box was well protected, it still saw some movement during the blast. This jolted the equipment inside, causing some of it to lock up. There are two possible solutions to these problems: (1) put the instrumentation much farther away from the test specimen, and (2) if the instrumentation is going to be close to the test specimen, build a concrete protective shelter for it that is well-anchored to the ground so there is no possibility of movement.

6.6.2. Pressure Transducer Data. The pressure transducers were placed 5.49 m [18 ft] away from the center of the blast and pointed directly at the charge. The main purpose of the pressure transducers was to verify the blast pressure calculations. Ideally, pressure would be measured directly on the columns. However, due to the difficulty associated in mounting the transducers at the surface of the column combined with their high cost and high probability of being destroyed during the blast, placing the transducers at a distance is an acceptable method of verifying the blast pressures.

A.T. Blast, a simple computer program developed by Applied Research Associates, Inc., was used to calculate blast parameters for the 4 lb blast. The program calculated the peak reflected pressure and positive duration as 134 kPa [19.44 psi] and 2.75 ms, respectively. These values agree very well with the pressure measurements taken from Transducers 1 and 3, as shown in Figure 6.18 and Figure 6.20, and fairly well with the measurements from Transducer 2 that are presented in Figure 6.19. Transducer 2 shows a slightly higher peak pressure and there are also two spikes in pressure which indicate that some debris came in contact with the transducer. Since two of the transducer measurements agree with the predicted pressure, the blast parameters at the face of the column can be calculated with confidence.

Since the calculated blast pressures agree with the measurements, the blast parameters at the face of the column (stand-off distance of 457 mm [18 in] from the center of charges) can be obtained from the A.T. Blast computer software. Table 6.1 gives these parameters for each of the different charge sizes.

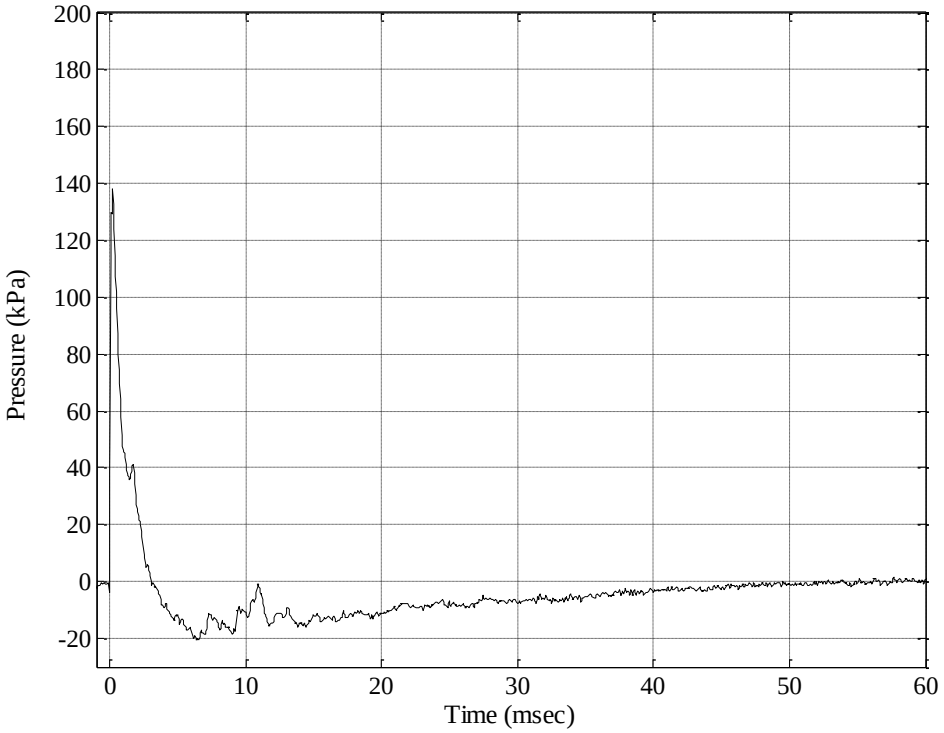

Figure 6.18. Pressure Measured from Transducer 1

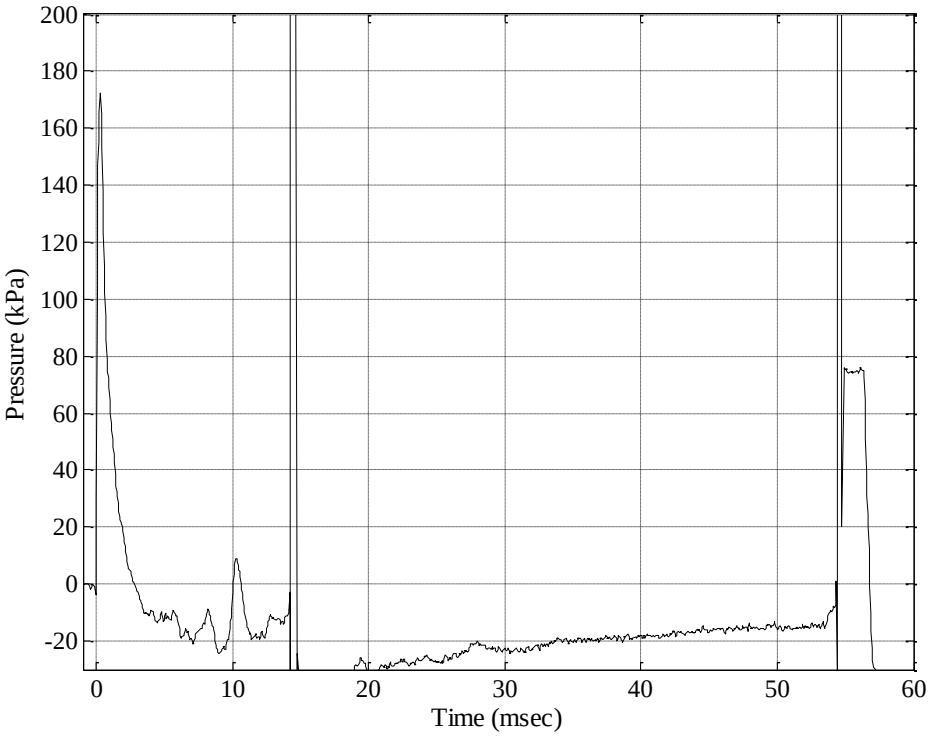

Figure 6.19. Pressure Measured from Transducer 2

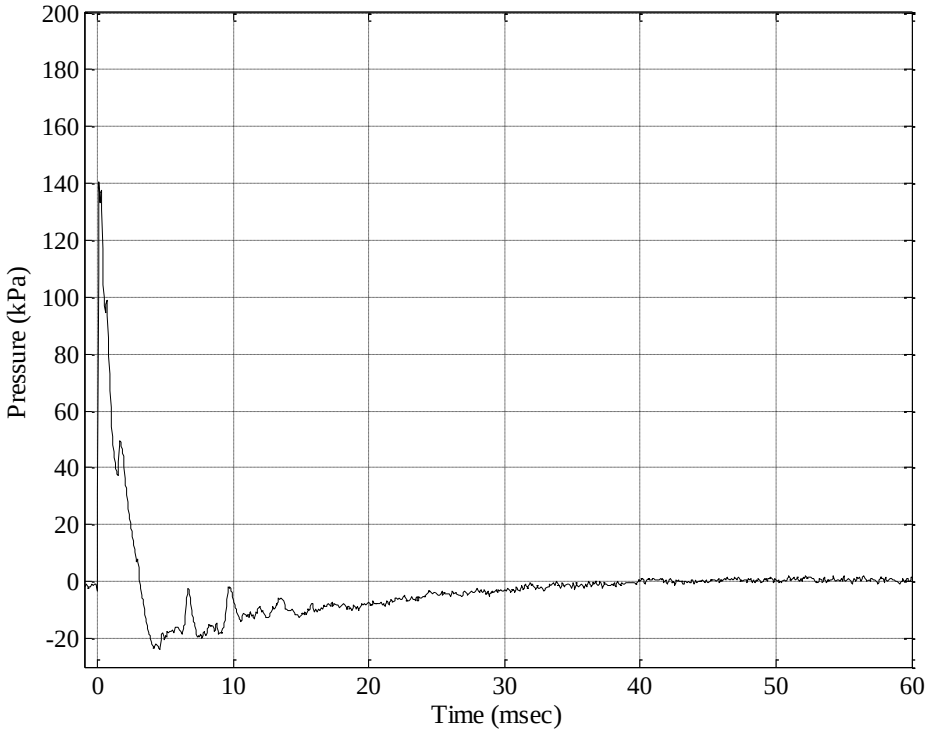

Figure 6.20. Pressure Measured from Transducer 3

Table 6.1. Shock Wave Parameters at the Column Face

Charge Weight (TNT) (kg [lb])	Velocity (m/ms [ft/ms])	Time of Arrival (ms)	Maximum Reflected Pressure (MPa [psi])	Impulse (kPa-ms [psi-ms])	Positive Pressure Duration (ms)
4.4	2.72 [8.91]	0.11	70.22 [10185]	4888 [709]	0.14
10.2	3.26 [10.71]	0.10	112.1 [16254]	10160 [1474]	0.18
30.0	4.11 [13.49]	0.08	198.9 [28844]	27120 [3933]	0.27

6.6.3. Strain Gage Data. As discussed in the experimental setup section, six strain gages were instrumented on each column, and four of them were used to record data—two at mid-height (positive moment region) and two at the top (negative moment region). Comparisons of strain gages from the three columns are shown in Figure 6.21

through Figure **6.24**, while each strain gage measurement is plotted separately along with an FFT analysis of each in Figures Figure **6.25** through Figure **6.46**. Figure 6.21 only shows the strain measurements at the mid-height of Columns 1 and 2. This is due to a mix-up in strain gage wiring during the construction process. When the grooves for the crack sensors were being cut, some of the strain gage wires were accidentally cut. When the wires were repaired, one of them was connected to the wrong strain gage. However, the three remaining figures show measurements from all three columns at different locations.

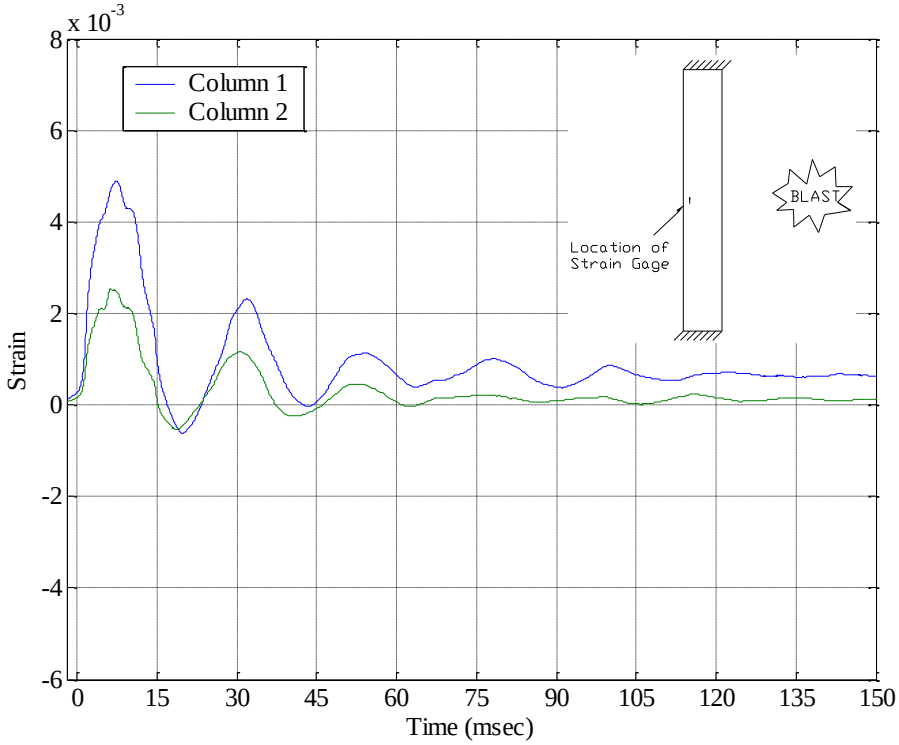

Figure 6.21. Strain for Positive Moment – Tension Side

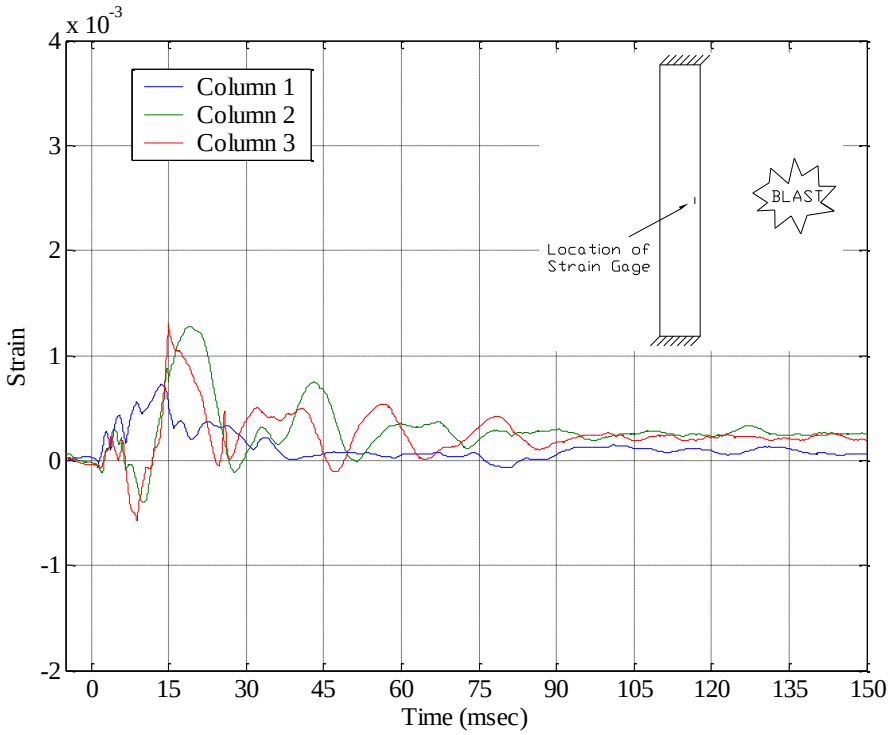

Figure 6.22. Strain for Positive Moment – Compression Side

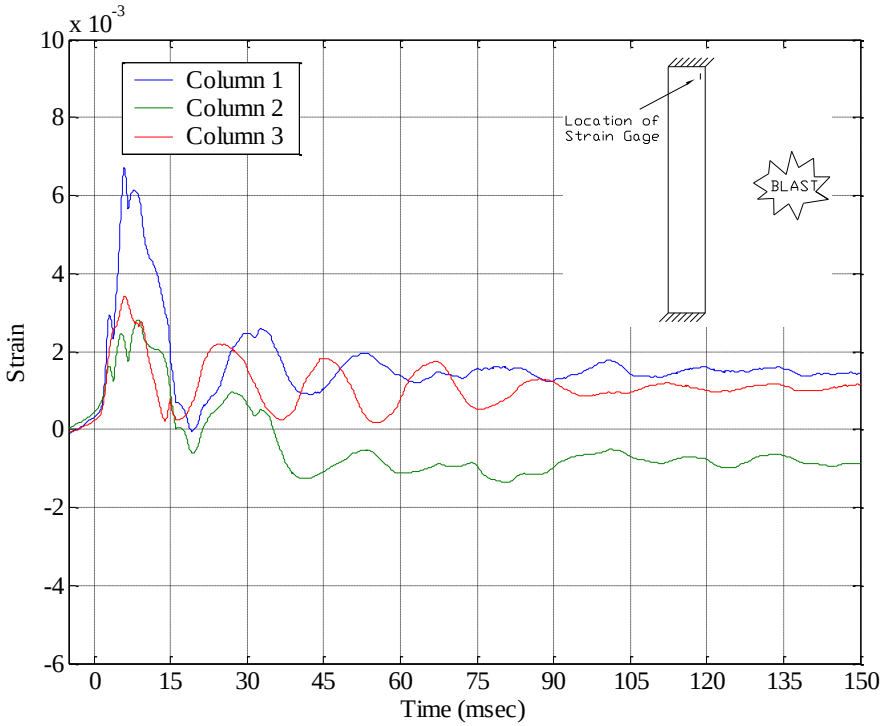

Figure 6.23. Strain for Negative Moment – Tension Side

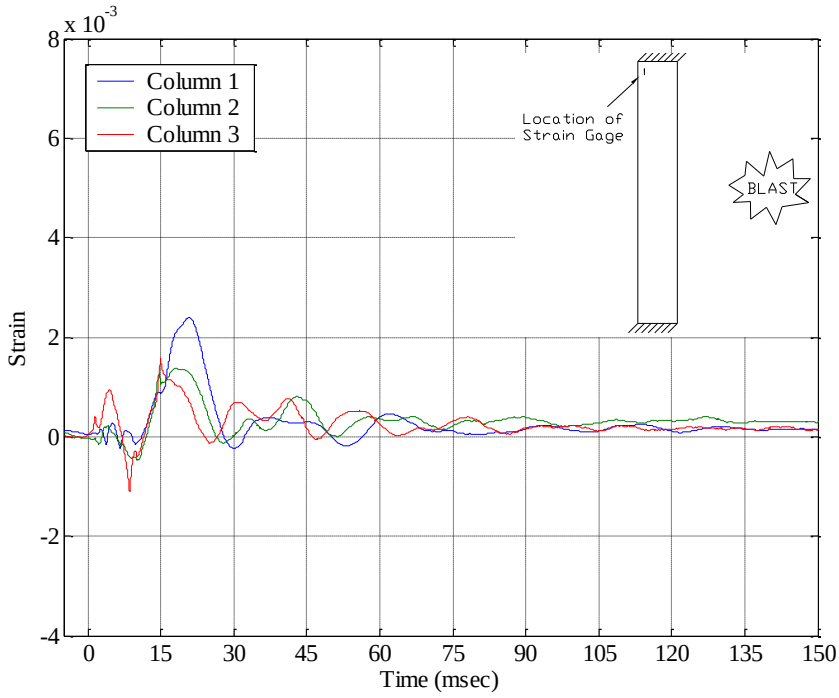

Figure 6.24. Strain for Negative Moment – Compression Side

It can be seen in Figure 6.21 that the FRP wrap resulted in a decrease in strain in the tension steel at mid-height. This trend is also evident in Figure 6.23. Although the strain gage in Column 2 appears to have come off the rebar (Figure 6.23. Strain for Negative Moment – Tension Side), there is still a clear reduction in strain when comparing Column 1 to 3.

Figure 6.25 through Figure 6.46 show each of the strain measurements from the first 4 lbs blast along with each associated FFT analysis. By examining the FFT plots, it is apparent that the two strengthening methods had an effect on the natural frequency characteristics of the columns. For Column 1, the 1st mode frequency appears to be about 42 Hz. This increases to approximately 45 Hz on Column 2 and to approximately 50 Hz on Column 3. These increases are due likely to the resistance to cracking provided

by the FRP wrap and the FRP-VE system. Less cracking would result in higher stiffness which would result in an increase in the natural frequency. As discussed earlier, this reduction in cracking was verified when the FRP and VE materials were removed from Columns 2 and 3, revealing very little cracking underneath.

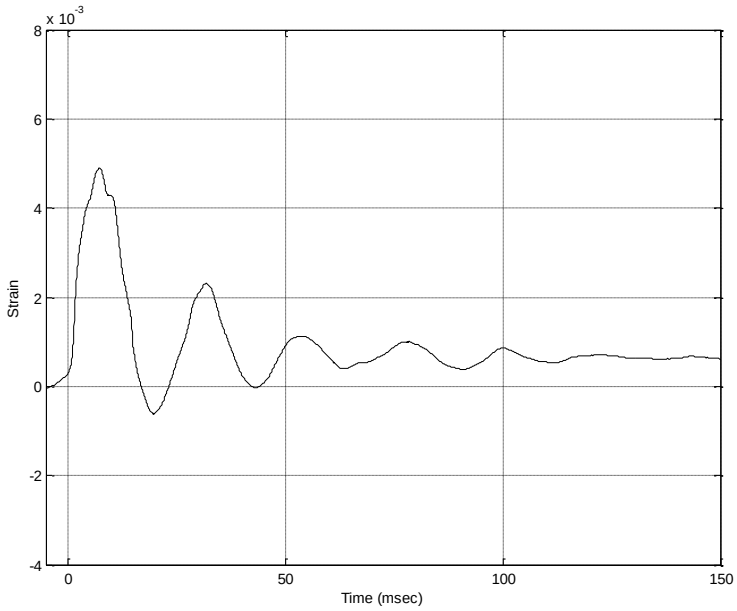

Figure 6.25. Column 1: Positive Moment (Tension) Strain

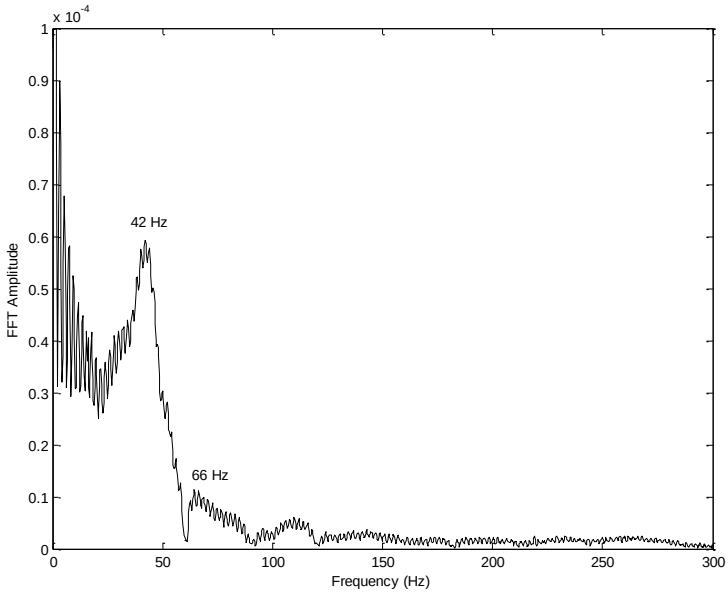

Figure 6.26. Column 1: Positive Moment (Tension) Strain FFT Plot

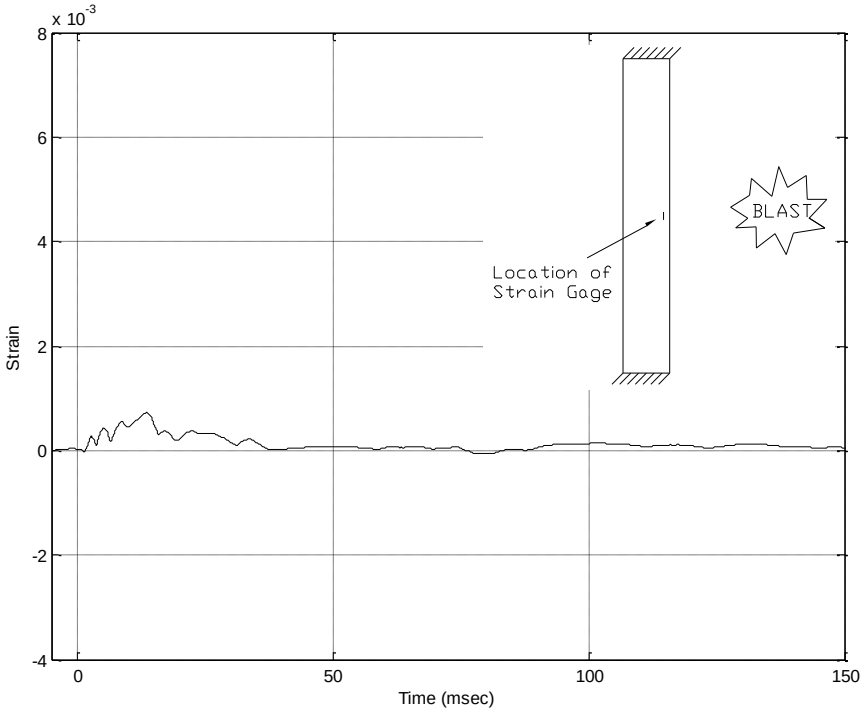

Figure 6.27. Column 1: Positive Moment (Compression) Strain

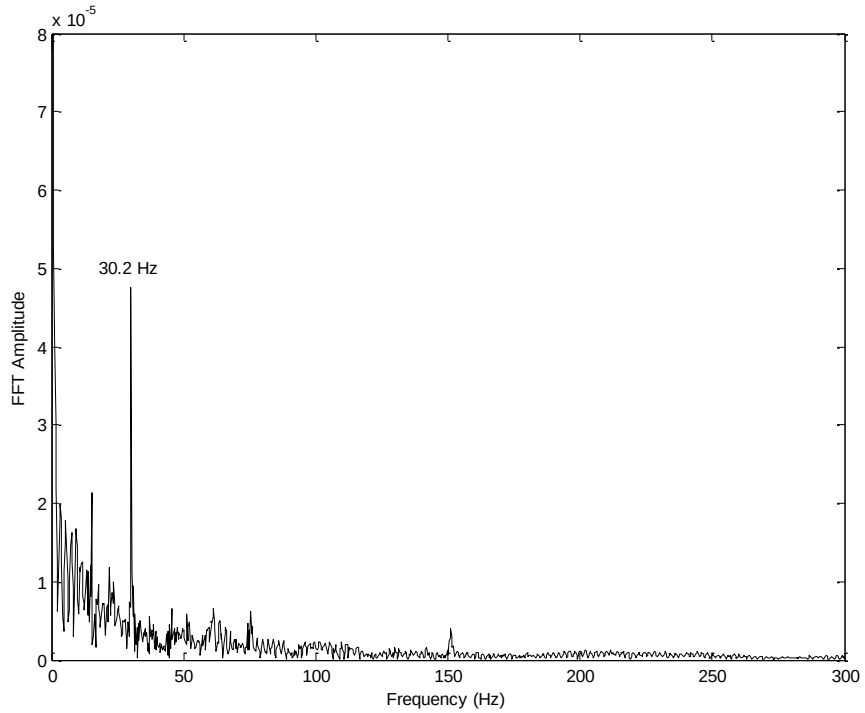

Figure 6.28. Column 1: Positive Moment (Compression) Strain FFT Plot

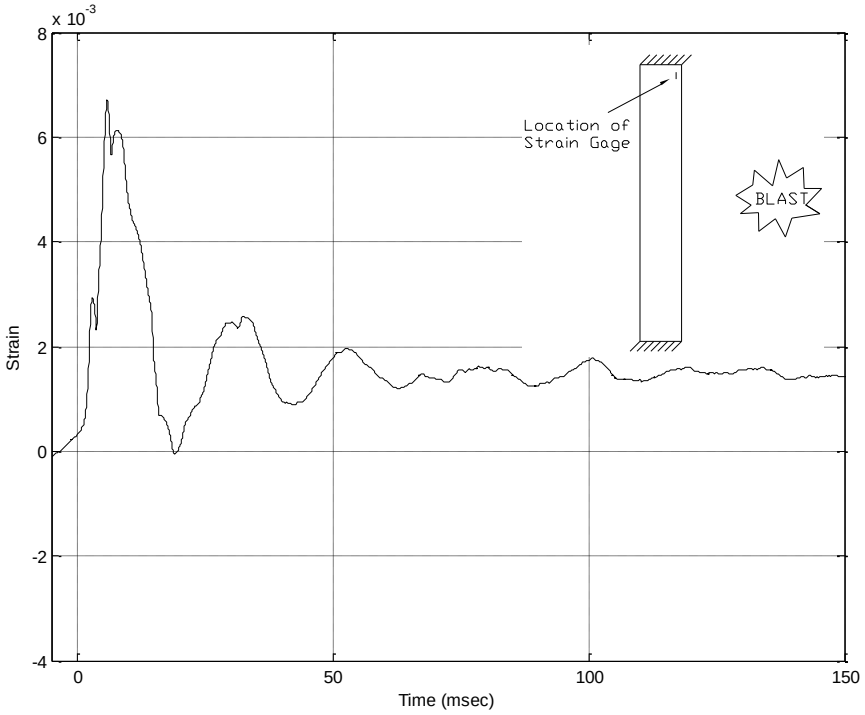

Figure 6.29. Column 1: Negative Moment (Tension) Strain

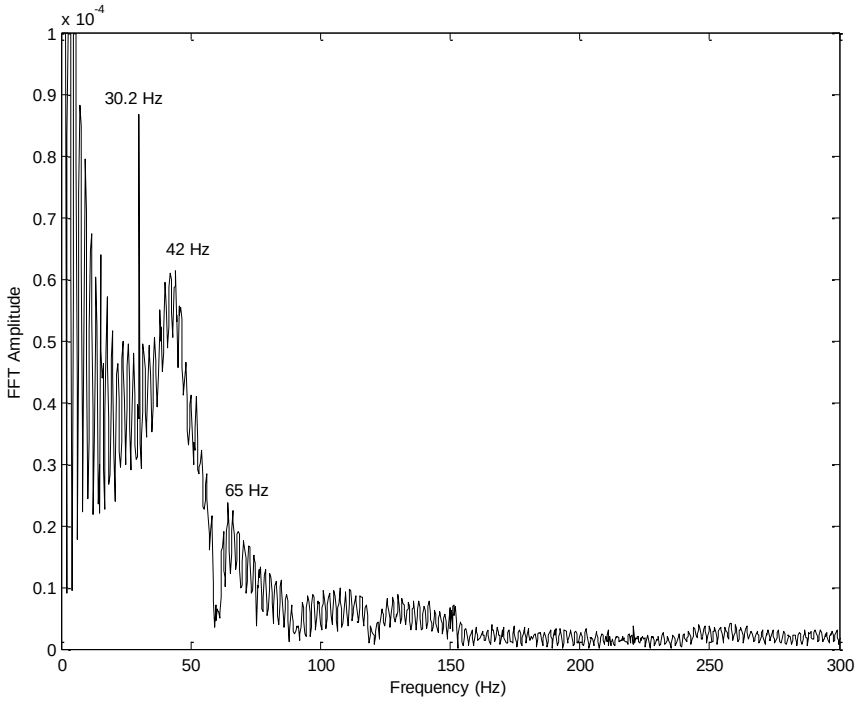

Figure 6.30. Column 1: Negative Moment (Tension) Strain FFT Plot

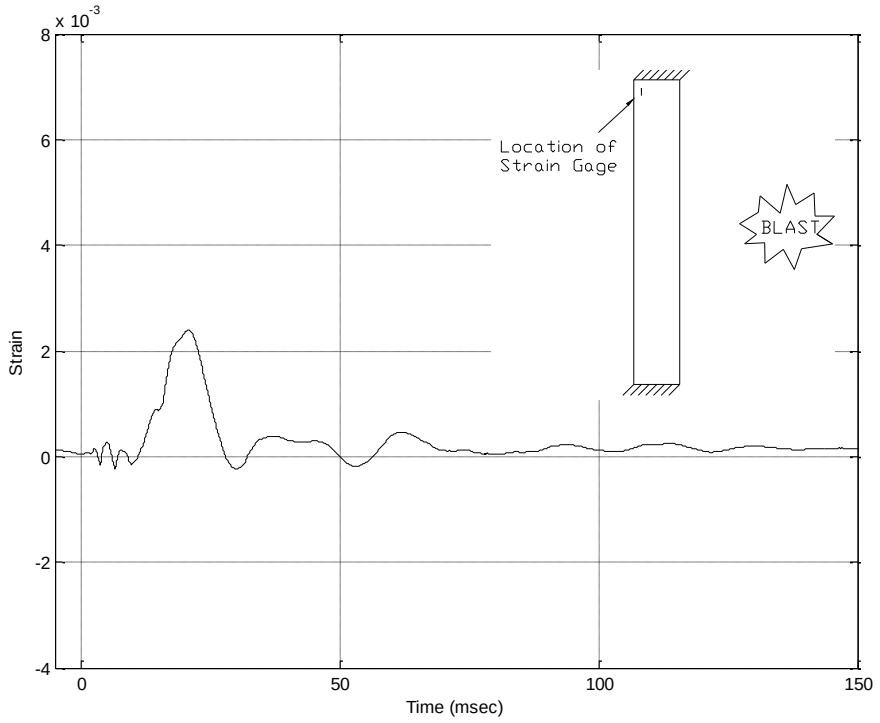

Figure 6.31. Column 1: Negative Moment (Compression) Strain

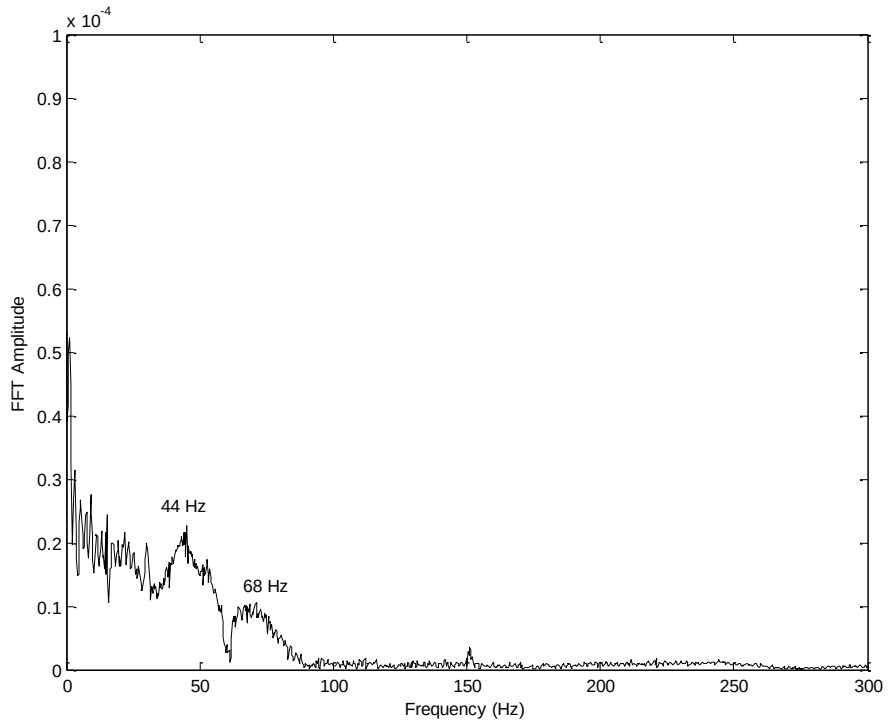

Figure 6.32. Column 1: Negative Moment (Compression) Strain FFT Plot

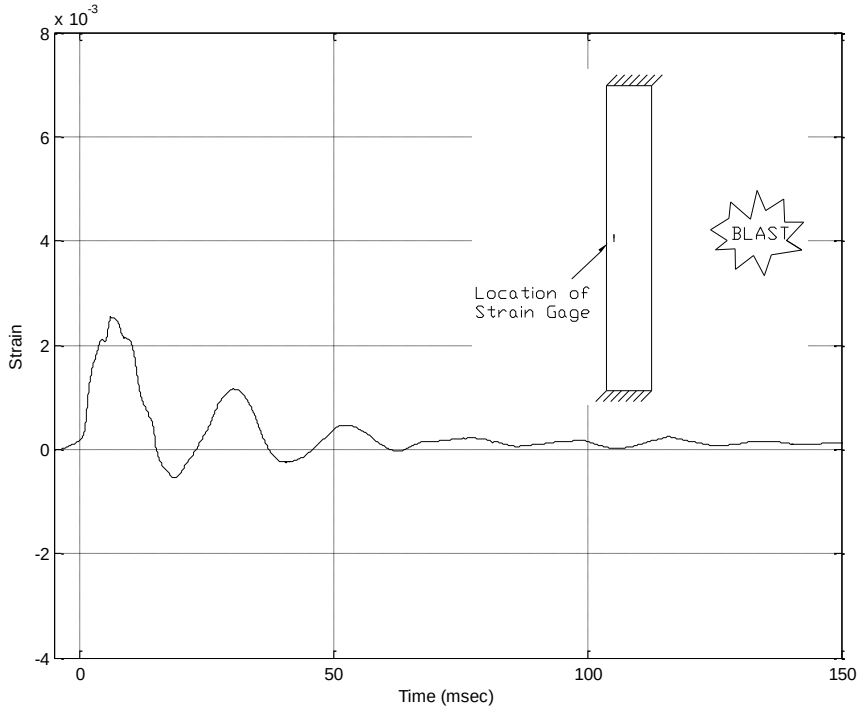

Figure 6.33. Column 2: Positive Moment (Tension) Strain

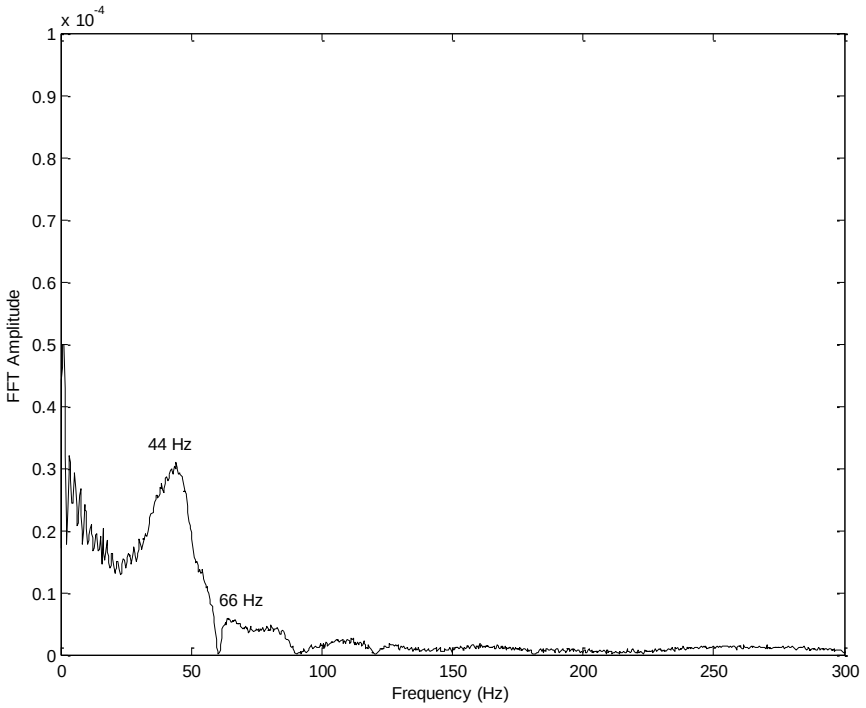

Figure 6.34. Column 2: Positive Moment (Tension) Strain FFT Plot

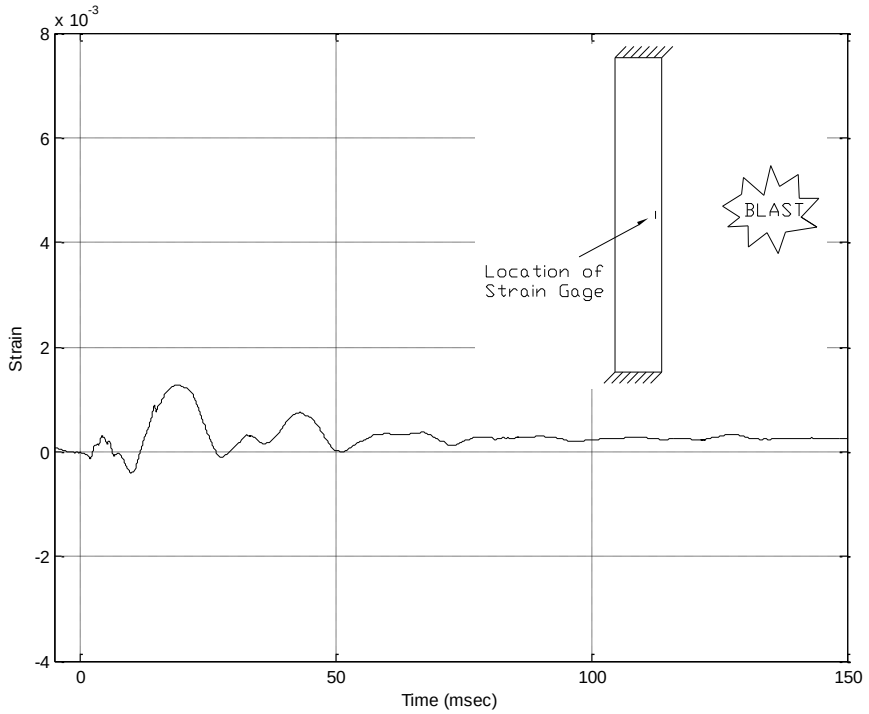

Figure 6.35. Column 2: Positive Moment (Compression) Strain

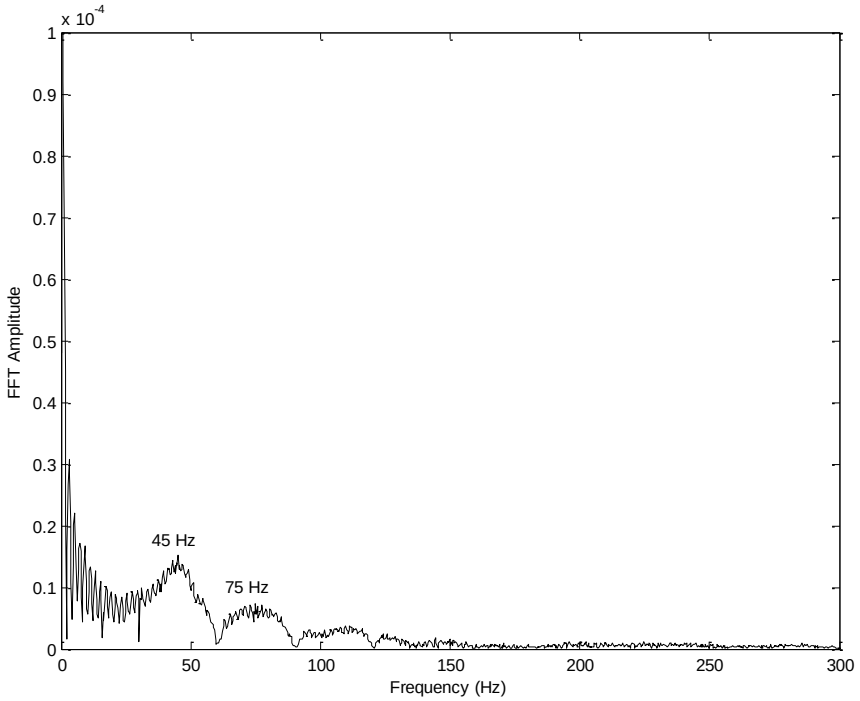

Figure 6.36. Column 2: Positive Moment (Compression) Strain FFT Plot

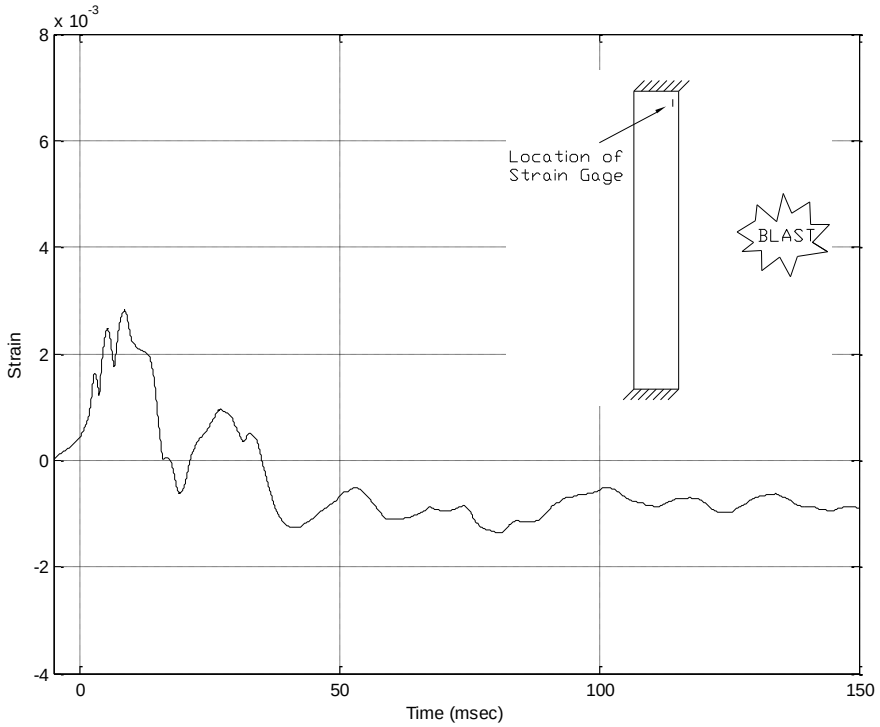

Figure 6.37. Column 2: Negative Moment (Tension) Strain

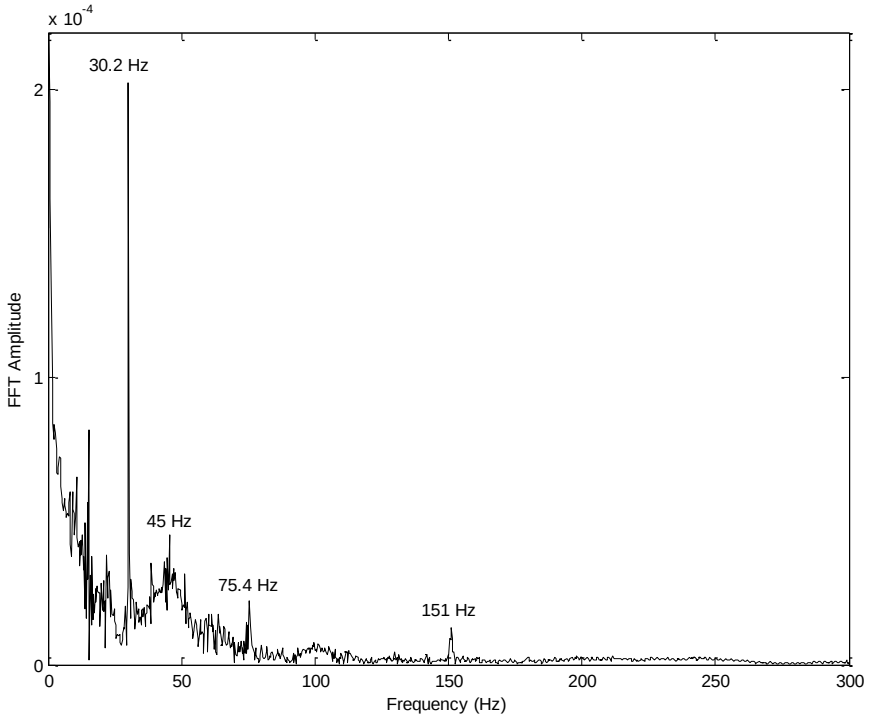

Figure 6.38. Column 2: Negative Moment (Tension) Strain FFT Plot

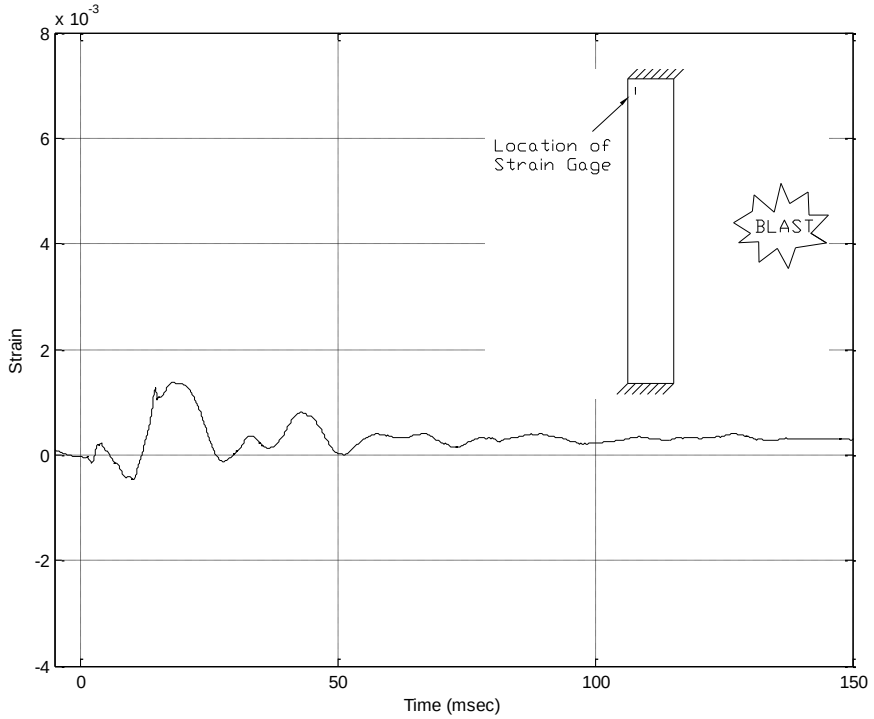

Figure 6.39. Column 2: Negative Moment (Compression) Strain

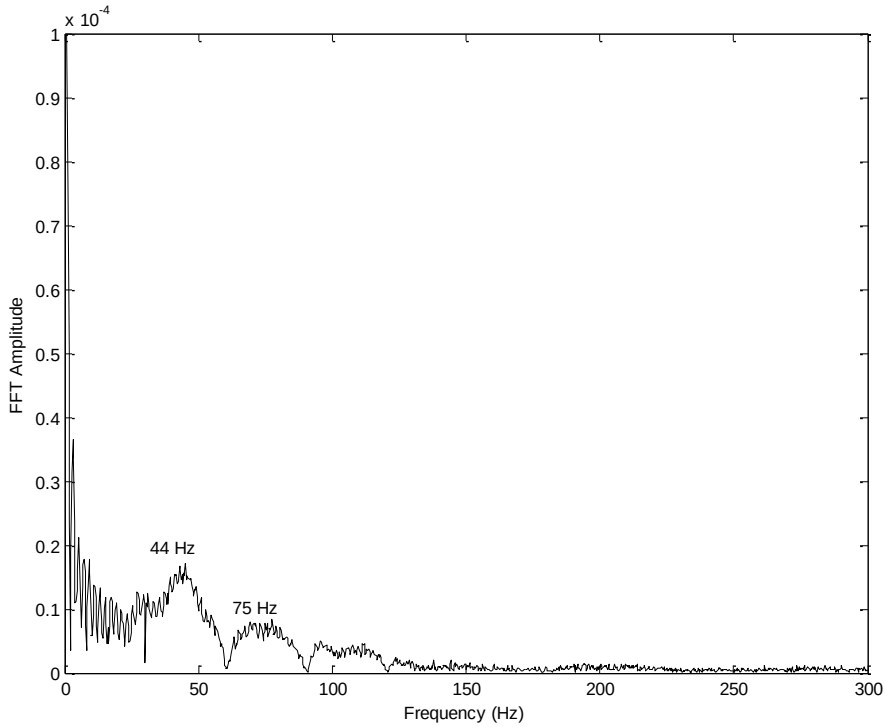

Figure 6.40. Column 2: Negative Moment (Compression) Strain FFT Plot

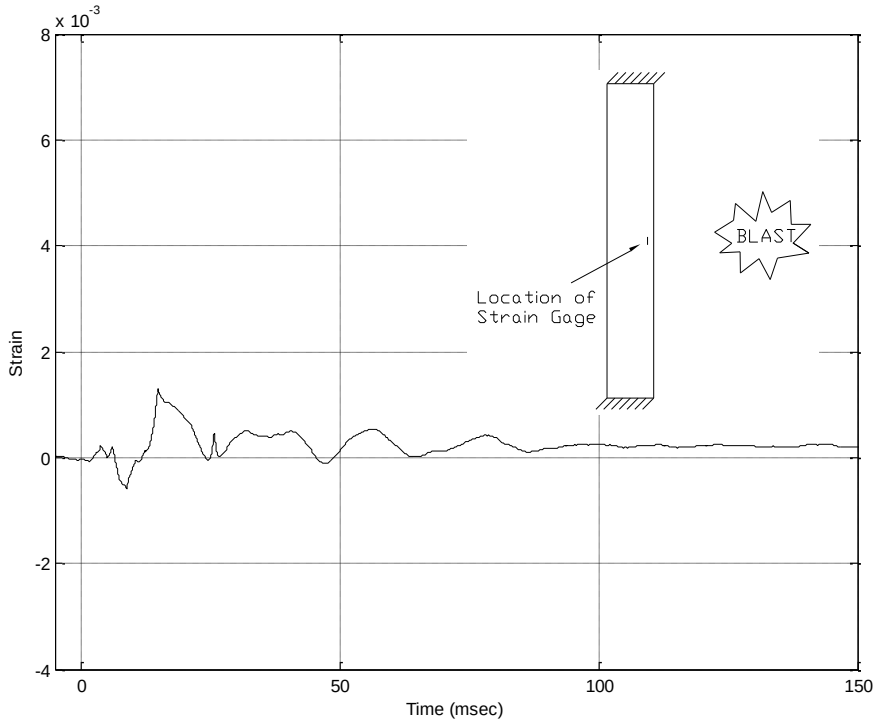

Figure 6.41. Column 3: Positive Moment (Compression) Strain

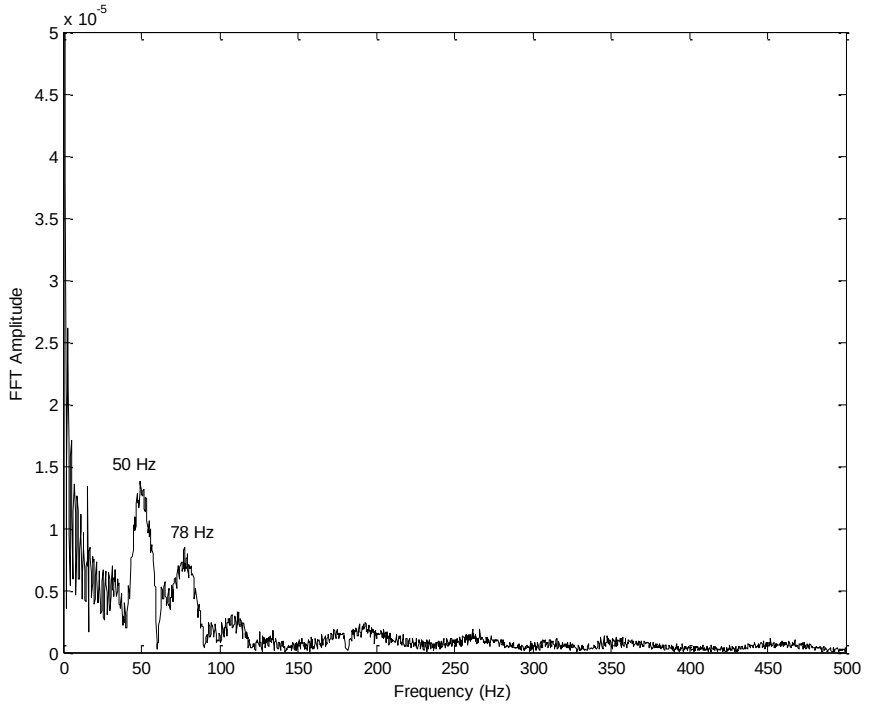

Figure 6.42. Column 3: Positive Moment (Compression) Strain FFT Plot

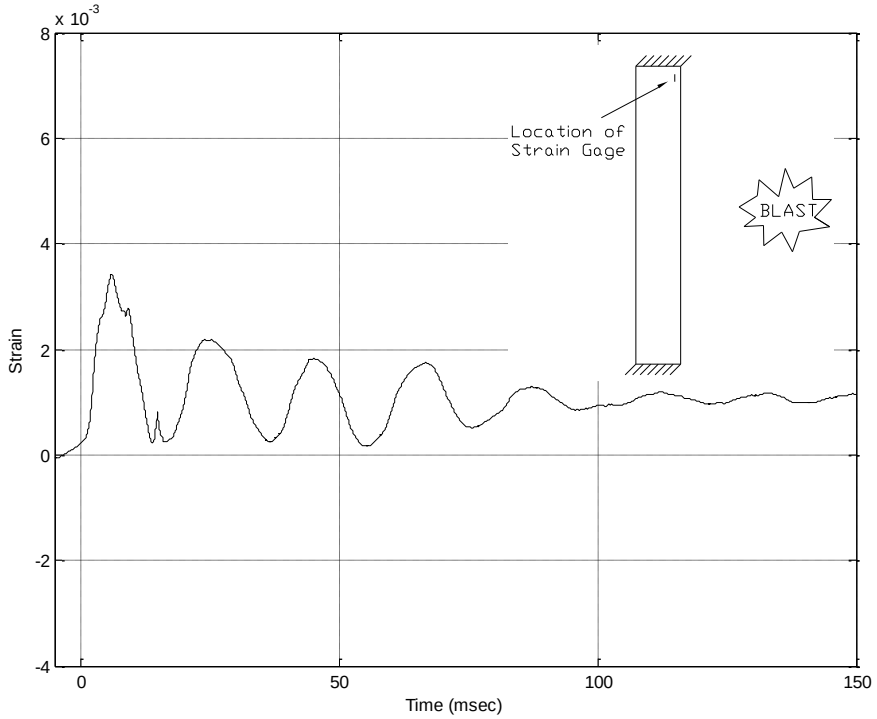

Figure 6.43. Column 3: Negative Moment (Tension) Strain

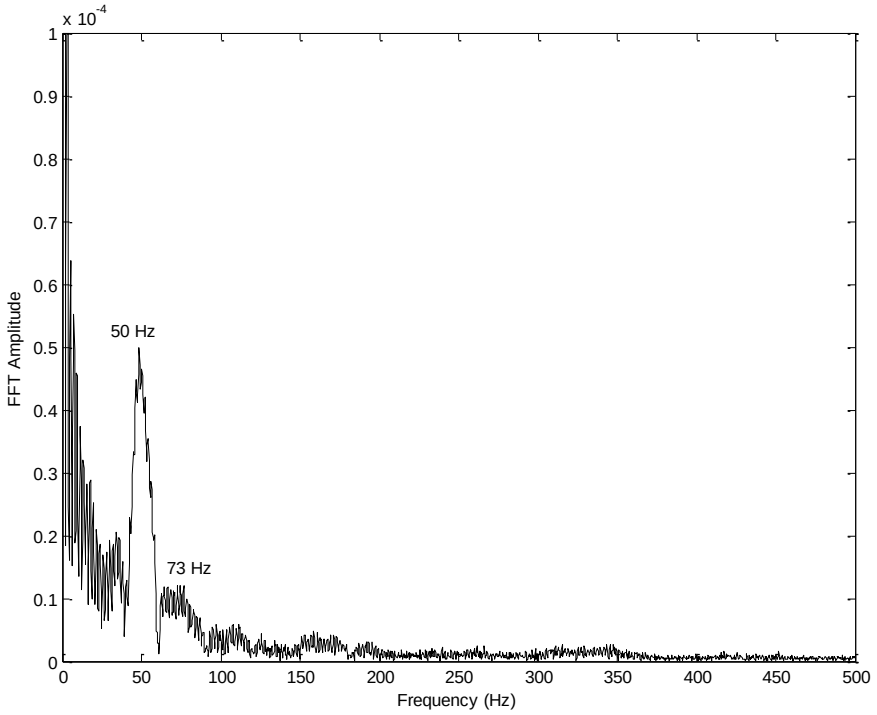

Figure 6.44. Column 3: Negative Moment (Tension) Strain FFT Plot

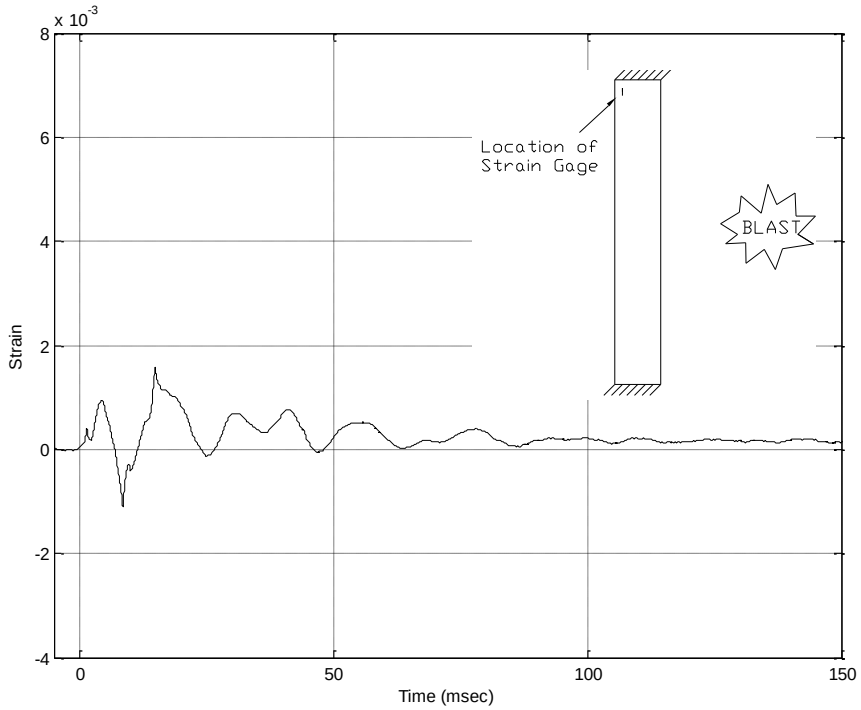

Figure 6.45. Column 3: Negative Moment (Compression) Strain

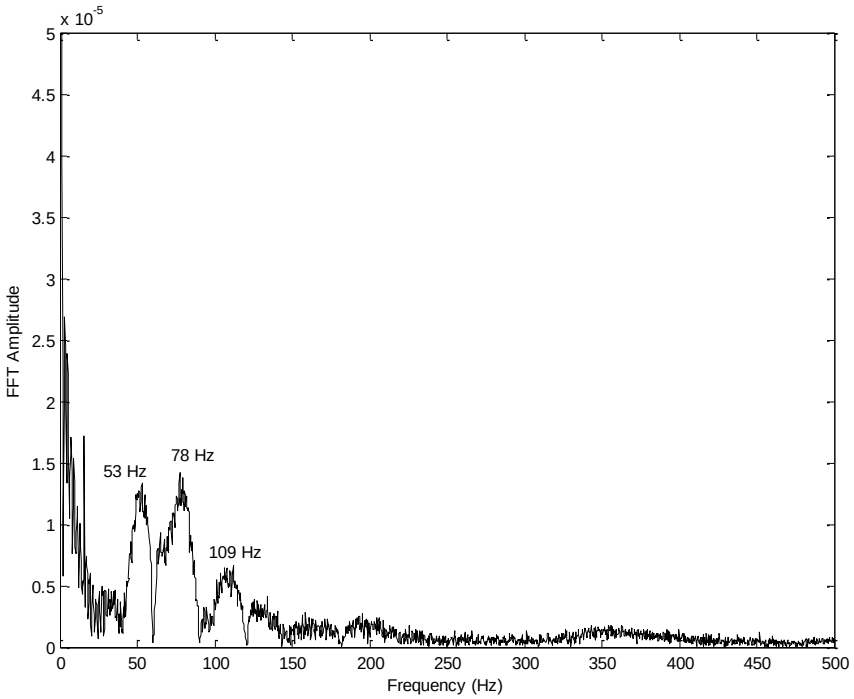

Figure 6.46. Column 3: Negative Moment (Compression) Strain FFT Plot

6.7. COAXIAL CABLE CRACK SENSOR MEASUREMENTS

The crack sensors were used to record dynamic data from Column 1 during the blasts and to record static data both before and after each blast. The sensors were embedded in the footing of the columns as well, but since the footing had minimal cracking from the blast, only the column portion of the sensor data is presented.

6.7.1. Dynamic Measurements. One of the main objectives of this research was to validate the performance of these sensors under a high strain-rate event, such as a blast. The sensors worked well during the dynamic testing. In fact, the crack sensors supplied more data than many of the other transducers used in the testing. It was shown that it is possible to record cracking during a loading event. One 'frame' of dynamic data was captured every 0.5 msec, which should be fast enough to capture the response of the column to the impulsive load since its natural period is approximately 18 msec, but maybe not fast enough to capture the initial crack propagation from the blast. For clarity, 'snapshots' of certain frames of data were taken from the dynamic data and plotted to show the progression of cracking during the blast. Figure 6.47 shows dynamic data from the second 4 lbs blast and Figure 6.48 shows data from the 10 lbs blast. Dynamic data was not recorded for either the first 4 lbs blast or the 30 lbs blast due to either malfunction of data acquisition or the charge size being too large to safely record data.

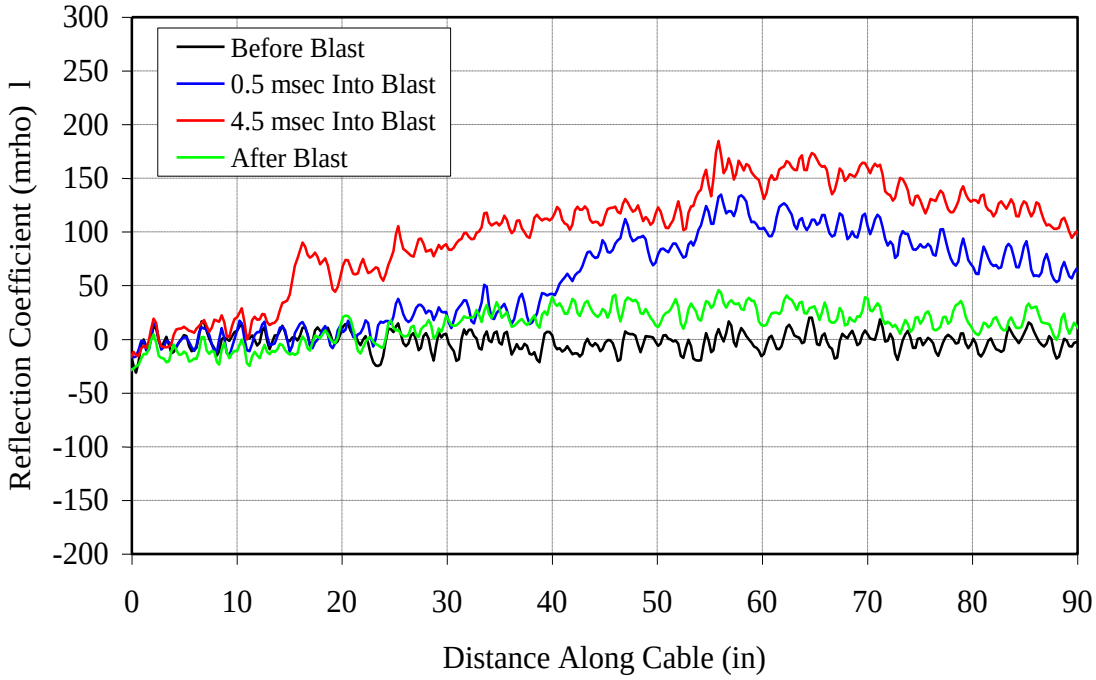

Figure 6.47. Dynamic Data from Column 1 during the 2nd 4 lbs Blast

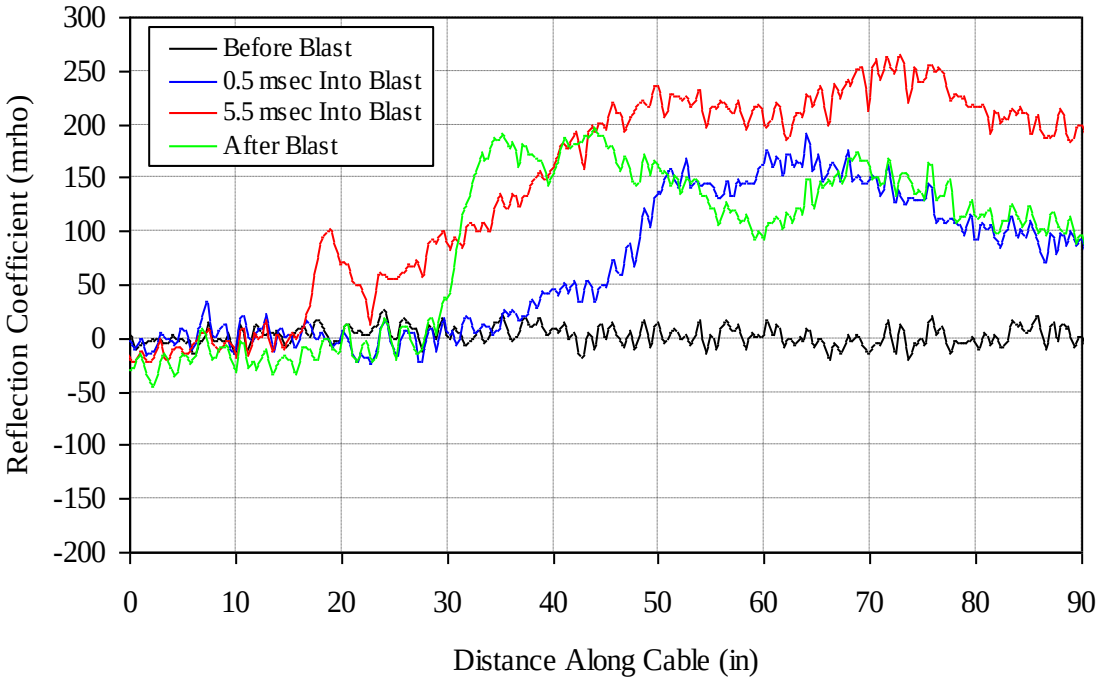

Figure 6.48. Dynamic Data from Column 1 during the 10 lbs Blast

The effect of the blast is seen in both figures. Figure 6.47 shows the curve increasing and then almost going back to its original position. The 4 lbs blasts did not create severe damage to Column 1, but they did cause significant cracking around the mid-height. The green line in Figure 6.47 shows how this cracking affected the final signal along the sensor, as the signal did not return to its original position. Referred to as the "memory" feature of the coaxial cable sensor, this can be seen in both figures, but is much more pronounced in Figure 6.48, as the 10 lbs blast caused significant spalling on the back of the column where the sensor was embedded. This left part of the sensor hanging out of the column.

6.7.2. Correlation of Dynamic Sensor Measurement and Strain. In an effort to relate strain to the crack sensor signal, a comparison was made relating the strain at the mid-height of the column to the crack sensor reflection coefficient at that location. Since the strain gage on the back side of the column (positive moment – tension) was at the same location as the crack sensor, this gage was used for comparison. The reflection coefficient at the mid-height of the column was extracted from each frame of dynamic data from the 4 lbs blast. Figure 6.49 shows this comparison. It is very clear that the shape of the strain response is similar to the shape of the crack sensor response. This is an anticipated yet interesting result since the width of cracks is directly related to the strain distribution across the member. It would be desirable to proceed with more testing in this area since one set of data is not sufficient to make a tangible conclusion or an empirical correlation.

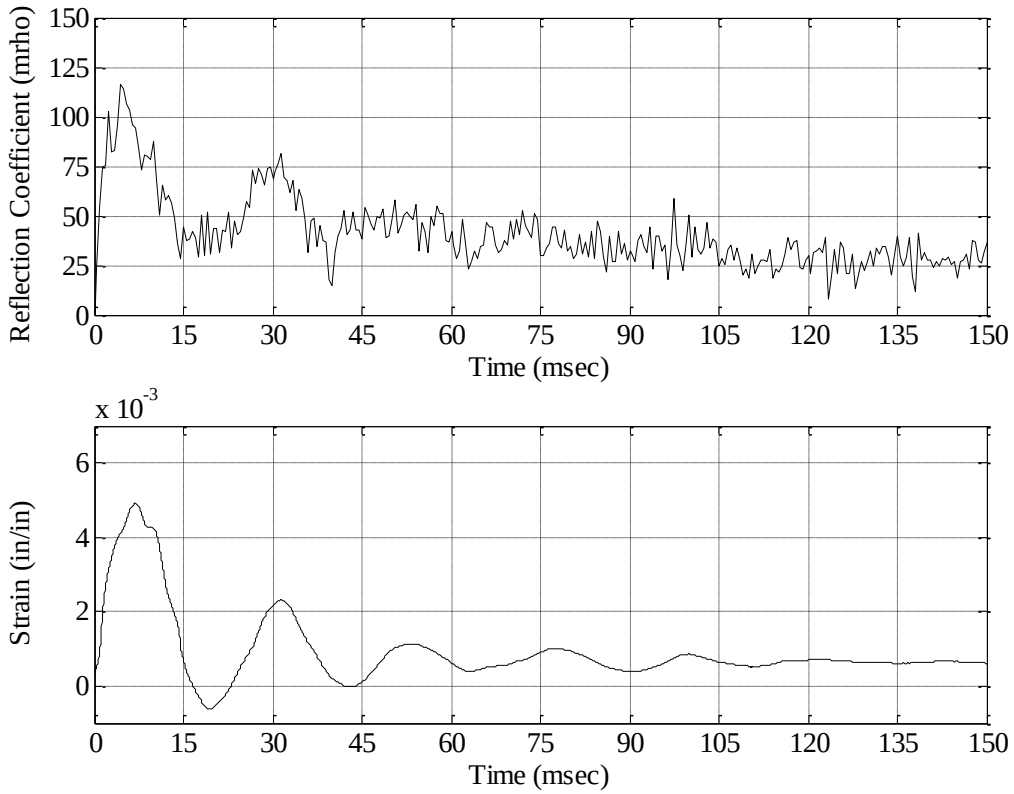

Figure 6.49. Relation of Tension Strain at Mid-height to Dynamic Crack Sensor Measurement at Mid-height

6.7.3. Static Crack Sensor Measurements. Static measurements were taken from the crack sensors embedded in all three columns at the following times: before and after the 2nd 4 lbs blast, before and after the 10 lbs blast, and after the 30 lbs blast. Due to equipment problems after the first blast, static measurements were not obtained from the first 4 lbs blast. To see only the effect of the blast, the signals recorded before each blast are differenced with (subtracted from) the signals recorded after each blast. The signals are also filtered using a lowpass filter to remove electrical noise. Comparisons of the three columns and their corresponding crack sensor signals are shown in Figure 6.50 through Figure 6.53.

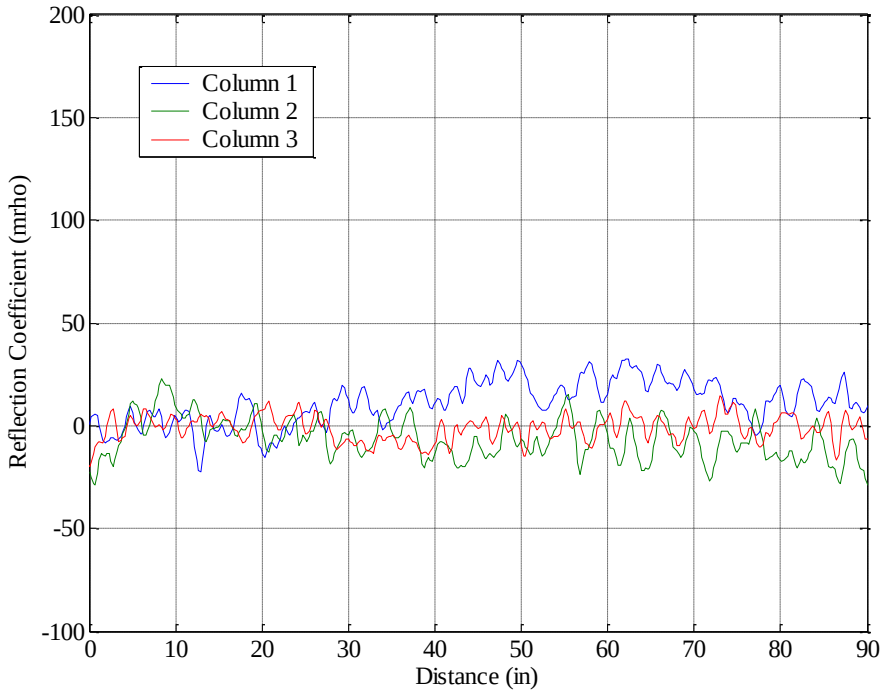

Figure 6.50. Crack Sensor Signals Taken after the 2nd 4 lb Blast (Differenced with the Signals Taken before the 2nd 4 lb Blast)

As can be seen in Figure 6.50, the blast did not cause severe cracking, and Column 1 was subjected to more cracking than Columns 2 and 3. As shown in Figure 6.51 and 6.52, the 10 lbs blast caused much more cracking in Column 1 than the 4 lbs blast, but Columns 2 and 3 still had low levels of cracking. The only difference in the two figures is that Figure 6.51 is differenced with the signals taken before the 4 lbs blast while Figure 6.52 is differenced with the signals taken before the 10 lbs blast. In other words, Figure 6.51 shows the cracking caused from both the 4 lb and 10 blasts while Figure 6.52 only shows the cracking caused from the 10 lb blast. This is why the blue curve in Figure 6.51 has a greater amplitude than the blue curve in Figure 6.52.

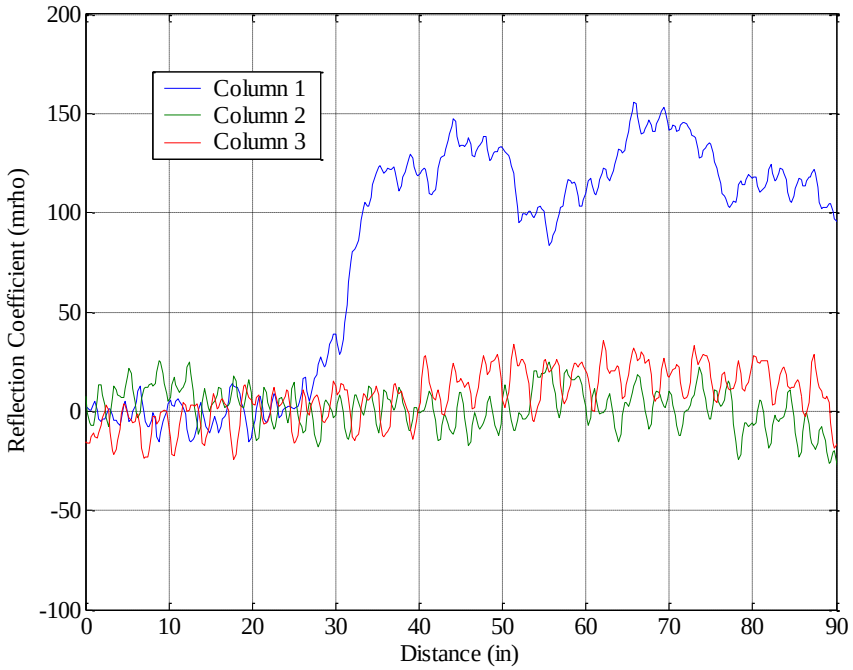

Figure 6.51. Crack Sensor Signals Taken after the 10 lbs Blast (Differenced with the Signals Taken before the 2nd 4 lb Blast)

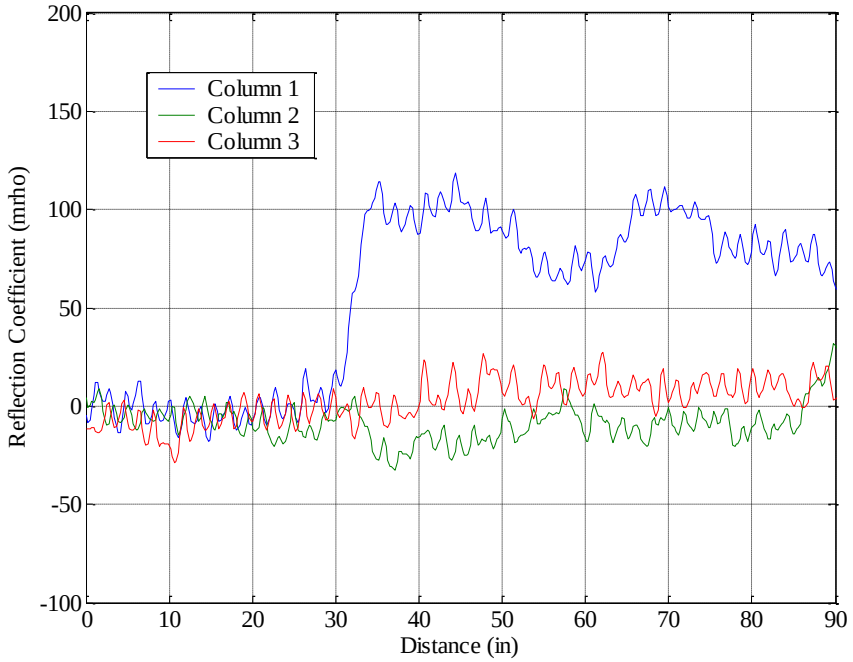

Figure 6.52. Crack Sensor Signals Taken after the 10 lbs Blast (Differenced with the Signals Taken before the 10 lb Blast)

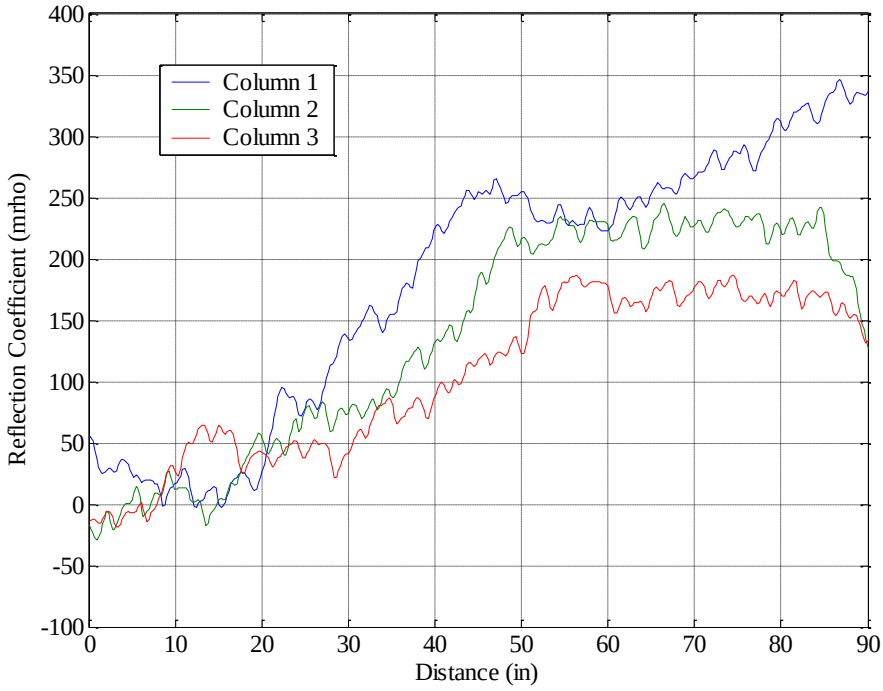

Figure 6.53. Crack Sensor Signals Taken after the 30 lb Blast (Differenced with the Signals Taken before the 2nd 4 lb Blast)

Figure 6.53 shows the severity of cracking that occurred from the 30 lbs blast, which failed all three columns. It does, however, show that there was a reduction in cracking from Column 1 to Columns 2 and 3. For each column, a sudden change in reflection coefficient can be observed around mid-height. This change is attributable to the formation of a plastic hinge at the mid-height of the column.

Column 1 was unstrengthened, allowing for visual inspection of cracking after each blast test. Figure 6.54 shows the reflection coefficient due to the 2nd 4 lb blast. The blue lines in the picture designate the cracks that occurred from the 1st 4 lb blast, and the red lines indicate the cracks that occurred from the 2nd 4 lb blast. It seems difficult to distinguish individual cracks in the signal. This could be due to the spatial resolution used to record the signal (distance between each data point). It can be seen, however,

that the curve starts to increase around the mid-height of the column, where many cracks are located. This trend is also seen in Figures 6.55 and 6.56.

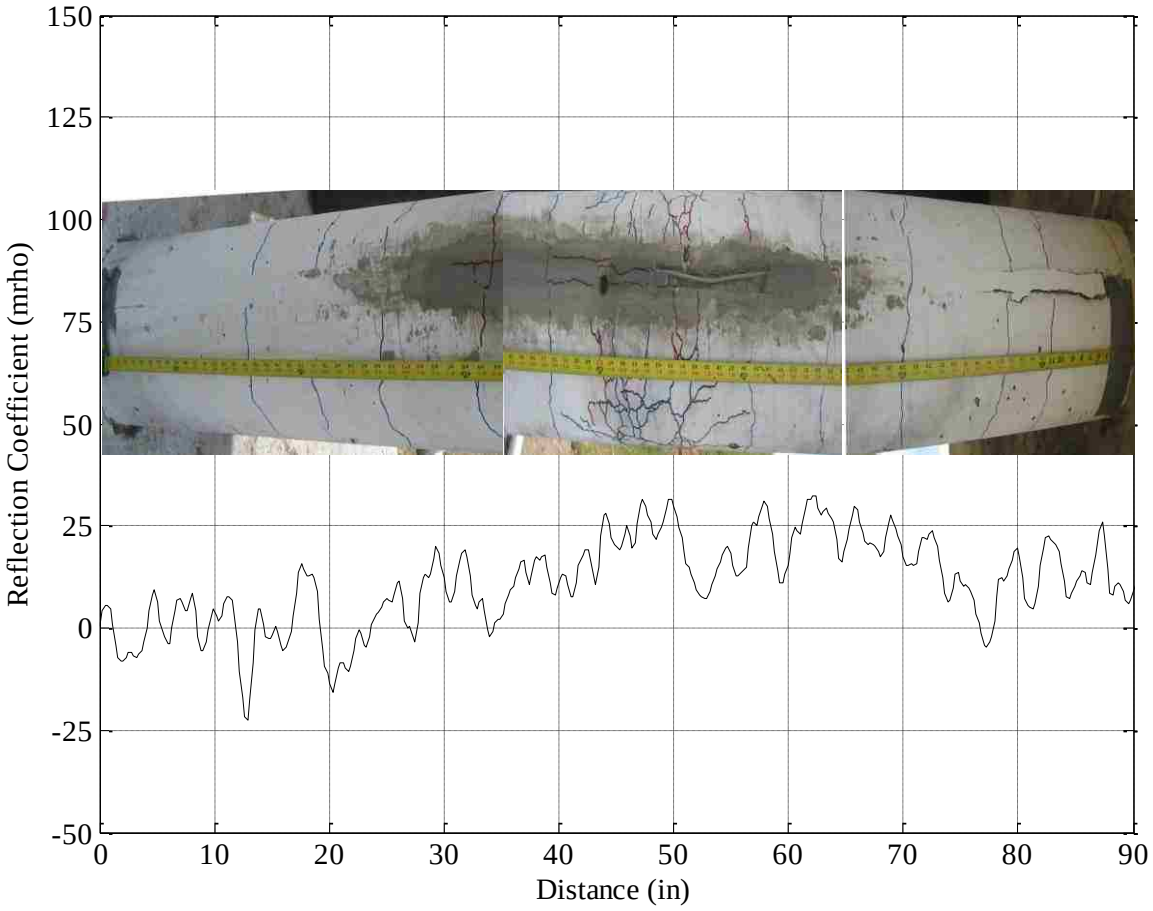

Figure 6.54. Column 1 2nd 4 lbs Crack Sensor Signal Compared to Picture of Cracking

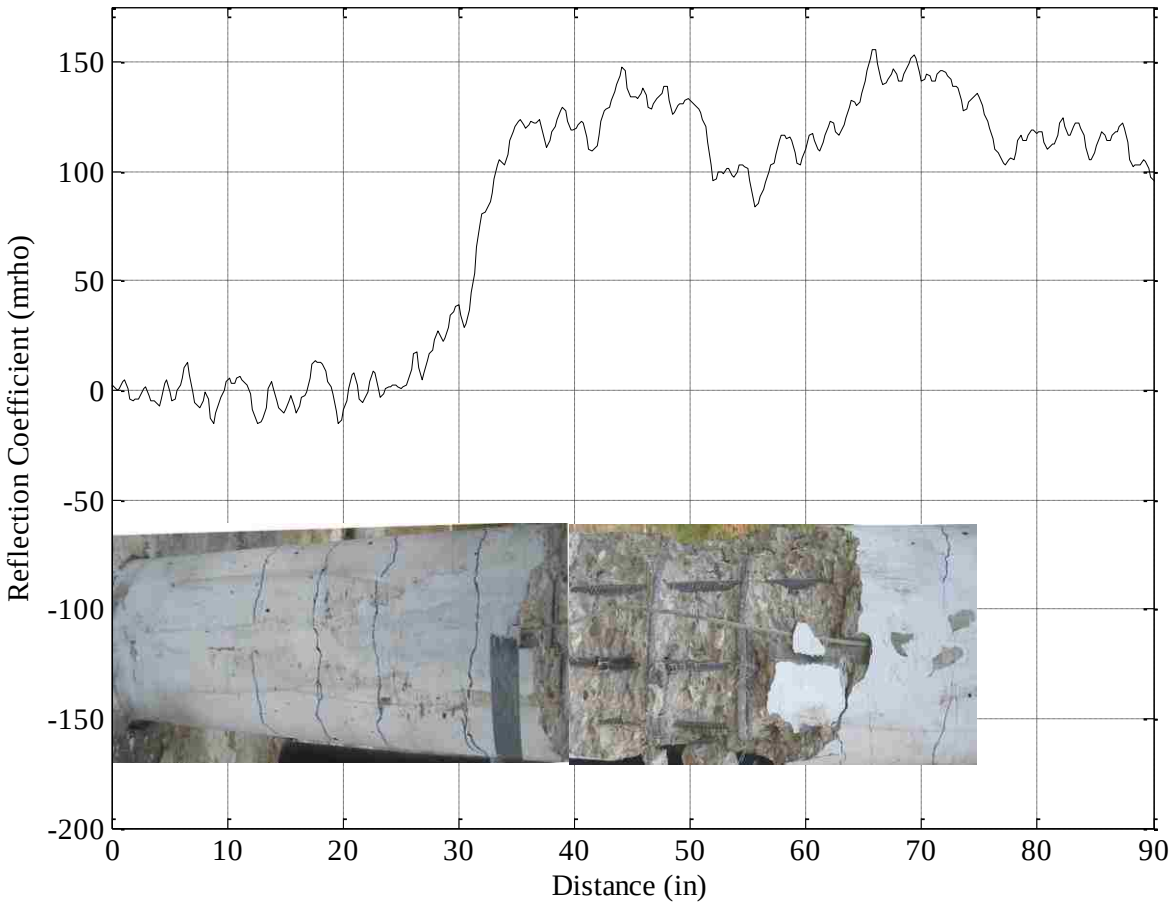

Figure 6.55. Column 1 10 lbs Crack Sensor Signal Compared to Picture of Cracking

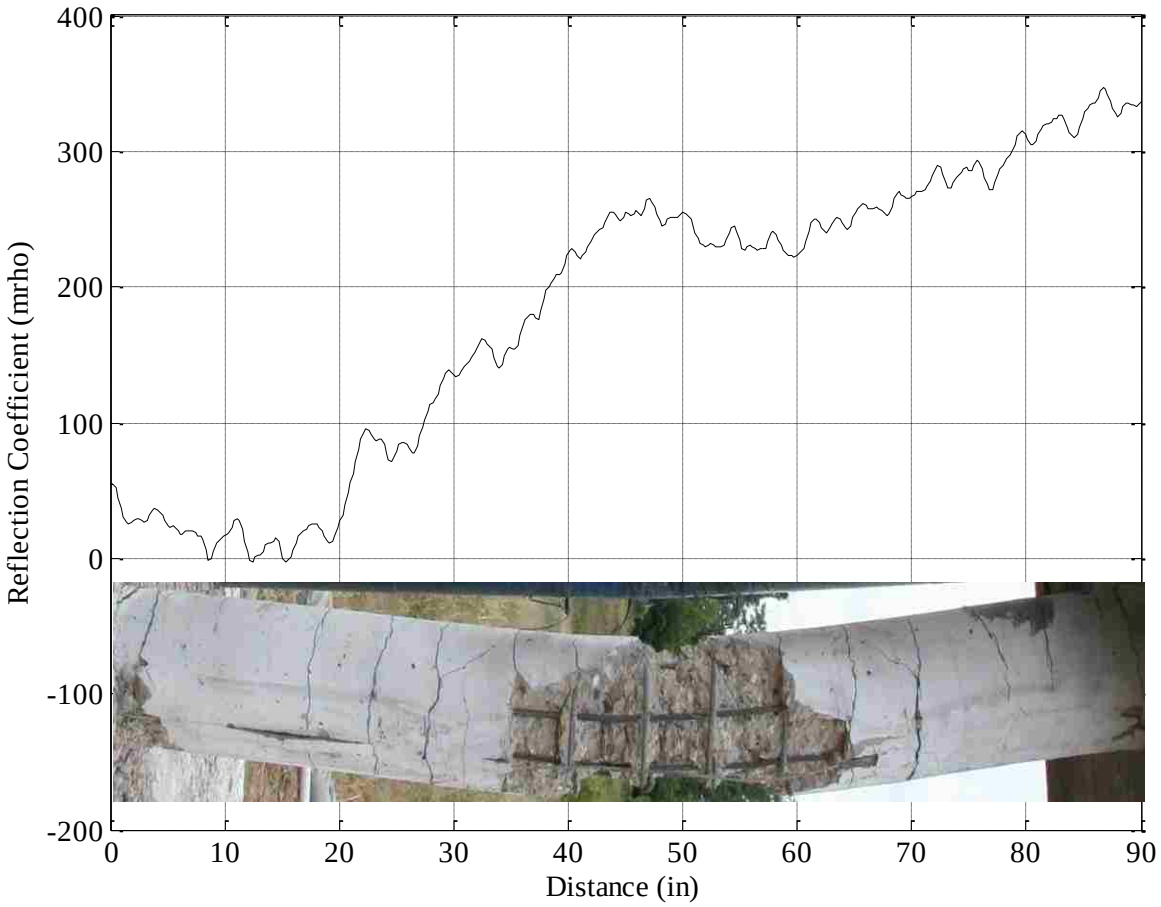

Figure 6.56. Column 1 30 lbs Crack Sensor Signal Compared to Picture of Cracking

7. CONCLUSIONS

7.1. GENERAL

In this study, a three-column specimen was tested in order to fulfill two objectives. The first objective was to validate the performance of an FRP-VE strengthening system for RC columns in mitigating blast loads. The second objective was to validate the performance of coaxial cable crack sensors when measured dynamically under blast loading.

The FRP-VE strengthening system performed very well during the testing. It was shown to reduce the permanent mid-height deformation of the column by 50% when compared to an unstrengthened column and an FRP-confined column. This reduction in permanent deformation is important because larger deflections in the column would result in much larger P-Δ moments if the column was supporting a significant axial load. These additional moments could cause instability or even collapse of the entire structure. It was also shown to nearly eliminate the occurrence of spalling and scabbing on the column. These high-velocity fragments are often what cause injuries and casualties to occupants of buildings during an explosion. It took 30 pounds of explosives at 0.46 m [1.5 ft] standoff distance (to face of column) to cause cratering on the front side of Column 2 (CFRP-confined column), but even at this charge size Column 3 (FRP-VE column) still had no signs of cratering or spalling. Finally, it was demonstrated that FRP is still able to confine the concrete under a close-in explosion, and the VE material attached outside the inner FRP for column confinement can protect the inner FRP material.

The coaxial cable crack sensors also behaved very well during the testing. It was shown that cracks can be detected dynamically under very rapid loading, such as blast effects. This technology could prove to be a very effective tool for structural health monitoring of critical infrastructure. When comparing the sensor signals both during and after the blast, the strengthening system showed a significant reduction in cracking when compared to the control column. There was also a correlation found between the reflection coefficient and strain at the same location in the column when measured dynamically. Currently, a more robust data acquisition system is being developed for dynamic testing of the crack sensors. When this system is completed, better data acquisition will be available for use in future testing.

7.2. RECOMMENDATIONS

This study was primarily a proof-of-concept test. Additional testing needs to be done in order to further characterize the FRP-VE strengthening system for blast loading, as well as the coaxial cable crack sensors when used to detect cracks at very high loading rates. Items that should be addressed include the following:

- An analytical model should be developed for both rectangular and circular columns for transient, short-duration (blast or impact) loading.
- A parametric study should be conducted examining the FRP and VE properties that result in optimal effectiveness of the retrofitting system under blast loads.
- A more complex finite element model needs to be developed that utilizes an FE code specifically designed for blast loading such as LS-DYNA or DYNA3D.

These programs can more accurately simulate the blast pressures created by the shock front and the dynamics of the fluid in which the explosive is detonated.

- Additional blast tests should be conducted on larger scale specimens and/or specimens with additional axial load added to better simulate the behavior of actual columns.
- The instrumentation protection should be planned out better so that less data is lost in the testing.
- Other types of FRP, such as Aramid and Glass, should be investigated for use in the strengthening system. Aramid is often used in strengthening for blast loads because of its impact resistance.
- Once the system has undergone supplementary testing, design equations should be developed that allow engineers to apply the system as an actual strengthening regime.
- More work should be done in order to correlate the dynamic measurements from the crack sensors and strain gages.
- Additional dynamic testing of the crack sensors using the new data acquisition system is required to better understand their behavior under dynamic loading.

BIBLIOGRAPHY

ABAQUS Finite Element Software. (2005). "User's Manual," Version 6.5.

ABAQUS Finite Element Software. (2005). "Theory Manual," Version 6.5.

Al-Salloum, Y.A. (2007). "Effect of High Temperatures on FRP-Confined Concrete." In: *Proceedings of the First International Workshop on Performance, Protection, and Strengthening of Structures under Extreme Loading*. Whistler, Canada: The University of British Columbia.

American Concrete Institute Committee 440 (2002). "Guide for the Design and Construction of Externally Bonded FRP Systems for Strengthening Concrete Structures (440.2R-02)," Farmington Hills, Michigan: American Concrete Institute.

American Concrete Institute Committee 318 (2002). "Building Code Requirements for Structural Concrete (ACI 318-02 and Commentary (ACI 318R-02)," Farmington Hills, Michigan: American Concrete Institute.

Baker, W.E. (1973). *Explosions in Air*, Austin: University of Texas Press.

Bank, L.C. (2006). *Composites for Construction: Structural Design with FRP Materials*, Hoboken, New Jersey: John Wiley & Sons.

Beshara, F.B.A. (1994). "Modeling of Blast Loading on Aboveground Structures-I. General Phenomenology and External Blast," *Computers & Structures*, Vol. 51, No. 5, 585-596.

Buchan, P.A. and Chen, J.F. (2007). "Blast Resistance of FRP Composites and Polymer Strengthened Concrete and Masonry Structures – A State-of-the-art Review," *Composites Part B: Engineering, Infrastructure Composites under Extreme Loadings*, Vol. 38, No. 5-6, 509-522.

CEB-FIP MODEL CODE. (1990). "Design Code, Comite Euro-International Du Béton," Thomas Telford.

Chen, G.D., Mu, H.M., Pommerenke, D., and Drewniak, J.L. (2004). "Damage detection of reinforced concrete beams with novel distributed crack/strain sensors," *Journal of Structural Health Monitoring*, Vol. 3, No. 3, 225-243.

Chen, G.D., McDaniel, R.D., Sun, S.S., Pommerenke, D., and Drewniak, J.L. (2005). "Distributed Crack Sensors Featuring Unique Memory Capability for Post-Earthquake Condition Assessment of RC Structures," *Journal of Smart Structures and Systems*, Vol.1, No.2, 141-158.

Chopra, A.K. (2007), *Dynamics of Structures: Theory and Applications to Earthquake Engineering, Third Edition*, Upper Saddle River, New Jersey: Pearson Prentice Hall.

Crawford, J.E., Malvar, L.J., Wesevich, J.W., Valancius, J., and Reynolds, A.D. (1997). "Retrofit of Reinforced Concrete Structures to Resist Blast Effects." *ACI Structural Journal*, Vol. 94, No. 4, 371–377.

Crawford, J.E., Malvar, L.J., and Morrill, K.B. (2001a). "Reinforced Concrete Column Retrofit Methods for Seismic and Blast Protection." In: *Proceedings of the Society of American Military Engineering Symposium on Compressive Force Protection*. Charleston, USA: Society of American Military Engineers.

Crawford, J.E., Malvar, L.J., Morrill, K.B., and Ferritto J.M. (2001b). "Composite Retrofits to Increase the Blast Resistance of Reinforced Concrete Buildings." In: *Proceedings of the 10th International Symposium on Interaction of the Effects of Munitions with Structures*. San Diego, USA. 1–13.

Esmaeily, A. (2001). "USC_RC Computer Software Help Documents," Los Angeles, CA: Asad Esmaeily.

Federal Emergency Management Agency (FEMA). (1998). "Handbook for the Seismic Evaluation of Buildings—A Prestandard." *FEMA 310*. Washington, D.C.

Gram, M.M., Clark, A.J., Hegemier, G.A., and Seible, F. (2006). "Laboratory Simulation of Blast Loading on Building and Bridge Structures." *The Built Environment – Structures Under Shock and Impact IX*, Vol. 87, 33-44.

Hayes, J.R., Woodson, S.C., Pekelnicky, R.G., Poland, C.D., Corley, W.G., and Sozen, M. (2005). "Can Strengthening for Earthquake Improve Blast and Progressive Collapse Resistance?" *Journal of Structural Engineering*, Vol. 131, No. 8, 1157-1177.

HNDM-1110-1-2 (1977). "Suppressive Shields–Structural Design and Analysis Handbook." U.S. Army Corps of Engineers: Huntsville, AL.

Hopler, R. (Ed.). (1998). *Blasters' Handbook, 17th Edition*. International Society of Explosives Engineers: Cleveland, OH, 626-644.

Huang, X. (2005). "An Integrated VE Damping and FRP Strengthening System for Performance-based Seismic Retrofit of RC Columns." Doctoral Dissertation, University of Missouri – Rolla.

Joint Departments of the Army, The Navy, and The Air Force. (1990). "Structures to Resist the Effects of Accidental Explosions (TM 5-1300)." Technical Manual. Washington, DC.

Jones, D., Johnson, G, and Lockwood, J. (1995). "Protecting Building Occupants from Explosions and Fires in Processing Facilities." EQE Review.

Kiger, S. and Woodson, S. (2008). "Explosion Effects and Structural Design for Blast: A Two-Day Training Course." Course Notes. St. Louis, MO.

Kinney, G.F. and Graham, K.J. (1985). *Explosive Shocks in Air*. Springer-Verlag New York.

Lee, J. and Fenves, G.L. (1998). "Plastic-damage Model for Cyclic Loading of Concrete Structures." *Journal of Engineering Mechanics*, Vol. 124, No. 8, 892-900.

Lubliner, J., Oliver, J., and Onate, E. (1989). "A Plastic-damage Model for Concrete." *International Journal of Solids and Structures*, Vol. 25, 299-329.

Luo, X., Aref, A.J., and Dargush, G.F. (2007). "Analysis and Optimal Design of Layered Elastic Stress Wave Attenuators Subjected to Impulse Loading." In: *ECCOMAS Thematic Conference on Computational Methods in Structural Dynamics and Earthquake Engineering.* Rethymno, Crete, Greece.

MacGregor, J.G. and Wight, J.K. (2005). *Reinforced Concrete: Mechanics and Design, Fourth Edition*. Upper Saddle River, New Jersey: Pearson Prentice Hall.

Malhotra, A., Carson, D., and Stevens, T. (2007). "Demystifying Blast Effects on Buildings." In: *Proceedings of the First International Workshop on Performance, Protection, and Strengthening of Structures under Extreme Loading*. Whistler, Canada: The University of British Columbia.

Malvar, L.J. and Ross, C.A. (1998). "Review of Strain Rate Effects for Concrete in Tension." *ACI Materials Journal*, November-December, 735-739.

Malvar, L.J., Morrill, K.B., and Crawford, J.E. (2004). "Numerical Modeling of Concrete Confined by Fiber Reinforced Composites." *Journal of Composites for Construction*, Vol. 8, No. 4, 315–322.

Mays, G.C. and Smith P.D. (1995), *Blast Effects on Buildings*. London: Thomas Telford Publications.

McDaniel, R.D. (2004). "Characterization and Implementation of Distributed Coaxial Cable Crack Sensors for Embedment in Reinforced Concrete Structural Members." Master's Thesis, University of Missouri – Rolla.

Mendis, P., Pendyala, R., and Setunge, S. (2000). "Stress-strain Model to Predict the Full-range Moment Curvature Behavior of High-strength Concrete Sections." *Magazine of Concrete Research*, Vol. 52, No. 4, 227-234.

Morrill, K.B., Malvar, L.J., Crawford, J.E., and Ferritto, J.M. (2004). "Blast Resistant Design and Retrofit of Reinforced Concrete Columns and Walls." In: *Proceedings of the 2004 Structures Congress – Building on the Past: Securing the Future*. Nashville, TN.

Muszynski, L.C., Purcell, M.R., and Sierakowski, R. (1995). "Strengthening Concrete Ctructures by Using Externally Applied Composite Reinforcing Material." In: *Proceedings of the Seventh International Symposium on Interaction of the Effects of Munitions with Structures*. Germany, 291–298.

Muszynski, L.C., Purcell, M.R. (2003). "Composite Reinforcement to Strengthen Existing Concrete Structures Against Air Blast." *Journal of Composites for Construction*, Vol. 7, No. 2, 93–97.

Sorbothane, Inc. (2001). "Sorbothane: Material Properties." Kent, OH.

Watson, Bowman, Acme Corporation. (2002). "Wabo MBrace Saturant Epoxy Encapsulation Resin Data Sheet." Amherst, New York.

Watson, Bowman, Acme Corporation. (2003). "Wabo MBrace CF 160 Unidirectional High Strength Carbon Fiber Fabric Data Sheet." Amherst, New York.

Woodson, S.C. and Baylot, J.T. (2000). "Quarter-Scale Building/Column Experiments." In: *Proceedings of the 2000 Structures Congress – Advanced Technology in Structural Engineering*. Philadelphia, PA.

Xue, L. (2006). "Power Distribution Network Modeling for Design and High-speed Time-domain Reflectometer System Design for Cable Sensor Defect Measurement." Master's Thesis, University of Missouri – Rolla.

VITA

Brian Henry Wood was born on October 28, 1983 at Jackson Madison County General Hospital in Jackson, Tennessee. He attended North Side High School in Jackson, Tennessee, where he graduated with Highest Honors in 2002. He began his undergraduate studies at the University of Tennessee at Martin in August of 2002. While at UTM, Brian served as Treasurer of the ASCE Civil Engineering Student Chapter, participated in steel bridge competitions, and played intramural soccer. He was also a member of Sigma Alpha Epsilon Fraternity, Tennessee Tau Chapter, where he served as Vice President, Treasurer, and Secretary. In December of 2006, he received certification as an Engineer Intern in the State of Tennessee. He graduated with a Bachelor of Science in Engineering Degree, Summa Cum Laude, in May of 2006. He married Jennifer Lyn Heer on July 29, 2006. Brian began his graduate career at the then University of Missouri – Rolla in August of 2006 under the direction of Dr. Genda Chen. He served as a Graduate Research and Teaching Assistant under Dr. Chen. Brian graduated with a Master of Science in Civil Engineering in August of 2008 from the now Missouri University of Science and Technology and began working as a Structural Engineer in Nashville, TN.